Techniques for Battery Health Conscious Power Management via Electrochemical Modeling and Optimal Control

by

Scott J. Moura

A dissertation submitted in partial fulfillment
of the requirements for the degree of
Doctor of Philosophy
(Mechanical Engineering)
in The University of Michigan
2011

Doctoral Committee:

      Assistant Professor Hosam K. Fathy, Co-Chair, Pennsylvania State University
      Professor Jeffrey L. Stein, Co-Chair
      Professor Jessy Grizzle
      Professor Huei Peng

Far better is it to dare mighty things, to win glorious
triumphs, even though checkered by failure, than to rank
with those poor spirits who neither enjoy nor suffer much,
because they live in a gray twilight that knows not victory
nor defeat.

— Theodore Roosevelt

If we knew what we were doing, it wouldn't be called
research

— Albert Einstein

This thesis is dedicated to my parents, Manny and Bonnie Moura,
to my aunt and uncle, Leslee and Michael Perlstein,
and finally my puppy, Jek.

Acknowledgments

First and foremost, I wish to extend gratitude towards my advisors, Prof. Hosam Fathy and Prof. Jeff Stein. Their astute mentorship, thoughtful guidance, and unwavering support is deeply appreciated. Hosam jokes that upon entering graduate school I was "as green as green can be." Since then, Hosam's profound counseling has been instrumental toward my development as a scientific scholar. In particular, his ability to distill the important facts, find technical weaknesses, and recommend creative solutions are simply uncanny. In am indebted to Prof. Stein for teaching me to approach research with maturity. Prof. Stein has a unique ability to "see the big picture," connect concepts, and contextualize results. These skills directly impacted my own maturation. More than anything else, Hosam and Prof. Stein always believed in me.

I am extremely thankful to my committee members, Prof. Huei Peng and Prof. Jessy Grizzle, for asking tough questions and providing critical feedback. Their insightful advice has been crucial toward creating a solid foundation for the work presented in this dissertation.

Several colleagues deserve special recognition for their mentorship and friendship during my doctoral studies. I thank Jason Siegel for his endless knowledge on fabricating experimental facilities. I thank Dan Opila for tips on stochastic dynamic programming, the Center for Advanced Computing, and being an inspirational role-model who occasionally invites me on breath-taking flying trips across Southeast Michigan. I thank Dongsuk Kum for his support, technical discussions, and introduction to authentic Korean food. I thank Giulio Ripaccioli for his great friendship and hospitality. He came to The States to learn from us, but I learned more from him than he could possibly imagine. I thank Carmelo Speltino for his friendship, witty humor, and tiramisu cooking lessons. I thank Stefano DiCairano for his friendship and career advice. Stefano is my role-model for academic/industrial success. These colleagues are my idols, and this work would not be possible without them.

I wish to acknowledge Laura Perkett and Caitlin McKeighan for their instruction

iii

Table of Contents

List of Tables

List of Figures

List of Appendices

Abstract

This dissertation combines electrochemistry-based battery models and optimal control theory to study power management in energy storage/conversion systems. This topic is motivated by the need to enhance the performance and longevity of battery electric systems. In particular, the rapid progress in battery material science and energy conversion presents a highly relevant opportunity to bridge the knowledge gap between electrochemistry and control. Ultimately, this dissertation elucidates the key physical phenomena in battery-powered systems which enable opportunities to improve battery performance and health through control. We address this topic in three phases.

First we provide an overview of battery fundamentals and relevant degradation mechanisms. Then we develop mathematical models for the electrochemical battery phenomena, plug-in hybrid vehicle drivetrain dynamics, and stochastic drive cycle dynamics. A battery-in-the-loop experimental test system is fabricated to identify the electrochemical battery model.

Second, we investigate the battery-health conscious power management problem for plug-in hybrid electric vehicles (PHEVs). This effort designs controllers to split engine and battery power to minimize both fuel/electricity consumption costs and battery state-of-health degradation. Mathematically, this problem is formulated as a stochastic dynamic program. The degradation phenomena considered include anode-side solid electrolyte interphase film growth and the "Ah-processed" model. This work is the first to utilize fundamental electrochemical battery models to optimize power management.

The final phase proposes a novel battery pack management strategy which investigates the potential health advantages of allowing unequal yet controlled charge levels across batteries connected in parallel. Mathematically, this problem is formulated as a deterministic dynamic program. The optimal solutions reveal that capacity fade can be mitigated through controlled charge unequalization if concavity properties exist in the health degradation dynamics. The sensitivity of these results are analyzed across various degradation models derived from existing literature and experimental data.

In total, this dissertation utilizes physics-based battery models to optimize power management in energy storage systems. The unique overarching contribution is a systematic optimal control approach for elucidating the physical electrochemical properties one can exploit through control to enhance battery performance and life. The second and third phases described above demonstrate how this approach can be very useful for PHEV and battery pack management applications

Chapter 1
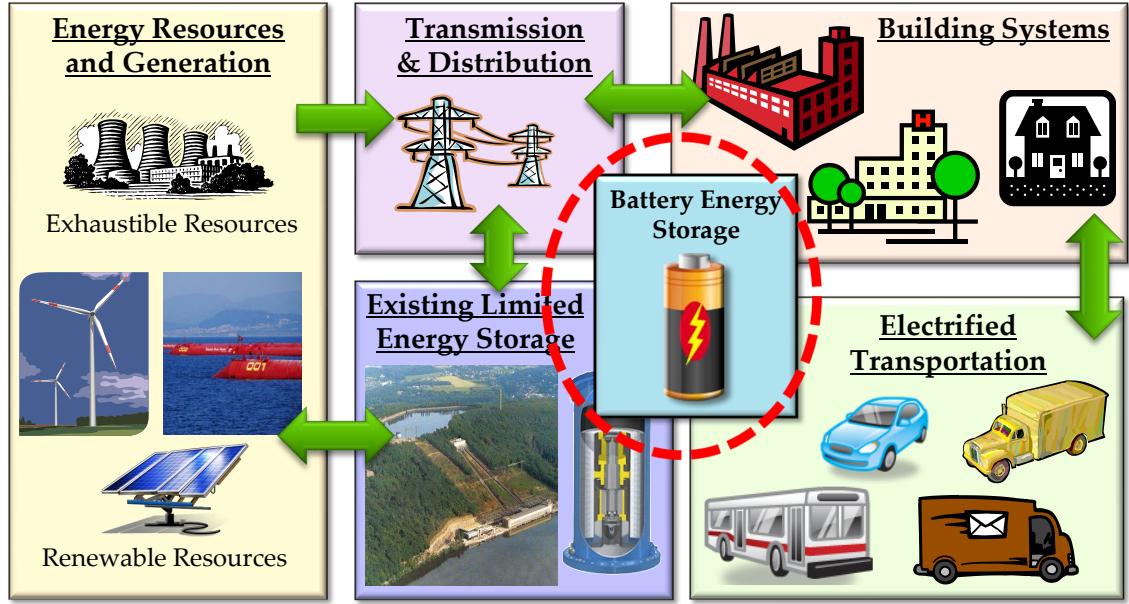
Introduction

This dissertation combines electrochemical physics and optimal supervisory control to study the tradeoffs between performance and health in battery-powered systems. The proposed health-conscious control algorithms have the potential to increase the performance characteristics and long-term energy capacity of battery packs. This is critically important for large scale battery energy storage systems - ranging from electrified transportation to stationary grid-scale storage - where replacement cost, bulk, and cycle life are inhibiting factors associated with the uncertainty in maintaining safe operation. Moreover, the framework presented here fuses electrochemical physics and control techniques to increase our intellectual understanding of how to manage their interaction.

In order to design battery-health conscious power management algorithms via electrochemical principles, this dissertation introduces novel techniques for modeling, control problem formulation, and analysis. These techniques may be applied to any situation which involves complex physical models, multiple energy storage/conversion devices, stochastic dynamics, multiple objectives, and state/control constraints. This dissertation applies these techniques to plug-in hybrid electric vehicles (PHEVs) and lithium-ion battery packs. Nonetheless, the approaches are fundamental and extend beyond batteries and PHEVs.

Ultimately, the results of this dissertation highlight which physical/mathematical properties in battery health degradation dynamics enable the use of innovative control techniques to enhance performance and health attributes. These specific properties include slope and convexity of health degradation metrics with respect to state-of-charge and current. This question has been generally unexplored in the literature. Yet it results from the innovative combination of electrochemical physics and supervisory control explored here.

The remainder of this introduction is structured as follows. First, we motivate the above research question through its broader impacts on the energy and transportation

Figure 1.1 Potential future energy infrastructure, in which battery energy storage mitigates the intermittency of renewable energy generation. Photos sources: Tidal power photo from Pelamis Agucadoura wave farm project in Portugal, pumped hydroelectric storage photo from [2], flywheel diagram courtesy of Beacon Power Corporation.

infrastructure. Second, we succinctly summarize the technical challenges associated with optimal power management of battery-powered systems via electrochemical modeling. Third, we review the existing literature which sets the foundation for this work. Finally, we summarize the contributions of this dissertation and outline their development in the subsequent chapters.

1.1 Research Objective and Motivation

The objective of this dissertation is to develop battery health conscious algorithms which manage power flow in energy systems. The relevancy of this topic is highlighted by the 27.2 billion USD federal government investment in energy efficiency and renewable energy research, including advanced batteries and electrified transportation, under the American Recovery and Reinvestment Act (ARRA) of 2009 [11]. Techniques for battery-health conscious power management are further motivated by a vision for the future energy infrastructure, depicted in Fig. 1.1. Potentially, renewable energy will represent a significant portion of the energy generation mix. In the near term, ARRA

Table 1.1 Renewable Portfolio Standards for Select States [1]

State	Renewable Energy as Percentage of Total Sales	Year Full Requirements Take Effect
California	33%	2030
Colorado	20%	2020
Hawaii	20%	2020
Illinois	25%	2025
Massachusetts	15%	2020
Maryland	20%	2022
Maine	40%	2017
Michigan	10%	2015
New Jersey	22.5%	2021
Nevada	20%	2015
New York	24%	2013
Oregon	25%	2025
Pennsylvania	8%	2020
Utah	20%	2025
Virginia	12%	2022
Washington	15%	2020
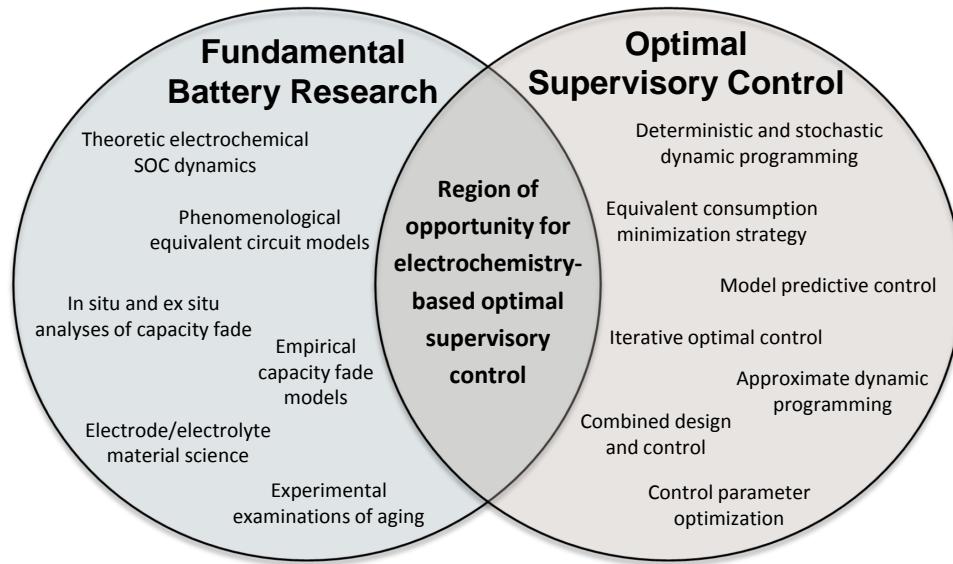
seeks to double nation-wide renewable energy capacity within two years [11]. In the long term, individual states are implementing renewable portfolio standards (RPS) to increase renewable energy production. The current RPS programs for several select states are included in Table 1.1 [1]. Yet most renewables such as wind, solar, and tidal power are fundamentally intermittent sources which do not temporally match energy demand. Overcoming this mismatch to enable significant penetration of renewable energy requires large scale energy storage. This is where electrified transportation can provide an enabling role. That is, large energy capacity battery packs on grid-connected vehicles can potentially provide the necessary energy storage to enable significant penetration of renewable energy. This "vehicle-to-grid" infrastructure thus couples the electric grid and transportation to form a large scale distributed energy generation, storage, and consumption system [12, 13, 14].

The critical enabling technology to realize this future energy infrastructure is, arguably, the battery energy storage system. In this dissertation we focus on modeling, systems, and control to study optimal power management algorithms for these battery systems. To narrow the focus further we study battery health-conscious optimal power

management in plug-in hybrid electric vehicle systems. Such health-conscious battery pack management has the potential to increase the useful life and reduce the long-term replacement costs of expensive high-capacity battery packs. This is important for ensuring the financial feasibility of battery energy storage in systems such as electric vehicles and smart grids, especially if such systems are able to share energy through, e.g., vehicle-to-grid (V2G) integration [15].

1.2 Literature Review

Two general categories of research provide the foundation for optimal power management of battery-powered systems. These include fundamental battery research and optimal supervisory control (see Fig. 1.2). One of this dissertation's main goals is to connect these two previously separate bodies of literature.

Figure 1.2 This dissertation seeks to contribute knowledge at the intersection of fundamental battery research and optimal supervisory control.

1.2.1 Fundamental Battery Research

The first body of literature involves fundamental battery research. This research considers the theoretical and experimental design and analysis of batteries through mechanical, material, and chemical science techniques. Much of the fundamental

operating principles are unified in excellent textbooks on electrochemical systems [16] and advanced batteries [17, 18].

In the area of Li-ion batteries, one of the first significant breakthroughs was the utilization of $LiCoO_2$ as the metal oxide cathode material. This battery design was eventually commercialized by Sony in 1991 [19]. More recently, $LiFePO_4$ cathodes with olivine structures were introduced as low-cost, safe alternatives to lithium cobalt oxide, though they sacrifice some energy density [20]. During the development of Li-ion batteries, lithium polymer battery technology was born. The key difference in lithium polymer batteries is that the electrolyte is contained within a solid polymer as opposed to an aqueous organic solvent [21]. The key advantages of such a design include lower manufacturing cost and flexible packaging. An excellent overview (ca. 1991) of lithium battery technology, its promises, and challenges is provided by Tarascon and Armand [22].

A crucial development in lithium battery technology was the discovery of intercalation compounds [22]. Intercalation, by definition, is the inclusion of one molecule between two other molecules. In the case of lithium batteries, the electrodes are made of intercalation compounds which effectively store and release lithium. Intercalation continues to be an extremely active area of research. Interested readers should refer to the historical perspective and research trends summarized in the survey paper by Broussley (ca. 1999) [23]. Example studies over the past fifteen years include the intercalation of carbon fiber micro-electrodes [24], the impact of carbonate solvents [25], and mechanical/thermal stress due to intercalation [26, 27]. The impact of structural design has also been considered with respect to optimal porosity [28] and conductivity in olivine [29].

A subset of this literature considers modeling degradation in lithium-ion batteries, including phenomena such as solid electrolyte interphase (SEI) layers, dendrite formation, carbon dissolution, electrolyte degradation, and electrode structural distortion. Excellent reviews by Aurbach [30], Arora [31], and Kanevskii [32] survey these various mechanisms in depth. In this dissertation we leverage a model particularly well-suited for model reduction and control applications that accounts for lithium diffusion dynamics, intercalation kinetics, and electrochemical potentials developed by Doyle, Fuller, and Newman [33, 34]. Ramadass *et al.* [7] added a degradation component to this model by including an irreversible solvent reduction reaction at the anode-side solid/electrolyte interface that generates a resistive film which consumes cyclable lithium. This mechanism has been identified as one of the chief contributors to capacity and power fade, whose effect is also representative of other mechanisms.

A more detailed overview of battery damage processes is provided in Section 2.1.1.

1.2.2 Optimal Supervisory Control

The second relevant body of research considers optimal supervisory control. Specifically, we focus our attention to the power management problem in hybrid vehicles. An excellent overview of this research area ca. 2007 is provided by Sciarretta and Guzzella [35].

Deterministic dynamic programming generates provably optimal performance, yet requires exact knowledge of the input signal, i.e. drive cycle [36, 37, 38, 39]. In many cases, it is impossible to know the exact input *a priori*. However, it is often possible to identify and optimize with respect to the statistics of the input signal by modeling it as a random process. This idea motivates the use of stochastic dynamic programming, which generates a supervisory controller that is optimal with respect to the expected input behavior [37, 40, 41, 42].

Dynamic programming approaches are generally computed off-line and are optimal only with respect to a model - our mathematical idealization of the actual plant. In contrast, model predictive control methods are generally computed on-line. Namely, they determine optimal state and control trajectories over a receding time horizon using a predictive model and implement only the subsequent step. Real-time optimization necessities the use of relatively simple models, however the initial state can be recalibrated using measurement signals at each time step [43, 44]. Yet another concept, called Equivalent Consumption Minimization Strategy (ECMS), applies an instantaneous optimization procedure which minimizes the energetic equivalent fuel consumption of both engine fuel and electric battery energy [45, 46]. Recently several researchers have shown that this formulation is in fact a physical interpretation to instantaneous optimization using Pontryagin's minimum principle [47, 48, 49].

This body of research has considered various hybrid vehicle configurations, such as engine/battery [50], fuel cell/battery [37], fuel cell/ultracapacitor [46], ultracapacitor/battery [51], and engine/hydraulics [52]. These strategies are typically optimized for objectives such as fuel consumption [37, 52, 45, 46, 43, 38, 39, 51, 41, 50], emissions [53], drivabilitiy [54], and/or combined fuel/electricity consumption [55, 42]. For PHEVs, several studies (e.g. [38]) have identified that the optimal strategy rations battery charge such that it reaches the minimum value exactly when the trip terminates. However, exact *a priori* knowledge of drive cycle behavior and length is typically not available. Moreover, there has been no work performed on optimizing

vehicle power management for battery health. In this dissertation, we shall consider battery health as an objective and directly encode trip length distribution information into the problem formulation.

1.2.3 Estimation Techniques for Li-ion Batteries

Although there have been few publications on *controlling* battery health degradation, the concept of modeling battery degradation in terms of charge capacity fade and increased internal resistance spawned a body of research known as state-of-health (SOH) estimation. Although this dissertation does not explicitly make contributions to SOH estimation, this body of literature is closely related and worth mentioning vis-à-vis the work presented here.

Research on SOH estimation generally uses empirical equivalent circuit battery cell models to estimate charge capacity and internal resistance. Various algorithms have been investigated, including batch data reconciliation, moving-horizon parameter estimation [56], recursive least squares [57], subspace parameter estimation [58], slide-mode observers [59], impedance-based Kalman filters [60], and extended Kalman filtering [61, 62, 63]. The key advantage of these equivalent circuit model-based methods lie in their relatively low complexity. However, the state and parameter values correspond to phenomenological effects as opposed to the true physical values. Moreover, validation of these estimation algorithms is very difficult using in-situ methods [64].

More recently electrochemical models have been utilized in estimation algorithms. For example Smith *et al.* [65], Di Domenico *et al.* [66], and Klein *et al.* [67] respectively used linear Kalman filters, extended Kalman filters, and PDE observers to estimate the internal spatial-temporal states (i.e. Li-ion concentrations) of reduced order electrochemical models derived from [33, 34]. These investigations do not estimate SOH-related parameters. Combining state estimation with SOH-related parameter estimation is a difficult task for two reasons. First, the electrochemical models have 10's of parameters which relate directly to capacity and power fade. Secondly, these parameters vary at significantly slower rates than the concentration dynamics. One recently reported approach uses an Unscented Kalman filter (UKF) in combination with least squares parameter identification [68]. Specifically, the UKF estimates the concentration states and least squares is employed every five cycles to identify the cathode porosity and electrolyte conductivity.

Tangent to model-based battery estimation is prognostics. These studies focus on

predicting when a battery reaches its end-of-life, rather than identifying the exact SOH parameter values. Some of the techniques employed for battery health prognostics include particle filters [69, 70] and mechanical fatigue inspired-approaches [71, 72]. Nonetheless, none of these estimation or prognostic approaches seek to manage or at least mitigate battery health degradation via electrochemical modeling and optimal control.

Prior to this dissertation, fundamental battery research and optimal supervisory control have been largely separate bodies of knowledge. Our focus is to investigate the interaction between electrochemical physics and control systems. Yet, the fusion of these two topics contains several technical challenges.

1.3   Technical Challenges

The design of optimal supervisory controllers for battery energy storage systems is particularly challenging for the following reasons:

- The material properties, energy storage dynamics, health degradation mechanisms, and operating scenarios can vary widely from one battery to another. Therefore a fundamental framework for analyzing battery-health conscious power management is required.

- The dynamics of electrochemical battery models are generally too complex for control design. These challenges are underscored in the context of this dissertation, which utilizes dynamic programming techniques that suffer from the "curse of dimensionality". Innovative model reduction, optimal control solution, and validation approaches are required.

- The input signals are stochastic. That is, the load profiles (e.g. drive cycles, charge/discharge cycles) are typically unknown *a priori*. However the statistics of these inputs may be known. Therefore, new stochastic modeling and control techniques are required.

- Optimal power management is, by itself, a non-trivial problem that requires the solution of an optimal control problem with multiple inputs, stochastic dynamics, state and control constraints, and multiple objectives. A fundamental framework which considers all these features is required.

1.4   New Contributions

The overarching goal of this dissertation is to link battery electrochemistry with optimal supervisory control to enhance battery lifetime. This objective is comprised of three categories of contributions to knowledge on battery systems and control for energy systems:

Model Development of Battery-Electric Systems (Chapter 2)

- *Integration of PHEV drivetrain and electrochemical battery models:*   A first-principles partial differential algebraic equation based electrochemical model is coupled together with PHEV drivetrain models, for the first time. (Sections 2.1 - 2.2)

- *Model of power-split PHEV:* An established power-split HEV model from Liu [73] is augmented with a high-energy capacity Li-ion battery model, engine start/stop dynamics, and higher accuracy actuator/state constraints. (Section 2.2)

- *Markov chain model of drive cycle dynamics and daily trip length:* Markov chain models of drive cycles are not new [37, 73, 41, 48]. However, the direct incorporation of daily trip length distributions via an identified absorbing state in the Markov chain is new. (Section 2.3)

Power Management via Stochastic Optimal Control (Chapter 3)

- *An energy consumption cost objective:* This objective function includes the monetary cost of fuel and electricity, sourced from the gas pump and electric utility, respectively. This objective represents the true utilization cost of a *plug-in* hybrid electric vehicle. (Section 3.1)

- *Numerical techniques for constrained SDP problems:* Many past methods enforce constraints through penalty functions [37, 73, 53] - a soft constraint method. In this dissertation we calculate the sets of admissible controls offline. These sets then become the admissible decision space over which optimization occurs online. Hence the constraints are hard. (Section 3.1.2)

- *Integration of high fidelity and reduced battery models into SDP formulation, solution, and analysis:* The full model is used for determining the sets of admissible controls and evaluating the resulting controllers. The reduced model is used for control optimization. This ensure the constraints of the full model are satisfied while retaining the numerical tractability of dynamic programming. (Section 3.4)

- *Analysis of optimal blending versus charge depletion-charge sustenance (CDCS):* This analysis reveals how a power-split architecture and charge depletion strategy add an additional degree of freedom to regulate engine operation around its most efficient region. (Section 3.2.2)

- *Sensitivity to battery size, daily trip distance, and energy price :* The sensitivity of optimal blending performance is evaluated against varying model parameters and input conditions. This analysis demonstrates when blending provides the greatest and least performance improvement over CDCS. (Section 3.3)

- *Battery-health conscious power management:* This power management formulation considers battery health with energy consumption cost, for the first time. The example battery health metrics we analyzed include SEI layer growth and charge processed. (Section 3.4 - 3.5)

- *Relationships between optimal control and fundamental plant physics:* Analysis of the optimal control solutions reveals which physical plant properties enable improved performance through control. Example include the analysis of optimal blending (Section 3.2.2) and battery health conscious power management (Section 3.4 - 3.5)

Health-Conscious Battery Charge Management (Chapter 4)

- *Switching control paradigm for unequal charging of batteries connected in parallel:* Conventionally, all batteries connected in parallel are constrainted to equal charge levels. This concept explores how unequal yet controlled charge levels may improve battery pack life. (Chapter 4)

- *Optimal control problem formulation including high fidelity and reduced order battery models with degradation:* The optimal switching sequence for health is

determined via deterministic dynamic programming. Control optimization is performed on a reduced degrading battery model (4.2), while control evaluation is performed on a full order degrading battery model (Section 4.4.2).

- *Relationships between optimal control and degradation mechanism properties:* This analysis reveals that unequal charge levels for batteries connected in parallel provide advantages when certain concavity features exist in the physical degradation mechanisms. (Section 4.3.3)

- *Extraction of state-feedback rules:* Analysis of the optimal trajectories reveals time-invariant patterns which are approximated by a "heuristic" state feedback control algorithm. Similar ideas have been explored by Lin [37], Kum [53] and their colleagues. (Section 4.3)

- *Sensitivity to alternative degradation models:* The robustness of these results are evaluated against alternative degradation models taken from literature and experimental data. (Section 4.4)

The research reported throughout this dissertation is based primarily on a series of publications by the author and his colleagues [55, 42, 74, 75, 76, 77, 10, 78].

1.4.1 Impact on Related Efforts

In addition to the core contributions described above, the work presented in this dissertation has had notable impact on several related efforts, which we list here.

Battery Experiments: A custom-built battery-in-the-loop test system was developed to identify the electrochemical model described in Chapter 2. This test facility will also be utilized for future projects involving control system prototyping of battery management systems. Appendix A contains a complete description of this experimental rig and its components. This experimental effort also paved the way for new multi-channel battery testing facilities and float charging equipment to obtain data-driven models of health degradation.

Extremum Seeking Control of Alternative Energy Conversion Devices: Extremum seeking (ES) deals with the problem of regulating a system to an unknown optimal set-point, which may be time-varying [79]. This effort consists of developing new theoretical advancements and applications of ES to fuel cell [80] and photovoltaic systems [81].

Vehicle-to-Grid Integration: The PHEV models and supervisory control algorithms developed in Chapters 2 and 3, respectively, were utilized to develop optimal grid-to-vehicle charging profiles [82] and predict PHEV-related power demand on the grid [83]. This work forms the foundation for broader research questions on energy management in smart-grid systems.

PDE Control: New theoretical developments in the area of PDE-based optimal control and estimation are currently underway [84]. These theoretical developments are motivated by the lack of control and estimation tools for the PDE-based battery model described in Chapter 2.

Education on Battery Systems and Control: This dissertation has had a direct impact on a new course developed at the University of Michigan entitled "Battery Systems and Control." The course disseminates knowledge gained from this research to practicing engineers. Designing and delivering such a course is a unique opportunity among doctoral students. A high-level description of this course is provided in Appendix B, which is roughly based upon an education-focused publication by the course instructors [85].

1.5   Dissertation Organization

This dissertation is organized as follows. Chapter 2 develops the mathematical models for the electrochemical battery physics, PHEV powertrain, and drive cycle dynamics. These models are used for control design in the subsequent two chapters. Chapter 3 investigates battery health conscious supervisory control algorithms for PHEVs. Chapter 4 examines the potential of unequal charge levels in parallel-connected batteries through optimal control. Finally Chapter 5 summarizes the main results of this dissertation, its original contributions, and possible future research directions.

Chapter 2

Model Development

This chapter introduces the physical dynamic system models used throughout this dissertation. These include models of the lithium-ion battery concentration dynamics, lithium-ion battery health degradation, plug-in hybrid electric vehicle (PHEV) powertrain, and stochastic drive cycles.

2.1 Li-ion Batteries

In the following, we review the fundamentals of battery operation and provide an overview of the important degradation mechanisms in Li-ion batteries. Next we develop two types of battery cell models: electrochemical and equivalent circuit. Following this discussion, we describe two battery health degradation models/metrics utilized in the optimal control studies. Finally, we discuss the construction of battery pack models from cells.

2.1.1 Battery Fundamentals

Jumping Frog Legs: A Brief History of the First Battery

The first battery cell was invented by Italian physicist Alessandro Volta in 1800 (see Fig. 2.1). The so-called voltaic pile consisted of two metals in series, zinc and copper, coupled by a sulphuric acid electrolyte. Volta was inspired to construct this system in response to experiments performed by his colleague Luigi Galvani (Fig. 2.1), also an Italian physicist. Galvani was interested in the interaction between electricity and biological nervous systems. During his experiments, Galvani discovered that a dead frog's legs would kick to life when in contact with two dissimilar metals. Galvani called this phenomenon "animal electricity" and theorized it resulted from an electrical fluid

Allesandro Volta (1745-1827)   **Luigi Galvani** (1737-1798)
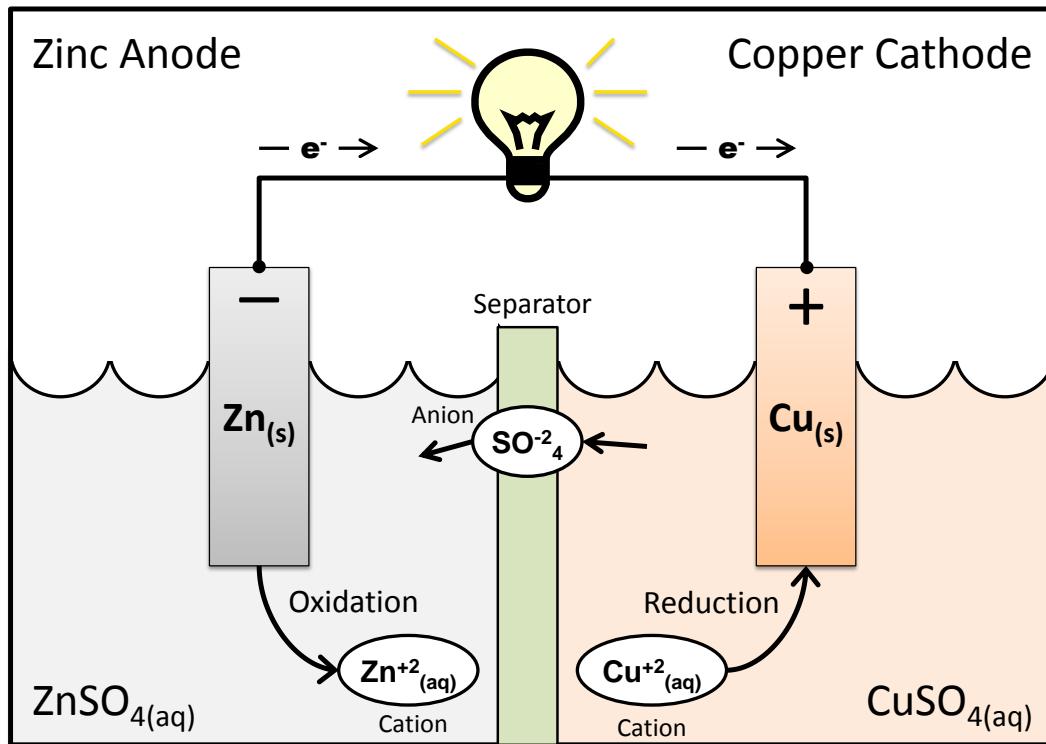
Figure 2.1 Alessandro Volta (left) [3] and Luigi Galvani (right) [4]. Volta is credited for inventing the first battery cell, the voltaic pile, in an effort to further investigate Galvani's experimental findings in "animal electricity". Both images are available to the public domain from Wikimedia Commons.

within the nervous system. Volta, on the contrary, reasoned that this behavior was caused by the different metals. The voltaic pile described above proved Volta's theory to be true.

Principles of Operation

A battery, put simply, converts chemical energy to and from electrical energy through an oxidation-reduction (redox) reaction. It consists of two dissimilar metals (the electrodes) connected by an electrolyte. The electrodes are electrically isolated from one another via a separator. Hence, as the redox reactions occur, cations flow between the electrodes through the electrolyte while electrons are forced through an external electric circuit. This process is sometimes reversible when an external electric potential is applied. This process is demonstrated by the zinc-copper Galvanic cell in Fig. 2.2.

Fundamentally, all electrochemical cells operate under this principle. The important differences between types of battery cells relate to varying electrode and electrolyte materials. Electrode and electrolyte materials are typically selected for their voltage, charge capacity, conductivity, weight, cost, reactivity with other components, ease of handling, ease of manufacturing, etc. [17]. For example, lithium-ion cells have become very attractive in mobile applications [86, 19] because lithium is the lightest (6.94

Figure 2.2 An example zinc-copper Galvanic (or Voltaic) cell demonstrating the principles of operation for an electrochemical cell.

g/mol) and most electropositive (-3.01V vs. standard hydrogen electrode) metal in the periodic table. Lead acid cells feature relatively heavy electrode materials (Pb and PbO$_2$), yet these cells can provide high surge currents and are cost effective. As a final example, lithium-air batteries feature cathodes that couple electrochemically with atmospheric oxygen, thus producing energy densities that rival gasoline fuel [87].

Overview of Degradation Mechanisms

In addition to the operating principles described above, batteries undergo various degradation mechanisms that cause capacity and power fade. These mechanisms include dendrite formation, electrode chemical and/or structural distortion, electrolyte decomposition, and solid electrolyte interphase (SEI) layers. Excellent reviews of these damage mechanisms and more are reported in [30, 31, 32]. Below we provide an overview of the four mechanisms described above.
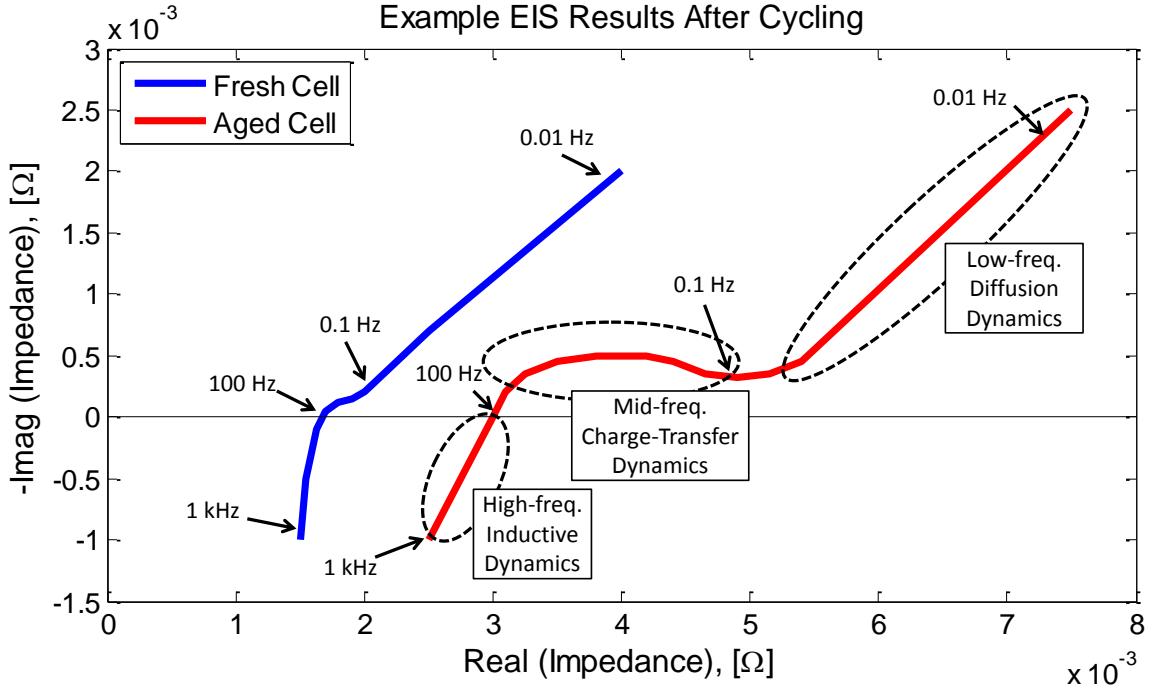
In lithium or lithium-ion batteries, dendrite formation refers to the uneven growth of Li-metal, particularly in negative lithium or carbonaceous electrodes. These den-

dritic structures can eventually pierce the separator material and cause a short-circuit. Once this occurs, rapid overheating and possibly combustion ensues. Dendrites growth can occur as a result of overcharging or rapid charging, where Li is deposited into the dendritic structures as opposed to intercalating within the negative electrode material [88]. Solutions to this problem generally include different electrode/electrolyte combinations or coating the negative electrode [22].

The electrode material in either electrode may degrade chemically and/or structurally for a number of reasons. For example, mechanical stress induced during intercalation and deintercalation can produce distortions in the crystal structure [26]. To partially overcome this limitation $LiFePO_4$ utilizes olivine structures over spinel (in e.g. $LiCoO_2$ and $LiMnO_2$) which are generally more stable [20]. Another example is that cyclable lithium ions may can be consumed by the formation of a resistive surface layer through chemical decomposition. This manifests itself externally as both capacity and power fade. This process could occur at the anode [30] or cathode [89], depending on the electrode/electrolyte combination and operating conditions.

A third failure mechanism is electrolyte decomposition. Reduction of the electrolyte material (particulary at the electrode surface) can consume salt and solvent species, therefore impacting diffusion rates and conductivity [22]. Electrolyte reduction may also produce gaseous products which increase internal pressure and ultimately cause catastrophic failure [31]. As such, there exists ongoing investigations to find new electrolyte materials, such as polymer electrolytes [21] or vinylene carbonate additives [90].

The fourth failure mechanism involves the SEI layer. Several experimental studies have identified lithium-consuming SEI as an important mechanism for capacity fade for cells with $LiFePO_4$ cathodes and carbon anodes. These studies include ex-situ analyses [91, 92], in-situ analyses [93, 94], and cell design modifications that mitigate SEI layer growth [95, 90, 96]. For example, Amine et al. reported on a series of electrochemical impedance spectroscopy (EIS), Raman, and transmission electron microscopy (TEM) tests were carried out on pouch-type $LiFePO_4$-graphite cells following cycling [95]. These tests identified an increased SEI layer on the graphite anode via EIS testing. For an excellent review EIS for determination of SOC and SOH, see Huet [97]. After 50 cycles at an elevated temperature of 55°C, the anode contributes nearly 90% of the total cell impedance. More specifically, the semi-circular portion of the EIS curve increased most notably. The frequency range of this semi-circle corresponds directly with the charge-transfer dynamics associated with the resistive SEI film. An example of this behavior is illustrated in Fig. 2.3. After cycling, the cell was disassembled

Figure 2.3 EIS results for a fresh and aged Li-ion battery cell. Note the increase in size of the semi-circular shaped mid-frequency region, related to the charge-transfer dynamics. This corresponds to a growing SEI layer. Note that the data was synthesized for tutorial purposes and not taken from real measurements.

and energy-dispersive X-ray spectroscopy was performed on the anode. The results indicate the presence of Fe metal at the graphite surface. These authors hypothesize that Fe^{2+} dissolved from the cathode surface due to HF acid in the electrolyte, diffused from the cathode into the anode, formed deposits on the negative electrode, and ultimately catalyzed the interfacial impedance in the anode. This phenomenon has been observed in a number of other studies, including [91, 90, 96].

Several researchers have proposed design modifications to C-LiFePO$_4$ cells to mitigate the deposition of iron on the negative electrode and SEI film growth. For example, Amine *et al.* proposed a LiTi$_5$O$_{12}$ spinel anode in which the relatively high equilibrium potential of 1.5V vs. pure Li should theoretically reduce the reduction of Fe-ions on the electrode surface [95] In addition, they studied a LiBOB-based electrolyte which was shown to suppress the erosion of Fe from the LiFePO$_4$ cathode. Wu et al. investigated the addition of vinylene carbonate (VC) in the electrolyte solution, which dramatically suppresses the dissolution of Fe from the LiFePO$_4$ [90]. Finally, Chang et al. studied how various metal coatings of the carbon negative electrode may improve capacity life [96]. These authors found Au and Cu act as a

sieve to collect dissolved Fe ions resulting from LiFePO$_4$ corrosion, preventing Fe from diffusing within the interior of the carbon electrode and catalyzing SEI formation.

To contain this dissertation's scope, we focus our modeling and control efforts on SEI layer growth and other metrics of aging (Ah-processed). Yet, the methods are generalizable to other damage mechanisms - a key feature for extending and adapting this work.
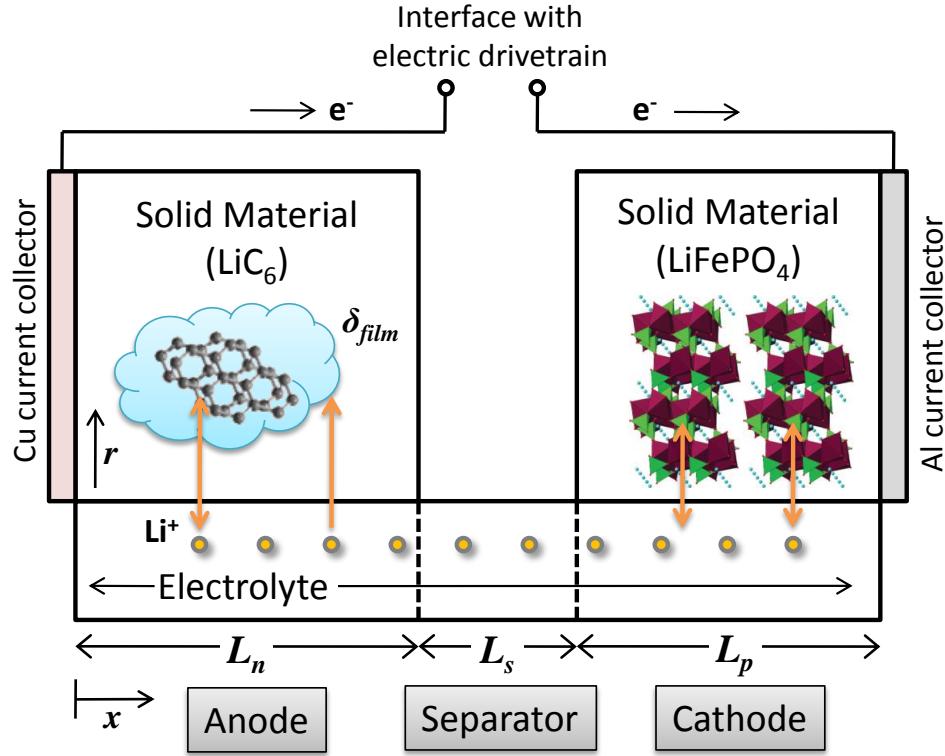
2.1.2 Battery Cell Models

Two battery models are considered in the control design and analysis process. A high-fidelity electrochemical-based model is used for constraint satisfaction and closed-loop simulation. A low-order equivalent circuit model is used for control optimization, since it has one state variable. The parameters of both models have been identified experimentally on a custom-built hardware-in-the-loop setup, for commercial Li-ion cells containing LiFePO$_4$ cathode chemistries [98]. Interested readers my refer to [10] for further details on the genetic optimization procedure used to identify the parameters of the electrochemical model. In the following we summarize the electrochemical battery model and equivalent circuit model.

Electrochemical Battery Model

The electrochemical battery model captures the spatiotemporal dynamics of lithium-ion concentration, electrode potential in each phase, and the Butler-Volmer kinetics which govern the intercalation reactions. A schematic of the model is provided in Fig. 2.4. This cross section displays three regions: a negative electrode (typically a lithium-carbon material), the separator, and a positive electrode (typically a lithium metal oxide). Each region is denoted by the subscript $j \in \{n, s, p\}$ representing the negative electrode, separator, and positive electrode respectively. The positive electrode material varies widely across manufacturer designs. However lithium iron phosphate (LiFePO$_4$) cells were used to identify this electrochemical model. Each electrode region contains two phases, the porous solid and electrolyte. The separator has an electrolyte phase only.

Mathematically, the electrochemical model structure is a coupled set of partial differential-algebraic equations. Parameter definition and values are provided in Table 2.1. Diffusion of lithium ions in the solid $c_{1,j}(x, r, t)$ is idealized by spherical diffusion. Diffusion of lithium ions across the electrolyte $c_{2,j}(x, t)$ is modeled by linear diffusion in

Figure 2.4 Structure of the electrochemical Lithium-ion battery cell model.

Cartesian coordinates. Respectively, these phenomena are represented mathematically by:

$$\frac{\partial c_{1,j}}{\partial t}(x,r,t) = \frac{D_{1,j}}{r^2}\frac{\partial}{\partial r}\left(r^2\frac{\partial c_{1,j}}{\partial r}\right) \tag{2.1}$$

$$\varepsilon_{2,j}\frac{\partial c_{2,j}}{\partial t}(x,t) = D_2^{eff}\frac{\partial^2 c_{2,j}}{\partial x^2} + \frac{1-t^+}{F}J_j \tag{2.2}$$

where the variable J_j represents the local volumetric transfer current density due to Li-ion intercalation at the solid/electrolyte interface, $D_{1,j}$ and D_2^{eff} are the diffusion coefficients for the solid and electrolyte phases, t^+ is the transference number, and F is Faraday's constant.

The boundary conditions for spherical diffusion of lithium ions in the solid phase are given by:

$$\left.\frac{\partial c_{1,j}}{\partial x}(x,r,t)\right|_{r=0} = 0 \tag{2.3}$$

$$\left.\frac{\partial c_{1,j}}{\partial x}(x,r,t)\right|_{r=R_s} = -\frac{1}{D_{1,j}a_j F}J_j(x) \tag{2.4}$$

where a_j is the specific surface area of the porous electrode. The second boundary condition (2.4) models the rate at which lithium ions are exchanged between the solid and electrolyte phases through intercalation at the particle surface $(r = R_s)$. The first boundary condition (2.3) results from spherical symmetry.

The boundary conditions for diffusion in the electrolyte are also Neumann-type, and are given as follows:

$$\frac{\partial c_{2,j}}{\partial x}(x,t)\Big|_{x=0} = \frac{\partial c_{2,j}}{\partial x}(x,t)\Big|_{x=L_n+L_s+L_p} = 0 \tag{2.5}$$

$$D_{2,eff,n}\frac{\partial c_{2,j}}{\partial x}(x,t)\Big|_{x=L_n} = D_{2,eff,s}\frac{\partial c_{2,j}}{\partial x}(x,t)\Big|_{x=L_n} \tag{2.6}$$

$$D_{2,eff,s}\frac{\partial c_{2,j}}{\partial x}(x,t)\Big|_{x=L_n+L_s} = D_{2,eff,p}\frac{\partial c_{2,j}}{\partial x}(x,t)\Big|_{x=L_n+L_s} \tag{2.7}$$

The first boundary condition (2.5) says there is no mass flow of lithium-ions outside the anode-separator-cathode sandwich. The subsequent two boundary conditions (2.6)-(2.7) are continuity conditions at the anode-separator and separator-cathode interfaces.

The electric potential of each phase (solid: $\phi_{1,j}$, electrolyte: $\phi_{2,j}$) within each region is determined by a parameter distributed form of Ohm's law. In the solid and electrolyte, this is given respectively by:

$$J_j(x,t) = \frac{\partial}{\partial x}\left(\sigma_j^{eff}\frac{\partial \phi_{1,j}}{\partial x}\right) \tag{2.8}$$

$$J_j(x,t) = \frac{\partial}{\partial x}\left(\kappa^{eff}\frac{\partial \phi_{2,j}}{\partial x}\right) + \frac{\partial}{\partial x}\left(\kappa\frac{\partial \ln c_{2,j}}{\partial x}\right) \tag{2.9}$$

The first terms in each equation above represent flux due to potential gradients. The second term in (2.9) represents the flux due to ionic concentration gradients in the electrolyte. The conductivities σ_j^{eff}, κ^{eff}, and κ are included in the partial derivatives because they vary with concentration which varies in space.

The model inputs (and outputs) are defined by the boundary conditions of the electric potential equations. When current is the input (i_{app}) the model runs in galvanostatic mode and voltage is defined. When voltage is the input (V_{app}) the model runs in potentiostatic mode and current is defined. All potentials are defined relative to the potential of the anode's solid phase at $x = 0$. These conditions are given as

follows:

$$\left.\frac{\partial \phi_1}{\partial x}(x,t)\right|_{x=L_n+L_s+L_p} = \frac{1}{A\sigma_{eff}}i_{app} \tag{2.10}$$

$$\phi_1(x)|_{x=L_n+L_s+L_p} = V_{app} \tag{2.11}$$

$$\phi_1(x)|_{x=0} = 0 \tag{2.12}$$

The remaining boundary conditions for the potential equations are continuity conditions.

$$\left.\frac{\partial \phi_1}{\partial x}(x)\right|_{x=L_n} = \left.\frac{\partial \phi_1}{\partial x}(x)\right|_{x=L_n+L_s} = 0 \tag{2.13}$$

$$\left.\frac{\partial \phi_2}{\partial x}(x)\right|_{x=0} = \left.\frac{\partial \phi_2}{\partial x}(x)\right|_{x=L_n+L_s+L_p} = 0 \tag{2.14}$$

$$\kappa^{eff}(c_2(x))|_{anode}\frac{\partial \phi_2}{\partial x} + \kappa(c_2(x))|_{anode}\left.\frac{\partial \ln(c_2)}{\partial x}(x)\right|_{x=L_n}$$
$$= \kappa^{eff}(c_2(x))|_{separator}\frac{\partial \phi_2}{\partial x} + \kappa(c_2(x))|_{separator}\left.\frac{\partial \ln(c_2)}{\partial x}(x)\right|_{x=L_n} \tag{2.15}$$

$$\kappa^{eff}(c_2(x))|_{separator}\frac{\partial \phi_2}{\partial x} + \kappa(c_2(x))|_{separator}\left.\frac{\partial \ln(c_2)}{\partial x}(x)\right|_{x=L_n+L_s}$$
$$= \kappa^{eff}(c_2(x))|_{cathode}\frac{\partial \phi_2}{\partial x} + \kappa(c_2(x))|_{cathode}\left.\frac{\partial \ln(c_2)}{\partial x}(x)\right|_{x=L_n+L_s} \tag{2.16}$$

The intercalation current J_j is governed by Butler-Volmer kinetics in (2.17), where η_j is the local overpotential defined by (2.18).

$$J_j(x,t) = a_j i_{0,j}\sinh\left(\frac{\alpha_{a,j}F}{RT}\eta_j\right) \tag{2.17}$$

$$\eta_j(x,t) = \phi_{1,j}(x,t) - \phi_{2,j}(x,t) - U_{ref,j}(\theta_j) - \frac{J_j}{a_n}R_{film} \tag{2.18}$$

The term $U_{ref,j}$ is the reference potential of the corresponding electrode, and is a function of the bulk electrode SOC θ_j. The term R_{film} is the resistance of the SEI layer and is described in detail in Section 2.1.3. From a supervisory control systems perspective, we define the total battery SOC to be the spatially averaged SOC of the anode. This definition allows us to distill the stored charge of the electrochemical

21

battery model into a single number.

Leveraged Model Reduction Techniques

In total, the electrochemical battery model is a system of partial differential algebraic equations. Moreover, these equations apply over three different regions, in which two regions contain multiple phases. Finally, there exist two spatial dimensions in the electrode solid phase. This complexity makes control design difficult. Even numerical simulation, by itself, is an extremely non-trivial task. In this dissertation we leverage the model reduction techniques co-developed in the laboratory group to solve these electrochemical model equations orders of magnitude faster than real-time. These techniques include: (1) Padé approximations of the spherical diffusion equations, which significantly reduce the number of states relative to finite differencing methods; (2) Real-time linearization (a.k.a. quasi-linearization) of the Butler-Volmer equations, which breaks the nonlinearity present in the algebraic equations and allows one to transform the model into a set of ODEs; (3) Projection of the states onto Legendre polynomials, which ultimately reduces the number of states relative to finite differencing. Readers interested in the complete details of the model reduction techniques should refer to [99].
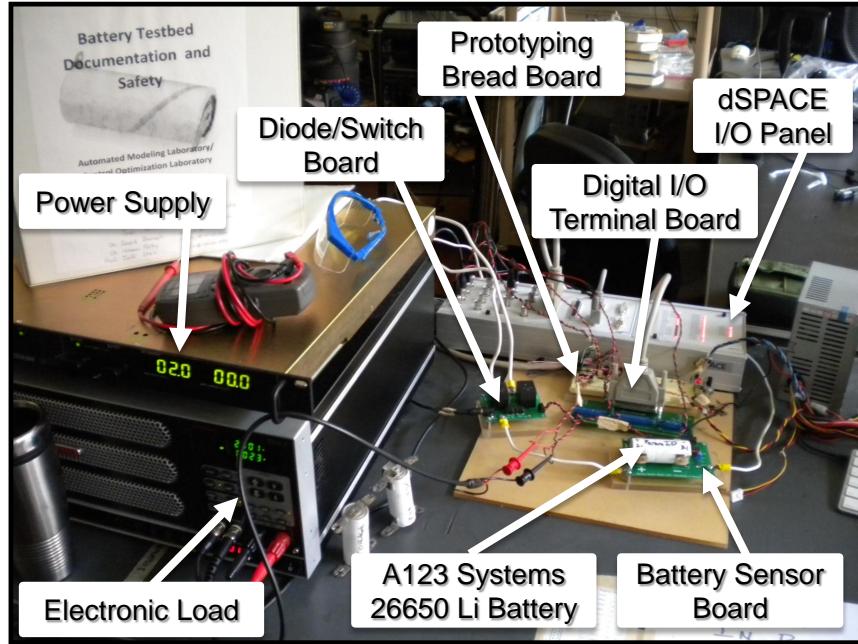
Parameter Identification of the Electrochemical Model

A genetic identification procedure was utilized to determine the electrochemical model parameters. The actual parameter identification procedure, results, and analysis are not products of this dissertation. However, the resulting identified model is utilized by this dissertation for control design purposes. As such, we describe the process at a high level. Interested readers should refer to Forman *et al.* [10] for more details. The identified parameters are reported in Table 2.1 and Appendix D.

Fitting and validation data has been collected from a custom-designed battery-in-the-loop test system, shown in Fig. 2.5, fabricated for this very purpose. Appendix A describes the details of fabricating this system. The data was obtained from $LiFePO_4$ ANR26650M1A battery cells with a 2.3 amp-hour capacity, a nominal voltage of 3.3 volts, and a maximum continuous discharge current of 70 amps (30.4 C-rate). These cells are designed for transient high power applications including commercial PHEVs and portable power tools.

A variety of different cycles were used for obtaining model identification and

validation data. These cycles include a CCCV chirp cycle, two naturalistic driving cycles, and four government certification driving cycles. The chirp cycle consists of five CCCV charge/discharge patterns between 2.0V - 3.6V with charge/discharge rates of 5C, 2.5C, and 1C. The naturalistic driving cycles were provided by the University of Michigan Transportation Research Institute (UMTRI). This data has been collected using real world drivers in midsized sedans equipped with over 200 data acquisition channels [100]. An individual's morning and evening commute were recorded to create the Naturalistc1 and Naturalistc2 drive cycles. The last four cycles, UDDSx2, US06x3, SC03x4, and LA92x2, are based on vehicle certification tests. The "x" indicates the number of times each drive cycle is repeated. Current profiles were generated from all six drive cycles by simulating the midsize power-split PHEV described in Section 2.2 using controllers from Chapter 3. For consistency, each experiment begins with the battery at 90% SoC (3.35V relaxed). Due to sensor limitations, drive cycles which contain current magnitudes greater than 20A have been uniformly scaled down to have maximum magnitudes of 20A: US06x3, SC03x2, and LA92x2. These seven cycles provide a rich data set for performing parameter identification and validation on a battery model intended for PHEV-centric studies. The results of this effort are reported in [10].

Figure 2.5 Photo of battery-in-the-loop hardware configuration.

Table 2.1 Electrochemical Model Parameters

Parameter	Description	Value
L_n	Length of anode	2.8853×10^{-5} m
L_s	Length of separator	1.6971×10^{-5} m
L_p	Length of cathode	6.5205×10^{-5} m
R_n	Radius of anode spherical particles	3.5961×10^{-6} m
R_p	Radius of cathode spherical particles	1.6371×10^{-7} m
$c_{1,n,max}$	Max concentration of anode solid	2.9482×10^4 mol/m^3
$c_{1,p,max}$	Max concentration of cathode solid	1.0355×10^4 mol/m^3
$D_{1,n}$	Diffusion coefficient in anode solid	8.2557×10^{-14} m^2/s
$D_{1,p}$	Diffusion coefficient in cathode solid	1.7362×10^{-14} m^2/s
D_2	Diffusion coefficient of electrolyte	6.9114×10^{-10} m^2/s
$\varepsilon_{1,n}$	Porosity of solid in anode	0.3810
$\varepsilon_{1,p}$	Porosity of solid in cathode	0.4800
$\varepsilon_{2,n}$	Porosity of electrolyte in anode	0.6190
$\varepsilon_{2,s}$	Porosity of electrolyte in separator	0.3041
$\varepsilon_{2,p}$	Porosity of electrolyte in cathode	0.5200
σ_n	Conductivity of anode solid	$100 \ (\Omega \ \text{m})^{-1}$
σ_p	Conductivity of cathode solid	$100 \ (\Omega \ \text{m})^{-1}$
A	Cross-sectional area	0.3108 m^2
a_n	Specific surface area of porous anode	3.1785×10^5 m^2/m^3
a_p	Specific surface area of porous cathode	8.7965×10^6 m^2/m^3
α	Electrode transfer coefficients	0.5
b	Bruggeman's number	1.452
k_n	Kinetic rate constant in anode	8.6963×10^{-7} $(\text{A/m}^2)(\text{mol/m}^3)^{1+\alpha}$
k_p	Kinetic rate constant in cathode	1.1267×10^{-7} $(\text{A/m}^2)(\text{mol/m}^3)^{1+\alpha}$
R_{SEI}	Initial SEI resistivity	3.691×10^{-3} Ω m^2
t^+	Transference number	0.2495
T	Cell temperature	298.2 K

Equivalent Circuit Model

Although the electrochemical model predicts the spatiotemporal concentration and potential dynamics of a battery cell, its complex structure is not easily conducive to optimal control. This fact motivates the use of a reduced equivalent circuit model with a single state. This model idealizes the battery as an open circuit voltage in series with an internal resistance. Both elements are continuous functions of SOC. Electric

power at the battery terminals P_{batt} is the input, resulting in the following dynamics:

$$\dot{SOC} = -\frac{V_{oc} - \sqrt{V_{oc}^2 - 4P_{batt}R_{batt}}}{2Q_{batt}R_{batt}} \qquad (2.19)$$

To calculate the current I and voltage V_{cell} across each cell, one must know the battery pack configuration. That is, how many cells are arranged in series to produce the desired pack voltage, and how many parallel strings exist to achieve the desired energy capacity. Here we assume the use of 2.3 Ah 26650 format cells (to be consistent with our experimental batteries) arranged with $n_s = 110$ in series, and $n_p = 6$ parallel strings.

$$I = \dot{SOC} \cdot Q_{batt}/n_p \qquad (2.20)$$

$$V_{cell} = (V_{oc} - IR_{batt})/n_s \qquad (2.21)$$

Each cell is assumed to be identical or properly balanced through appropriate charge equalization schemes [101]. The current through each cell is used to calculate the anode-side film growth rate discussed in Section 2.1.3. The voltage calculation is used to ensure each cell does not exceed safe operating limits - which we implement mathematically as constraints in the problem formulation in Section 4.2.
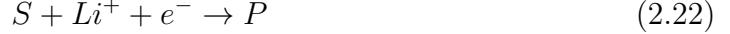
Temperature dynamics and their impact on battery health is also a critical factor to consider [102, 103, 104]. In this work we constrain the scope to batteries whose temperature is controlled around 25° C through appropriate thermal management systems. Nonetheless, one may include thermal dynamics into the presented problem formulation - a topic for future consideration.

2.1.3 Degradation Models

Anode-side Film Growth Model of Battery Aging

In this section we capture battery health degradation by modeling the resistive film which builds up on the anode solid/electrolyte interface [95, 105, 7, 30, 94, 90, 106]. This mechanism effectively consumes cyclable lithium ions and increases the internal impedance. The exact chemical side reaction depends on the chemistry of the electrode and electrolyte. Equations (2.22)-(2.27), developed by Ramadass *et al.* argue that a simple and general method for modeling capacity loss is to assume an irreversible

solvent reduction reaction of the following form

$$S + Li^+ + e^- \rightarrow P \tag{2.22}$$

where S denotes the solvent species and P is the product.

As a result of this irreversible side reaction, the products form a film at the solid/electrolyte interface, which has a time and spatially varying thickness $\delta_{film}(x,t)$ across the anode. This irreversibly formed film combines with the solid electrolyte interphase (SEI) resistance R_{SEI} to compose the total resistance at the solid/electrolyte interface as follows

$$R_{film}(x,t) = R_{SEI} + \frac{\delta_{film}(x,t)}{\kappa_P} \tag{2.23}$$

where κ_P, denotes the conductivity of the film, x is the spatial coordinate, and t is time. The state equation corresponding to the growth of film thickness, due to the unwanted solvent reduction described in (2.22), is given by

$$\frac{\partial \delta_{film}(x,t)}{\partial t} = -\frac{M_P}{a_n \rho_P F} J_{sd}(x,t) \tag{2.24}$$
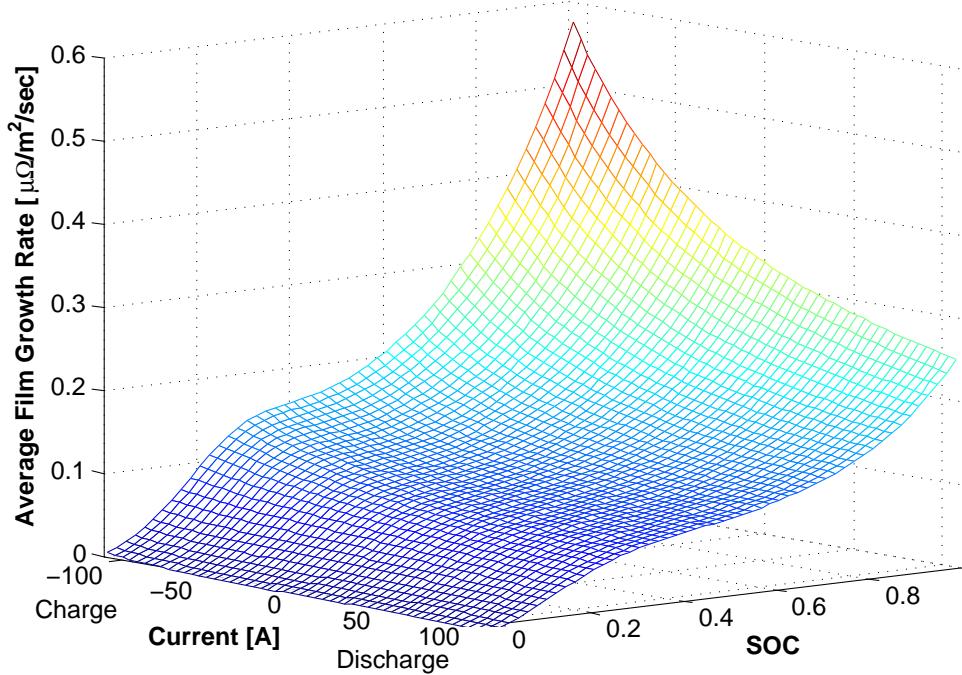
In (2.24), M_P, a_n, ρ_P, and F represent the product's molecular weight, specific surface area, mass density, and Faraday's constant, respectively. The term J_{sd} denotes the local volumetric current density for the side reaction, which is governed by Butler-Volmer kinetics. If the solvent reduction reaction is irreversible and the variation of Li-ion concentration in the electrolyte is small, then we may approximate J_{sd} by the Tafel equation [107].

$$J_{sd}(x,t) = -i_{0,s} a_n e^{\left(\frac{-0.5F}{R_{gas}T}\eta_{sd}(x,t)\right)} \tag{2.25}$$

In (2.25), $i_{0,s}$, R, and T respectively denote the exchange current density for the side reaction, universal gas constant, and cell temperature. The term η_{sd} represents the side reaction overpotential, which drives the solvent reduction reaction in (2.22). The overpotential is calculated according to

$$\eta_{sd}(x,t) = \phi_1(x,t) - \phi_2(x,t) - U_{s,ref} - \frac{J_{tot}(x,t)}{a_n} R_{film}(x,t) \tag{2.26}$$

The variables ϕ_1 and ϕ_2 represent solid and electrolyte potentials, respectively. The symbol $U_{s,ref}$ denotes the equilibrium potential of the solvent reduction reaction, which we assume to be constant. The total intercalation current J_{tot} represents the flow of charge exchanged with the anode-side electrolyte. Specifically, the total intercalation current J_n in the anode is given by the sum of current between the solid and electrolyte

Figure 2.6 Static approximation of film growth rate vs. cell current and SOC utilized for PHEV power management control synthesis.

(J_1), and the solvent reduction reaction and electrolyte (J_{sd}), that is

$$J_n = J_1 + J_{sd} \tag{2.27}$$

Equations (2.23)-(2.27) encompass the film growth subsystem of the Li-ion battery cell model, adopted from [7]. This subsystem connects to the remainder of the battery model (2.1)-(2.18) through the total intercalation current J_n and potentials ϕ_1 and ϕ_2.

Although this model captures complex physical phenomena such as coupled diffusion, intercalation, and film growth processes, its complexity makes control design for health management difficult. Therefore, the present research seeks to use the high fidelity model to generate simpler models for the purposes of control design. In the following, the anode-side film growth degradation dynamics will be approximated by a nonlinear static function, which enables optimal control design. Once the optimal control laws are derived from this approximate model, we simulate the closed-loop system with the full electrochemical model.

To acquire insight on the relationship between battery cell SOC, current, and film growth rate, consider an ideal fresh cell, that is $\delta_{film}(x,0) = 0$. Suppose all the intercalation currents, overpotentials, and concentration profiles are constant with

respect to space and correspond to zero initial applied current. Starting from these initial conditions, we simulate the electrochemical battery cell model for different initial SOC and applied current levels and measure the instantaneous film growth rate. From this data we produce a static relationship mapping cell SOC and applied current to the spatially averaged film growth rate $\dot{\bar{\delta}}_{film}$, shown in Fig. 2.6. The map indicates that film growth rate increases with cell SOC. The film growth rate also increases as the discharge current becomes increasingly negative, i.e. for increasing charge current. Finally, film grows when zero current is applied, indicating that aging occurs even when the cells are not in use - a fact previously reported in the literature [106] and commonly seen in practice. A key question we revisit after obtaining the optimal control solutions is what insight about the structural properties of this map can be leveraged to design supervisory power management controllers that reduce film formation in PHEV battery packs?

The Charge-Processed Model of Battery Aging

In this section we capture battery health degradation dynamics via an empirical result found in numerous experimental studies [108, 109]. Specifically, this model assumes battery SOH degrades in direct proportion to the "charge-processed" through the battery. Physically, this implies that capacity fade mechanisms are insensitive to local SOC levels, depth of discharge, or electrode lithiation rates. Instead, these mechanisms progress in proportion with the integrated number of lithium ions intercalated or de-intercalated into the electrode. Generally speaking, this model suggests batteries degrade as their "mileage" increases. Mathematically, this means

$$\text{Capacity/Power Fade} \propto \int_{\tau=0}^{t} |I(\tau)| \, d\tau \tag{2.28}$$

Both experimental studies utilized C-LiFePO$_4$ cells, which is the chemistry we mostly focus on in this dissertation. However, they also cycled these cells under relatively mild conditions. These conditions are summarized in Table 2.2. In this table, one can see that Peterson *et al.* [108] applied scaled PHEV driving cycle loads. However, these loads were limited between -3C and +1C, which is significantly less than the 30C maximum continuous discharge rate quoted by the manufacturer [98]. Low C-rates (namely C/2) also characterize the experimental results found by Wang *et al.* [109], which use cells from the same manufacturer. In contrast to the first investigation, this work cycled the cells at an elevated temperature of 60°C, which

will induce accelerated capacity fade.

Although it remains an open question whether capacity fade is correlated with SOC or depth of discharge for high C-rates, we consider Ah-processed as a very simple model for battery health degradation. That is, in Chapter 3 we design PHEV supervisory control algorithms which optimally blend fuel and battery energy in a manner that minimizes the total Ah-processed through each cell.

Table 2.2 Cycling conditions for experimental studies on C-LiFePO$_4$ cells relating Ah-processed and capacity fade.
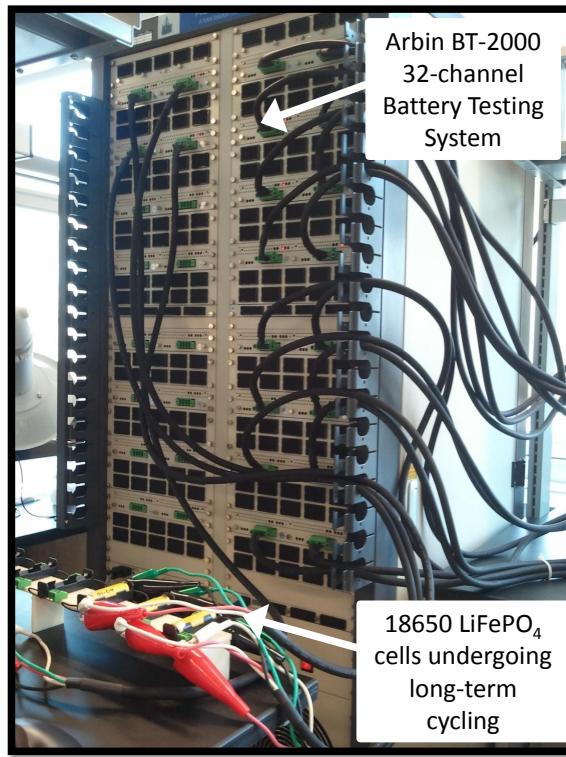
Reference	C-rate	Depth of discharge	Temperature
Peterson *et al.* [108]	Scaled PHEV drive cycle loads with C-rates ranging from -3C to +1C	34% to 97%	Ambient room temp. (24-27°C)
Wang *et al.* [109]	Constant current at C/2	10% to 90%	60° C

Future Work: Data-driven Health Models

Efforts to obtain data-driven models of battery health degradation are currently underway. These efforts consist of cycling multiple cells at various rates, depth of discharge levels, and temperatures using the experimental equipment shown in Fig. 2.7 and 2.8. These tests have been carefully designed using theory on experimental design and Fisher information [110, 10]. Future work shall utilize the methods proposed throughout this dissertation on these models.

2.1.4 Battery Pack Model
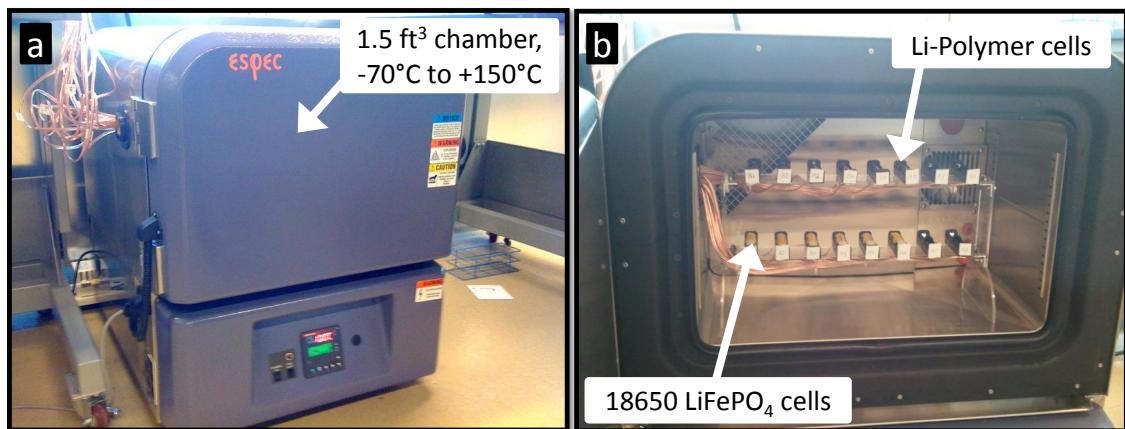
Switched capacitor circuits [111, 112] are typically applied to equalize individual SOC levels for cells connected in series. In this article, we examine the potential advantages of allowing unequal charge levels for battery modules connected in parallel. A simple method to independently control module charge levels uses switches in protection circuits [113] (e.g. solid state relays or contactors). These devices are primarily designed to disconnect the battery in case of imminent catastrophic behavior, such as thermal runaway [114]. When multiple modules are arranged in parallel, individual solid state relays can be connected in series with each parallel branch. These relays may serve as one potential opportunity for individually controlling battery module SOC, and will be the topology we consider henceforth.
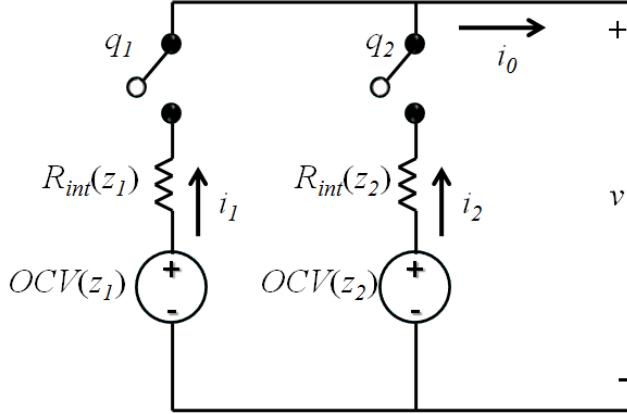
Figure 2.7 Arbin BT2000 32-channel battery test system used for data-driven health degradation modeling.

Two-Module Pack

Consider a battery pack architecture consisting of two modules connected in parallel through two switches, where each module contains one cell for simplicity (Fig. 2.9).

Figure 2.8 (a) Espec 1.5 cu ft. thermal chamber used for data-driven health degradation modeling. (b) LiFePO$_4$ and Li-Polymer cells undergoing temperature controlled cycling.

Figure 2.9 Circuit diagram of battery pack.

The goal is to determine the optimal switching strategy that minimizes the total film growth of both cells, given an exogenous current trajectory i_0. Due to the computational complexity of the distributed parameter electrochemical cell model described in Section 2.1, and the curse of dimensionality imposed by dynamic programming [115], we require a simplified model for control design. As such, we utilize an equivalent circuit model [62, 55], written in discrete time, with a ten second time step ($\Delta T = 10$ sec). This equivalent circuit model consists of an open circuit voltage source OCV in series with an internal resistor R_{int}. Open circuit voltage and internal resistance are nonlinear functions of SOC, that is $OCV(z_i)$ and $R_{int}(z_i)$ where $i = 1, 2$. The state variables z_1 and z_2 represent the SOC of battery cells 1 and 2 respectively. The dynamic equations for each cell are based on integrating current i_1, i_2 to obtain charge, and then dividing by the total charge capacity of the cell Q.

$$z_{1,k+1} = z_{1,k} - \frac{i_{1,k}}{Q}\Delta T \tag{2.29}$$

$$z_{2,k+1} = z_{2,k} - \frac{i_{2,k}}{Q}\Delta T \tag{2.30}$$

The currents i_1, i_2 are determined by the configuration of the switches and exogenous current demand on the battery pack i_0. The currents are given by Kirchoff's current law, where the switching signals q_1 and q_2 equal zero and one when the corresponding

switch is respectively open or closed:

$$i_{1,k} = q_{1,k}(1 - q_{2,k})i_{0,k} \qquad (2.31)$$
$$+ \frac{OCV(z_{1,k}) - OCV(z_{2,k}) + i_{0,k}R_{int}(z_{2,k})}{R_{int}(z_{1,k}) + R_{int}(z_{2,k})}q_{1,k}q_{2,k}$$
$$i_{2,k} = (1 - q_{1,k})q_{2,k}i_{0,k} \qquad (2.32)$$
$$+ \frac{OCV(z_{2,k}) - OCV(z_{1,k}) + i_{0,k}R_{int}(z_{1,k})}{R_{int}(z_{1,k}) + R_{int}(z_{2,k})}q_{1,k}q_{2,k}$$
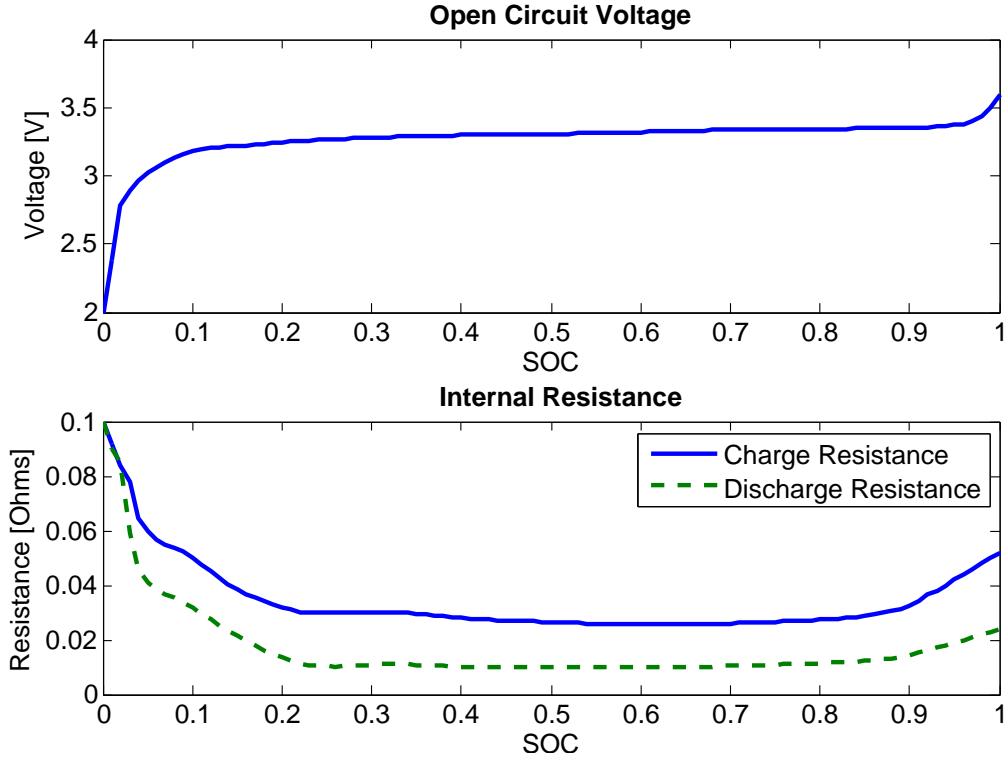
The first terms on the right-hand sides of (2.31) and (2.32) model one cell connected at a time. The second terms model when both cells are connected. When both q_1 and q_2 equal zero neither cell charges (i.e. both cells experience zero current).

Parameterization

The parameters OCV and R_{int} for the equivalent circuit model are identified from experimental characterization of commercial lithium-ion cells with LiFePO$_4$ cathode chemistries. The measured values are provided in Fig. 2.10. The open circuit voltage is determined by charging and discharging the cells at a C/10 rate across the entire voltage range. Then we average the measured terminal voltage for each SOC value. Internal resistance is determined by applying step changes in current and measuring the associated jump in terminal voltage, for each SOC value. This is done for both charging and discharging, rendering internal resistance as a function of SOC and direction of current flow.

2.2 PHEV Powertrain
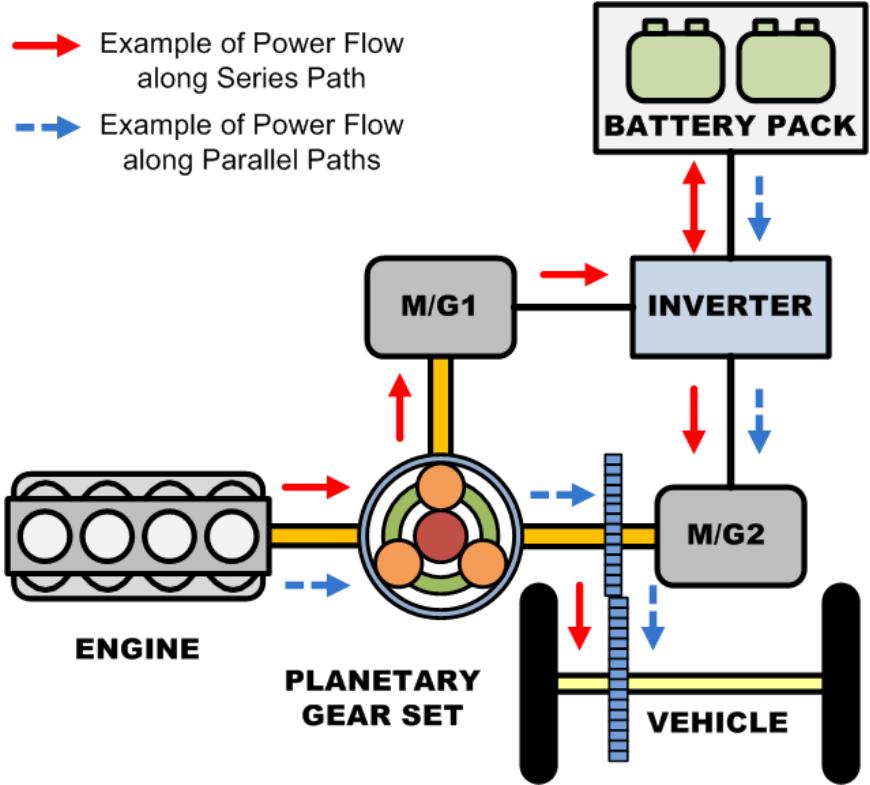
The PHEV modeled in this dissertation has a power-split configuration based upon THS-II [5], with a lithium-ion battery pack enlarged to a 5kWh energy capacity for plug-in operation [116]. Figure 2.11 portrays the main components and configuration of the power-split configuration (also known as "series/parallel" or "combined". This architecture combines internal combustion engine power with power from two electric motor/generators (identified as M/G1 and M/G2) through a planetary gear set. The planetary gear set creates both series and parallel paths for power flow to the wheels. The parallel flow paths (dashed blue arrows) include a path from the engine to the wheels and a path from the battery, through the motors, to the wheels. The series flow

Figure 2.10 Parameterization of equivalent circuit battery model identified from commercial lithium-ion cells with LiFePO$_4$ cathode chemistries. [Top] Open circuit voltage and [Bottom] internal resistance.

path, on the other hand, takes power from the engine to the battery first, then back through the electrical system to the wheels (solid red arrows). This redundancy of power flow paths, together with battery storage capacity, increases the degree to which one can optimize powertrain control for performance and efficiency while meeting overall vehicle power demand.

General parameters for the vehicle are provided in Table 2.3. A schematic of the PHEV system, the supervisory controller, and the relevant signals are given in Fig. 2.12. The state variables include engine speed, vehicle speed, battery state-of-charge (SOC) and acceleration. Acceleration is governed by a Markov chain which captures drive cycle dynamics, described in Section 2.3. We design this Markov chain to explicitly account for real-world daily trip length distributions - which is relevant for PHEVs that will potentially recharge overnight. In addition, we also include a battery health degradation model based upon an electrochemical anode-side film formation mechanism. To provide some perspective on the computational complexity for SDP-based control studies, Table 2.4 summarizes the number of states and controls

Figure 2.11 The single mode power-split hybrid architecture uses a planetary gear set to split power amongst the engine, M/G1, and M/G2. Diagram adapted from [5].
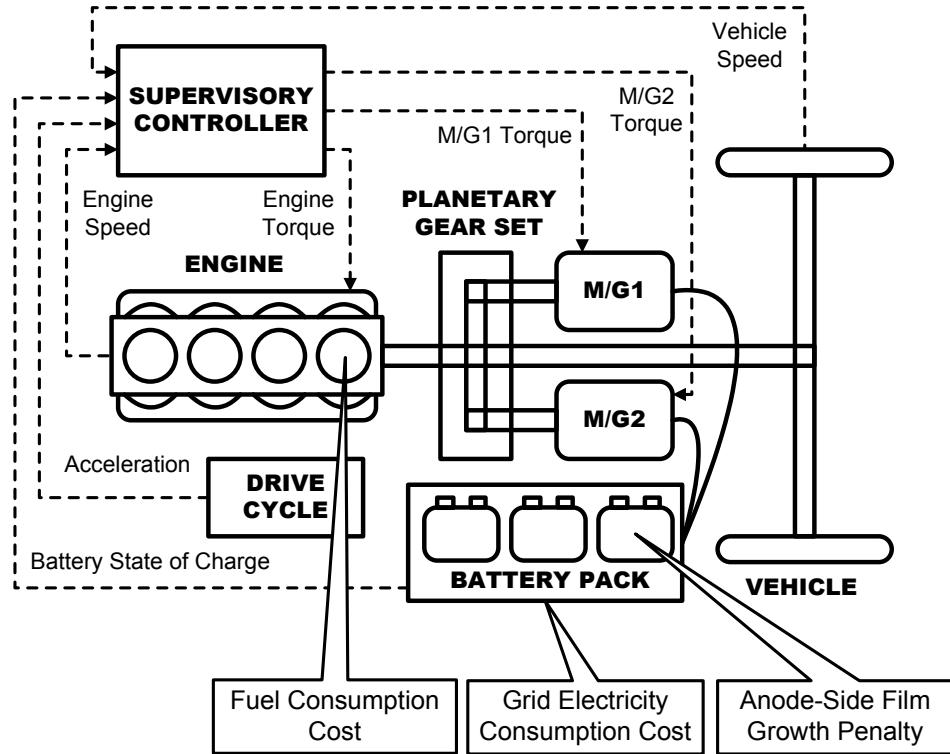
for various hybrid configurations studied in the past decade. A power-split architecture, with four states and two controls, is one of the more complex systems to study. In the following subsections we summarize the dynamic phenomena and governing equations for these models. Please reference the Appendix C for nomenclature definitions.

2.2.1 Mechanical Subsystem

The planetary gearset is at the heart of the power-split configuration. This three-port device couples the engine, motor/generator 1 (M/G1), and motor/generator 2 (M/G2) crankshafts. The planetary gear set can be conceptually and mathematically treated as an ideal "lever" connecting the engine, two motor/generators, and vehicle wheels (through the final drive), as shown in Fig. 2.13. The dynamic-algebraic equations that describe this device are governed by Euler's law and a kinematic constraint relating

34

Table 2.3   General PHEV Model Parameters

Vehicle	EPA Classification	Midsize Sedan
	HEV Configuration	Power-split
	Base Curb Weight	1471 kg
Engine	Type	Gasoline Inline 4-cylinder
	Displacement	1.5 L
	Max Power	57 kW @ 4500 RPM
	Max Torque	110 N-m @ 4500 RPM
Motor/ Generators	Type	Permanent Magnet AC
	M/G1 Max Power	30 kW @ 3000-5500 RPM
	M/G2 Max Power	35 kW @ 1040-5600 RPM
Battery Pack	Cell Chemistry	C-LiFePO$_4$
	Energy Capacity	5 kWh for pack
	Charge Capacity	2.3 Ah per cell
	Number of Cells	660
	Cell Arrangement	110S6P

Figure 2.12   PHEV powertrain system model. The supervisory controller provides the optimal engine, M/G1, M/G2, and M/G2 torque inputs as a function of the PHEV states to minimize energy consumption and battery film growth.

Table 2.4 Previous SDP-Based Hybrid Vehicle Control Problem Formulations

Configuration	Reference	States	Controls
Parallel HEV	Lin/2004 [37]	v, SOC, P_{dem}	P_e
Parallel Fuel Cell	Lin/2004 [37]	v, SOC, P_{dem}	I_{fc}
Parallel HEV	Johannesson/2007 [40]	v, SOC, P_{dem}	P_e
Power Split HEV	Liu/2007 [73]	$\omega_e, v, SOC, P_{dem}$	$P_e, T_{M/G1}$
Parallel HEV	Tate/2007 [41]	v, SOC, P_{dem}	PSR
Dual Mode HEV	Tate/2007 [41]	$\omega_e, v, SOC, a, T_{cat}$	$\omega_e, P_{batt}, M_e, M_{trm}$
Series-Parallel HEV	Opila/2010 [48]	$v, SOC, a,$ $CurrentGear,$ $EngState$	$T_e, TransGear,$ $T_{EM1} \text{or} \omega_{EM1}$
Series Hydraulic Hybrid	Johri/2010 [117]	v, SOC, P_{dem}	T_e, ω_e
Power Split PHEV	Moura/2011	ω_e, v, SOC, a	$T_e, T_{M/G1}$

component speeds [73]:

$$
\begin{bmatrix} I_e & 0 & 0 & R+S \\ 0 & I_{M/G1} & 0 & -S \\ 0 & 0 & I'_{M/G2} & -R \\ R+S & -S & -R & 0 \end{bmatrix} \begin{bmatrix} \dot{\omega}_e \\ \dot{\omega}_{M/G1} \\ \dot{\omega}_{M/G2} \\ F_g \end{bmatrix} = \begin{bmatrix} T_e \\ T_{M/G1} \\ T'_{M/G2} \\ 0 \end{bmatrix} \tag{2.33}
$$

The terms $I'_{M/G2}$ and $T'_{M/G2}$ are effective inertia and torques

$$
\begin{align}
I'_{M/G2} &= I_{M/G2} + (I_w + mR^2_{tire})/K^2 \tag{2.34} \\
T'_{M/G2} &= T_{M/G2} + F_{road}R_{tire}/K \tag{2.35} \\
F_{road} &= 0.5\rho C_d A_{fr} v^2 + \mu_{roll} mg \tag{2.36}
\end{align}
$$
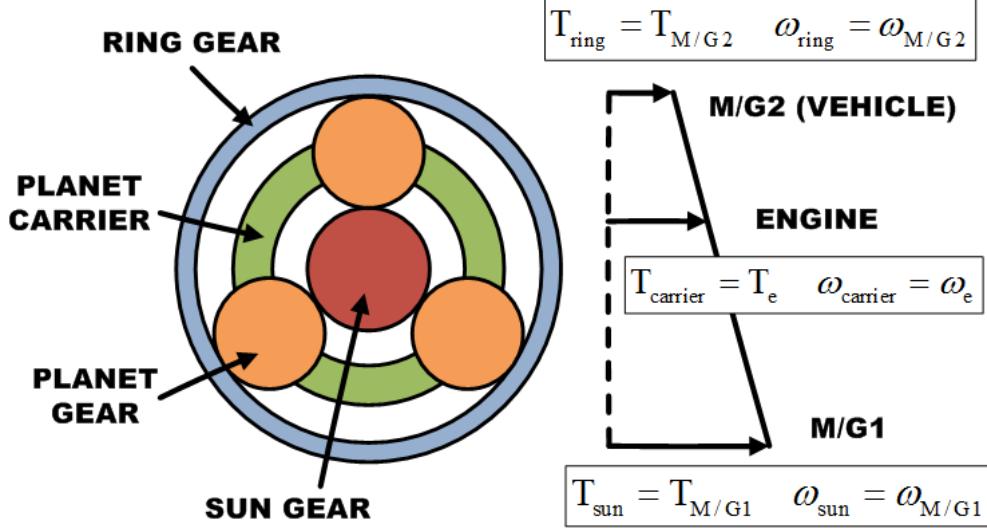
where F_{road} includes viscous aerodynamic drag and rolling friction forces.

Liu [73] demonstrated that the differential-algebraic equations which govern all possible power-split designs satisfy a universal matrix format give by

$$
\begin{bmatrix} J & D \\ D^T & 0 \end{bmatrix} \begin{bmatrix} \dot{\Omega} \\ F \end{bmatrix} = \begin{bmatrix} T \\ 0 \end{bmatrix} \tag{2.37}
$$

where J is a diagonal matrix containing inertia of each component attached to the planetary gear set and D contains kinematic parameters associated with the coupling
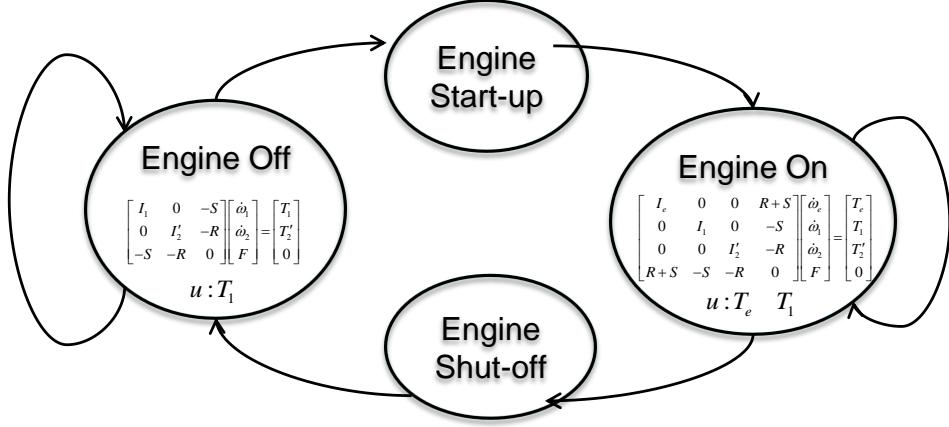
Figure 2.13 Planetary gear set and lever diagram. The engine, M/G1, and M/G2 are attached to the planet carrier, sun, and ring gears, respectively.

between gears. This format has the special property that one may analytically solve for the state variables $\dot{\Omega}$ without explicitly determining the gear force F or inverting the matrix on the LHS of (2.33). The resulting matrix ordinary differential equation is:

$$\dot{\Omega} = J^{-0.5} \left[I - E(E^T E)^{-1} E^T \right] J^{-0.5} T \tag{2.38}$$

This process results in two degrees of freedom, since originally there exist three ordinary differential equations and one algebraic constraint.

The control inputs include engine torque T_e and M/G1 torque $T_{M/G1}$. The engine is allowed to shut off by considering an "engine off" torque input command, which causes the engine speed to drop to zero within the span of one supervisory control time step (one second in this case). When positive torque is commanded from the engine while it is in the shutoff state, the engine is brought back to idle speed within one supervisory control time step. During both engine-on and engine-off modes, and transitions in between, the equations in (2.33)-(2.36) must be respected. For example, $\dot{\omega}_e = 0$ when the engine remains off. When the engine is commanded to turn on, then $\dot{\omega}_e$ must equal the appropriate value such that it reaches idle speed in the next simulation time step. If the engine speed must be above idle to meet the motor/generator speed constraints, then $\dot{\omega}_e$ must correspond to this speed change. The same type of calculations are used for engine shut-down. M/G2 torque $T_{M/G2}$ is determined by the states and control inputs since $\dot{\omega}_{M/G2}$ is proportional to the acceleration state a according to $\dot{\omega}_{M/G2} = aK/R_{tire}$. This concept is illustrated by the hybrid state automata depicted

Figure 2.14 Hybrid state automata used for engine shut-off and start-up transition.
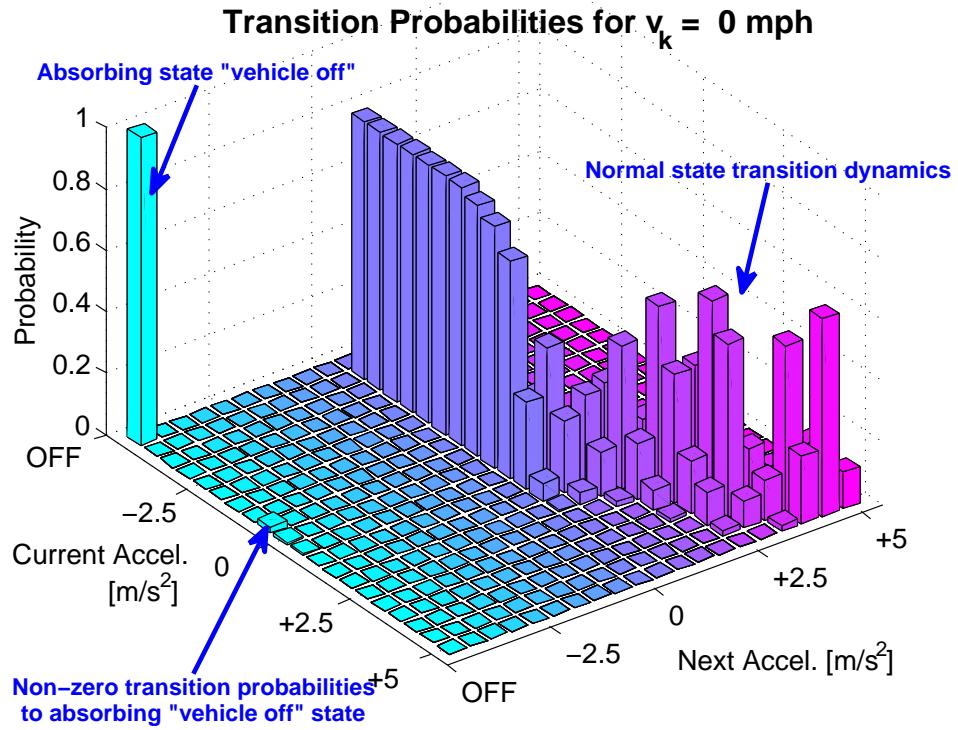
if Fig. 2.14.

2.2.2 Electrical Subsystem
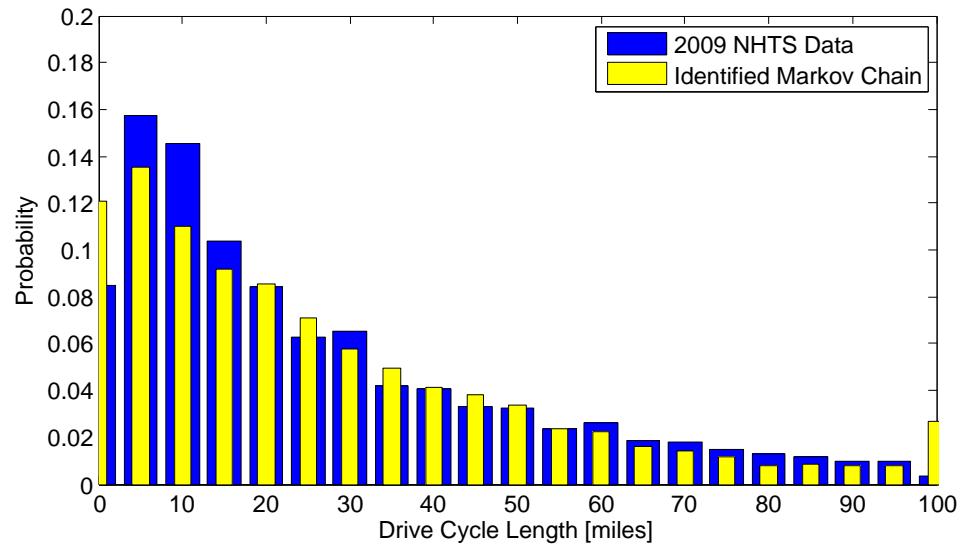
Both M/G1 and M/G2 interface with the battery pack, as shown in Fig. 2.12. These devices are modeled by power efficiency maps supplied by the Powertrain System Analysis Toolkit (PSAT) [9]. The motor/generator inertial dynamics are accounted for in (2.33), while their significantly faster inductive dynamics are approximated as instantaneous. The electrical powertrain also consists of power electronics. However, their dynamics are also ignored since they exceed the 1Hz bandwidth typically considered in power management studies. Nonetheless, their power transfer losses are accounted for in the motor/generator power efficiency maps, provided in Appendix D. Hence, the governing equations for the electric subsystem are given by:

$$P_{batt} = T_{M/G1}\omega_{M/G1}\eta_{M/G1}^{k_{M/G1}} + T_{M/G2}\omega_{M/G2}\eta_{M/G2}^{k_{M/G2}} \tag{2.39}$$

$$k_i = \begin{cases} -1, & T_i\omega_i > 0 \\ 1, & T_i\omega_i \le 0 \end{cases} \quad \text{for} \quad i = \{M/G1, M/G2\}$$

$$\tag{2.40}$$

Figure 2.15 Transition probabilities of the Markov chain for zero vehicle speed, which demonstrate the transition dynamics to the absorbing "vehicle off" state. The value of these transition probabilities relate to the distribution of daily trip length.

Figure 2.16 Trip length distribution for 2009 NHTS data and the identified Markov chain.

2.3 Drive Cycle Models

An important new contribution we apply toward *plug-in* HEV power management is to model drive cycles with a first-order Markov chain *containing a terminal state.* Namely, the terminal state can represent "vehicle off" which signifies when the drive cycle terminates and no more cost accrues. The concept of a terminal state in Markov chain models of drive cycles is not new and has been applied in the context of HEVs [41]. However, it has critical importance for *plug-in* HEV power management. Namely, a terminal state allows us to model distributions of drive cycle length directly. As demonstrated by O'Keefe and Markel [38], drive cycle length is critically important for *plug-in* HEV power management. They demonstrate that the optimal strategy rations battery charge through blending engine and battery power such that SOC reaches the minimum level exactly when the trip terminates, if the drive cycle is known *a priori.* This is in contrast to HEV power management, where battery SOC is typically sustained around a fixed value. In a later study Larsson, Johannesson, and Egardt studied the sensitivity of energy consumption to uncertainties in trip length [118]. Specifically, they formulated dynamic programming problems in which trip length was modeled by a Gaussian distribution. They discovered notable savings in fuel costs even with relatively little knowledge of trip length. We extend this work by directly incorporating daily trip length distribution information using this terminal state. This modeling approach is not new, and has been applied in the context of HEV power management [54]. Yet, its utility is particularly well suited for plug-in applications.

Mathematically, the Markov chain is given by

$$p_{ijm} = \Pr(a_{k+1} = j | a_k = i, v_k = m) \tag{2.41}$$

$$p_{itm} = \Pr(a_{k+1} = t | a_k = i, v_k = 0) \tag{2.42}$$

$$1 = \Pr(a_{k+1} = t | a_k = t, v_k = 0) \tag{2.43}$$

which maps acceleration-velocity pairs to a probability distribution over acceleration in the next time step (2.41)-(2.42). These transition probabilities are identified from certification cycles and real-world micro-trip data [42]. We derived the transition probabilities in 2.41 from this data using maximum likelihood estimation [119]. The Markov chain model assumes that the current state is conditioned only on the state immediately preceding it. We validated this assumption by computing the model residuals and confirming that their autocorrelation exceeds the 95 percent confidence interval for no more than 5 percent of all lag values that are 25% of the length of the

data set or less - as is the case for a white noise process [120].

Figure 2.15 visually demonstrates the transition probabilities at zero vehicle speed where there exists non-zero transition probabilities to the absorbing state for certain velocity-acceleration pairs. When acceleration reaches the terminal state t, it remains in that state with probability one (2.43) and no further cost is incurred. In other words, the vehicle is off and the trip is over.
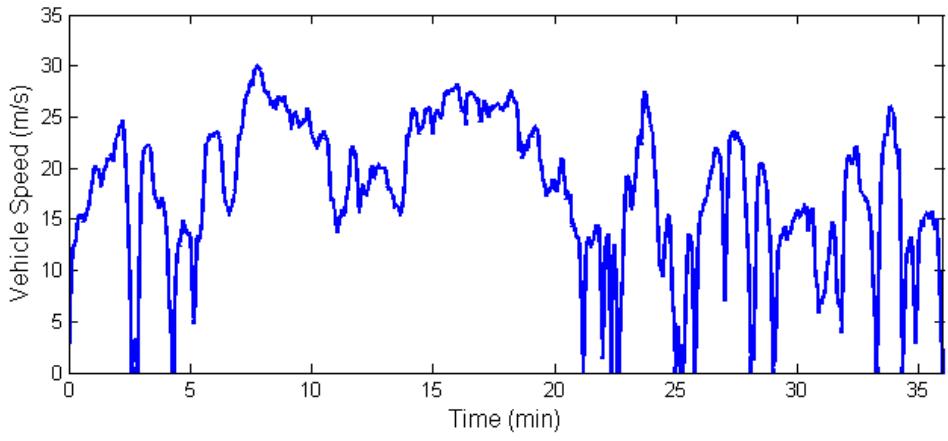
Figure 2.16 demonstrates the distribution of trip length for the Markov chain, in which the transition probabilities p_{itm} in (2.42) have been identified from the 2009 National Household Travel Survey (NHTS) database [121]. Specifically, the probability of transition to "vehicle off" is zero unless the vehicle is completely stopped ($v_k = 0$) and has zero or small negative acceleration. Without adding distance as a state variable, it is difficult to perfectly match the Markov chain and NHTS data. Nevertheless this approach integrates a reasonably accurate representation of real-world trip lengths without adding an exponential increase in computational complexity - a key benefit.

In the results presented in Chapter 3 we evaluate each controller across a library of 1,000 drive cycles generated from the Markov chain. An example randomly generated drive cycle is shown in Fig. 2.17. This process enables us to quantify the performance metrics across a distribution of drive cycle characteristics, rather than single certification cycles such as UDDS.
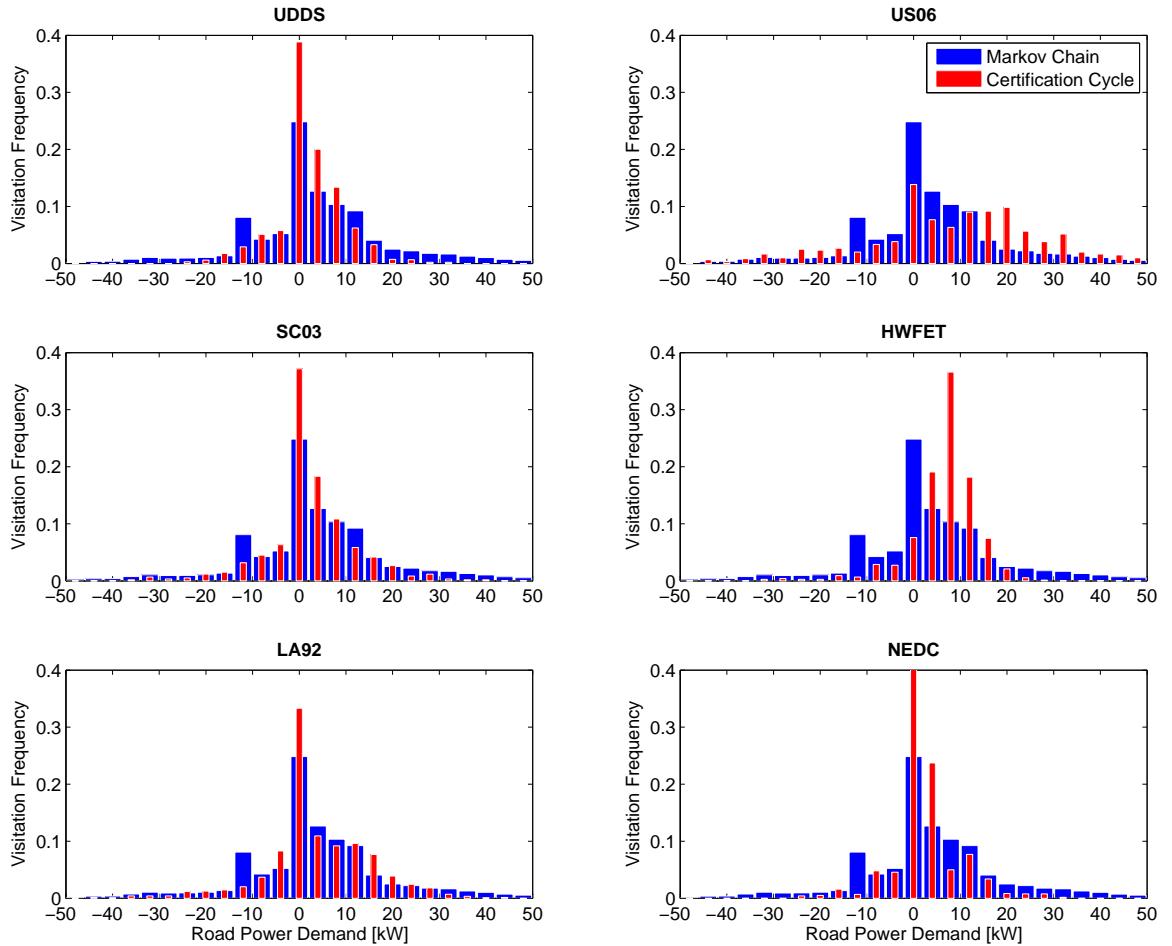
To provide more insight on the characteristics of the Markov chain model vis-a-vis government certification cycles, Fig. 2.18 portrays the distributions of road power demand for various cycles. The road power demand is calculated from the following equation

$$P_{dem} = mav + \frac{1}{2}A_{fr}C_d v^3 + \mu mgv \qquad (2.44)$$

which includes acceleration/deceleration, viscous air drag, and power loss due to rolling resistance. The parameters correspond to the PHEV model described in Section 2.2. Figure 2.18 superimposes various certification cycles over the Markov chain model. One can see how the Markov chain is generally more aggressive (i.e. higher power demand magnitudes) than UDDS, yet less aggressive than US06. In HWFET, which consists of mostly sustained high speeds experienced in highway driving, the distribution mean is shifted toward positive power. The New European Drive Cycle (NEDC) is relatively mild and experiences a large amount of stops (0 kW). These certification cycles, along with the Markov chain, will be used to evaluate various PHEV power management control designs in Chapter 3.

Figure 2.17 A sample randomly generated drive cycle from the Markov chain model.

Figure 2.18 Distributions of road power demand for various certification cycles superimposed on the distribution of road power demand for the Markov chain model.

2.4 Summary

This chapter utilizes first-principle physics to develop dynamic system models of the components considered throughout this dissertation. These components include Li-ion batteries, PHEV powertrains, and stochastic drive cycle dynamics and length. In the discourse on Li-ion batteries, we provide an overview of battery fundamentals, important degradation mechanisms, and the electrochemical transport, diffusion, intercalation, and electric dynamics. A custom-built battery-in-the-loop test system is also fabricated to identify the electrochemical model. The dynamics for each cell can be combined into battery packs, which are subsystems of the PHEV drive train. We specifically focus on a power-split architecture, yet other architectures can be considered as well. Finally, we describe a Markov chain modeling approach to predict drive cycle behavior in a statistical sense [37]. A new contribution to drive cycle modeling is the direct encoding of daily trip length through the utilization and proper identification of a terminal state (i.e. "vehicle off") within the Markov chain. These models will be utilized in the subsequent chapters to design battery-health conscious power management algorithms.

Chapter 3

Stochastic Control for Health-Conscious PHEV Power Management

This chapter investigates battery health conscious power management in plug-in hybrid electric vehicles through a novel combination of electrochemical modeling and stochastic control. This framework is a critical step toward increased performance and longevity of battery-powered systems. The controllers are designing to minimize both energy consumption (fuel and grid-supplied electricity) and battery health degradation metrics (SEI layer or Ah-processed). Several recent studies have considered the HEV power management problem for extending battery life. These studies focus on depth of discharge control [122, 123], power electronics management[124], and temperature management [125]. To date, however, no studies have applied models that explicitly account for specific electrochemical degradation mechanisms in the context of an optimal control framework, to the author's knowledge.

As a foundation, we first consider optimal blending without battery health. Then we analyze the sensitivity of these algorithms to battery size. Next we include electrochemistry-based degradation mechanisms and analyze the tradeoff between reducing energy consumption and reducing battery damage. Analysis of the optimal solutions reveal which physical properties (i.e. slope properties of the degradation model) enable increased performance and longevity through control. The design and analysis framework begins with a formulation of the general stochastic optimal control problem.

3.1 Optimal Control Problem Formulation

The control objective is to synthesize a static function mapping the PHEV state variables to the engine and M/G1 torque inputs such that both energy consumption cost (i.e. fuel and grid electricity) and battery health degradation in terms of anode-side film growth are minimized. We formulate this as a shortest-path[1] stochastic dynamic programming problem.

$$\text{min:} \qquad J^g \;=\; \lim_{N\to\infty} \mathrm{E}\left[\sum_{k=0}^{N} c(x_k, u_k)\right] \qquad\qquad (3.1)$$

$$\text{subject to:} \qquad x_{k+1} \;=\; f(x_k, u_k, w_k) \qquad\qquad\qquad (3.2)$$

$$x \;\in\; X \qquad\qquad\qquad\qquad (3.3)$$

$$u \;\in\; U(x) \qquad\qquad\qquad\qquad (3.4)$$

where J^g is the cost for a given control policy g and $c(x_k, u_k)$ is a function that maps the state and control vectors to an instantaneous cost. Note that 3.1 is formulated as an infinite-horizon problem, which brings forth the question of whether J^g is finite. Indeed, J^g is guaranteed to be finite since the system enters the terminal state (i.e. "vehicle off") in finite time with probability one and incurs zero addition cost henceforth. As such, the cost function J^g is guaranteed to be finite. The system dynamics summarized in discrete-time by (3.2) are provided in Chapter 2, with a one-second time step. This optimization is subject to sets of state and control constraints, X and $U(x)$ respectively, described in detail in Section 3.1.2. Our objective is to solve for the optimal control policy g^* which satisfies.

$$g^* = \arg\min_{g\in\mathcal{G}} J^g \qquad\qquad\qquad (3.5)$$

where $\mathcal{G}$ denotes the set of all feasible control policies.

3.1.1 Objective Function

The minimization of both energy consumption cost and battery health is, generally speaking, a multi-objective optimal control problem. For simplicity, we combine both

---

[1]The shortest-path term [126] is used for Markov decision processes that contain a terminal state in the Markov chain, such as our drive cycle model.

objectives into a scalar objective with linear weighting α, given mathematically by

$$c(x_k, u_k) = \alpha \cdot c_E(x_k, u_k) + (1 - \alpha) \cdot c_H(x_k, u_k) + c_{SOC}(x_k, u_k) \quad (3.6)$$

where the individual objective functions are given by

$$c_E(x_k, u_k) = \beta \alpha_{fuel} W_{fuel} + \alpha_{elec} \frac{-V_{oc} Q_{batt} \dot{SOC}}{\eta_{grid}} \quad (3.7)$$

$$c_H(x_k, u_k) = \dot{\delta}_{film}(I, SOC) \quad \text{OR} \quad |I/I_{max}| \quad (3.8)$$

$$c_{SOC}(x_k, u_k) = \begin{cases} \alpha_{SOC} \frac{SOC_{\text{min}} - SOC}{SOC_{\text{max}} - SOC_{\text{min}}} & \text{if } SOC \leq SOC_{\text{min}} \\ 0 & \text{else} \end{cases} \quad (3.9)$$

Equation (3.7) represents the instantaneous energy consumption cost in USD, which includes both fuel and grid charging costs. The first term of (3.7) quantifies PHEV fuel consumption, while the second term quantifies electricity consumption, and the coefficient β makes it possible to carefully study tradeoffs between the two. Specifically, W_{fuel} represents the fuel consumption rate in grams per time step. The constant parameter α_{fuel} then converts this rate to an energy consumption rate, in megajoules (MJ) per time step. Similarly, the second term of (3.7) represents the instantaneous rate of change of the battery's internal energy. The constant parameter α_{elec} converts the electricity consumed to MJ per time step. Dividing this change in stored battery energy by a constant charging efficiency $\eta_{grid} = 0.98$ (which corresponds to a full recharge in six hours) furnishes an estimate of the amount of energy needed from the grid to replenish the battery charge consumed during the trip. Note that the second term is positive when the PHEV uses stored battery energy and negative during regeneration. Hence, there exists a reward for regeneration that offsets the need to consume grid electricity. The magnitude of this reward depends on the parameter β, which represents the relative price of gasoline per MJ to the price of grid electricity per MJ is defined as follows:

$$\beta = \frac{\text{Price of Gasoline per MJ}}{\text{Price of Grid Electricity per MJ}} \quad (3.10)$$

We refer to this parameter as the "energy price ratio," and use it to examine the tradeoffs between fuel consumption and electricity consumption in PHEVs. Throughout this dissertation, we use $\beta = 0.8$, consistent with the average energy prices in June 2010, namely $2.73 USD per gallon of gasoline [127] and $0.094 USD per kWh of electricity [6].

Equation (3.8) represents one of two types of battery health models: the instantaneous anode-side SEI film growth, characterized by the map depicted in Fig. 2.6, or the normalized magnitude of applied current in a single battery cell. In the following subsections we consider PHEV power management controllers which minimize both of these measures of health degradation. In principle, other degradation models may also be input here. Additionally, both objectives are normalized by scaling the range of their physical values to values between zero and one.

Equation (3.9) invokes a linear penalty when the SOC falls below a minimum value. The parameter α_{SOC} is a penalty weight. The inclusion of this term produces the charge sustaining behavior we desire once the minimum SOC value is reached.

We vary the weighting α in (3.6) between zero and one to obtain the convex subset of the Pareto optimal control policies. The complete Pareto optimal set would require multi-objective dynamic programming techniques, such as those developed in [128]. Henceforth, we refer to the convex subset of Pareto optimal solutions as, simply, the Pareto set - although this is admittedly an abuse of terminology.

3.1.2 Constraints

In addition to minimizing the aforementioned objectives, the power management algorithm satisfies constraints on both the states and control actions. These constraints correspond to physical operating limits, zones of safe operation, and actuation limits. Rate of change constraints are not considered here, although they can be easily added in this formulation. The state constraints are given by

$$\omega_{e,min}(T_e) \quad \leq \quad \omega_e \leq \omega_{e,max} \tag{3.11}$$

$$\omega_{M/G1,min} \quad \leq \quad \omega_{M/G1} \leq \omega_{M/G1,max} \tag{3.12}$$

$$\omega_{M/G2,min} \quad \leq \quad \omega_{M/G2} \leq \omega_{M/G2,max} \tag{3.13}$$

$$SOC_{min} \quad \leq \quad SOC \leq SOC_{max} \tag{3.14}$$

Minimum engine speed is equal to idle speed when the engine is on, which is typically enforced for combustion stability, noise, vibration, and harshness. Minimum engine speed is zero otherwise. The minimum M/G1 speed constraint also produces an interesting effect in a power-split configuration. If the engine is off, then $\omega_{M/G1}$ will violate its minimum value if vehicle speed, which is proportional to $\omega_{M/G2}$, is sufficiently high, due to the kinematic relationship in (2.33). Consequently the engine must turn on for vehicle speeds greater than 36 mph, even when sufficient battery charge exists to

run in all-electric mode. This constraint partly motivates the need for a dual-model power-split where all-electric operation is possible at high speeds [73].

The control constraints are given by the following:

$$
\begin{aligned}
T_{e,min} &\leq T_e \leq T_{e,max}(\omega_e) & (3.15) \\
T_{M/G1,min}(\omega_{M/G1}) &\leq T_{M/G1} \leq T_{M/G1,max}(\omega_{M/G1}) & (3.16) \\
T_{M/G2,min}(\omega_{M/G2}) &\leq T_{M/G2} \leq T_{M/G2,max}(\omega_{M/G2}) & (3.17) \\
V_{cell,min} &\leq V_{cell} \leq V_{cell,max} & (3.18) \\
I_{cell,min} &\leq I_{cell} \leq I_{cell,max} & (3.19)
\end{aligned}
$$

The minimum M/G2 torque is determined by two constraints: saturation limits on M/G2 and the maximum battery pack voltage, which can be violated if too much regenerative power is supplied to the battery at, for example, high SOC levels. Hence the minimum M/G2 torque is a function of several states and control inputs $T_{M/G2,min} = T_{M/G2,min}(SOC, \omega_{M/G1}, T_{M/G1}, \omega_{M/G2})$. The residual M/G2 torque after applying these constraints is provided by hydraulic braking.

To enforce both the state and control constraints we apply the following method. For all state and control pairs we simulate the subsequent state using (3.2) and the full electrochemical model. If any constraints are violated then the corresponding control inputs are removed from the set of admissible controls, for the given state. This process generates the set of admissible controls $U(x)$ for each state, which can be computed offline from the stochastic dynamic programming algorithm.

Numerically, the SDP problem is solved via modified policy iteration, where the policy evaluation step is approximated through successive value iterations. This algorithm has the property that convergence to the optimal policy occurs in finite time [126]. More details on the implementation of this algorithm can be found in the next subsection.

Since we solve the stochastic dynamic programming problem for a sweeping range of α, and simulate the resulting controllers across 1,000 cycles each, we leverage parallel computing resources at the University of Michigan Center for Advanced Computing.

3.1.3   Numerical Techniques

This section presents the numerical techniques used to solve the optimal power management problem posed in the previous sections.

The SDP problem, which is framed as an infinite-horizon shortest-path problem, is

solved via modified policy iteration, where the policy evaluation step is approximated through successive value iterations. This algorithm has the property that convergence to the optimal policy occurs in finite time [126]. The approach begins with a uniform discretization of the admissible state and control input sets, X and $U(x)$. This discretization makes the optimal power management problem amenable to computer calculations, but generally produces suboptimal results. For a very thorough study of various discretization techniques, refer to the Ph.D. dissertation of Tate [41]. We use the symbols X and $U(x)$ to refer to both the continuous and discrete-valued state and control input sets for ease of reading. Given the discrete-valued sets, we apply a modified policy iteration algorithm to compute the optimal power management cost function and policy. This algorithm consists of two successive steps, namely, policy evaluation and policy improvement, repeated iteratively until convergence. For each possible PHEV state, the policy iteration step approximates the corresponding "cost-to-go" J, which may be intuitively interpreted as the expected cost function value averaged over a stochastic distribution of drive cycles starting at that state. The policy improvement step then approximates the optimal control policy g^*, corresponding to each possible PHEV state. This process iterates, as shown in Fig. 3.1, until convergence. The following subsections present the policy iteration and policy improvement steps in further detail.

Policy Evaluation

The policy evaluation step computes the cost-to-go for each state vector value, x, given a control policy, g. This computation is performed recursively as shown in (3.20):

$$J_{n+1}(x) = c(x, u) + \mathrm{E}_a \left[J_n(f(x, u)) \right] \tag{3.20}$$

The cost-to-go J is guaranteed to be finite because the system will reach the absorbing state (i.e. vehicle-off) in finite-time with probability one and incur zero cost henceforth. The expectation is taken over vehicle acceleration a, whose dynamics are governed by a Markov chain representing drive cycle behavior (See Section 2.3). The index n in the above *recurrence relation* represents an iteration number, and the recurrence relation is evaluated iteratively for all state vector values in the discretized set of admissible states, X. In general, the cost-to-go values within the expectation operator must be interpolated because $f(x, u)$ will not always generate values in the discrete-valued state set X. The true cost-to-go for a given control policy must satisfy $J_n = J_{n+1}$.

As such, we iterate (3.20) until one of two possible conditions are satisfied: (1) the infinity-norm of the normalized difference between J_n and J_{n+1} fall below a threshold value, or (2) a finite number of iterations are reached. This truncated policy evaluation approach, used in combination with the policy improvement step below, converges to the optimal control policy regardless of the maximum number of iterations. See [129, 130, 131, 126] for the theory underlying this method.

Policy Improvement

Bellman's principle of optimality indicates that the optimal control policy for the stochastic dynamic programming problem in (3.1)-(3.2) is also the control policy that minimizes the cost-to-go function $J(x)$ in (3.20). Thus, to find this control policy u^*, we minimize cost-to-go over all admissible controls for a given state $U(x)$ for each state vector value x, given the cost-to-go function $J(x)$. Mathematically, this minimization is represented by:

$$u^*(x) = \arg \min_{u \in U(x)} \left\{ c(x, u) + \mathrm{E}_a[J(x)] \right\} \tag{3.21}$$

Equation (3.21) imposes the state and control input set constraints from Section 3.1.2 by minimizing over the admissible control set $U(x)$.

After both policy evaluation and policy improvement are completed, the optimal control policy is passed back into the policy evaluation step and the entire procedure is repeated iteratively. The process terminates when the infinity norm of the difference between two consecutive steps is less than 1%, for both the cost and control functions.

Reducing Computational Effort

Dynamic programming is, generally speaking, computational intensive because it suffers from the so-called curse of dimensionality. That is, the complexity of the solution algorithms increase exponentially with each additional dimension added to the control-state space [126]. For the PHEV power management problem considered in this dissertation, there exist four states (ω_e, v, SOC, a) and two control inputs $(T_e, T_{M/G1})$. These six dimensions produce a problem that is more complex than most HEV power management studies. This dissertation does not seek to investigate efficient numerical techniques for SDP. However, we shall highlight basic techniques which are effective in making the relatively complex problem under consideration

computationally tractable.

Vectorization: The most effect method to reduce computational effort, by far, is to vectorize the model equations in (3.2). This allows one to input a vector of control inputs and receive a vector of outputs, as opposed to using a for-loop.
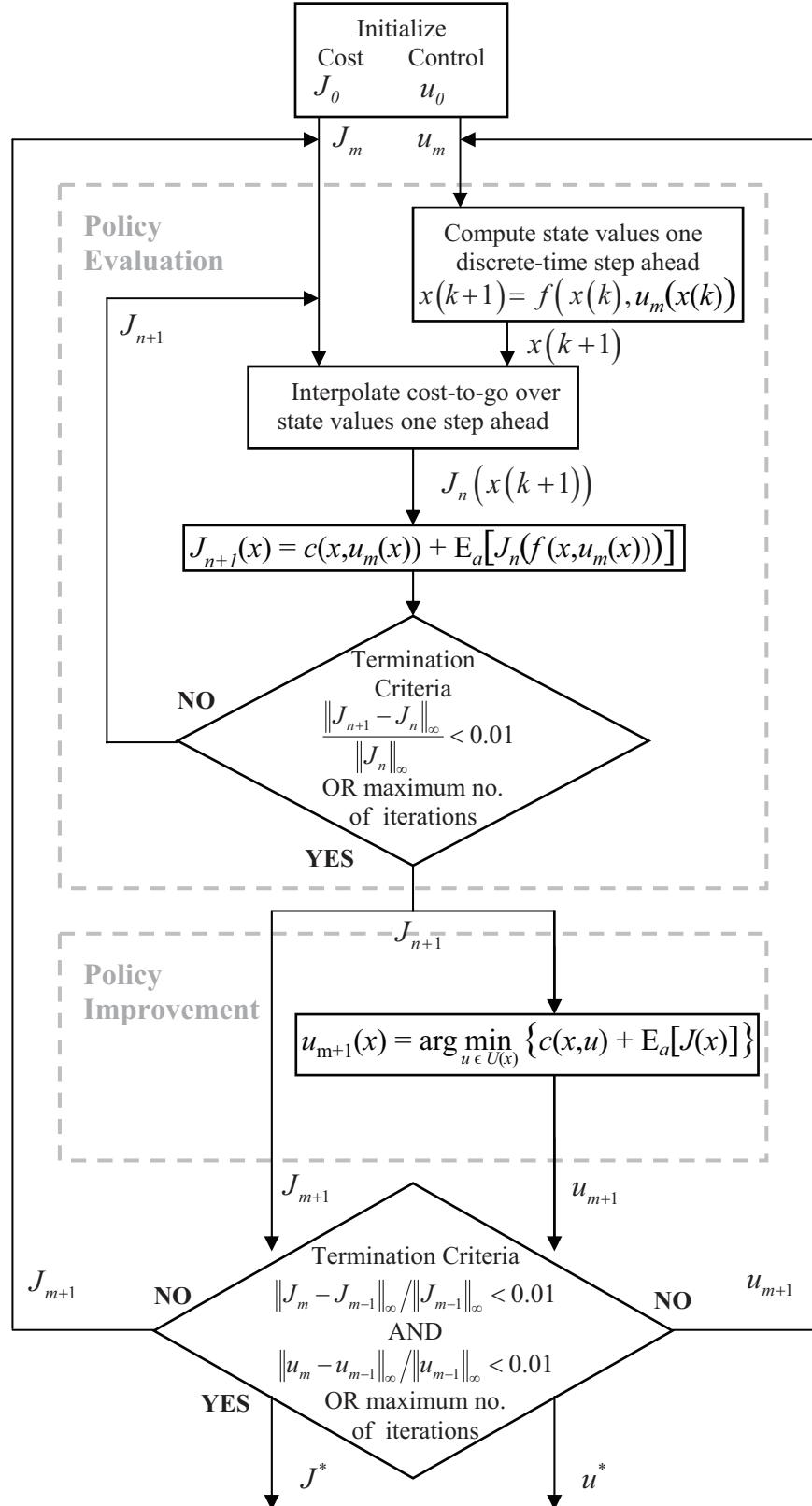
Custom Interpolation Code: The most computationally intensive task of SDP, in this author's experience, is interpolating the cost function over the states calculated for the next time step in (3.20). For this reason we designed stripped-down, singular purpose codes that sacrifice error checking and general purpose features for speed.

Offline Calculations: As an iterative process, SDP repeats several calculations over and over. However, many of these calculations are identical through each iteration and can be performed once offline. Examples include finding admissible control sets, inverting large matrices, preallocating variable space, and discretizing state-control spaces into meshed grids. In the code used to generate all the results shown here, we take advantage of this opportunity whenever possible.

Control Space Reduction: Note that in the policy improvement step (3.21) one must compute the cost of all possible controls to find the minimizer. In this work we calculate the admissible control set $U(x)$ for a given state x offline. That is, for each state we determine the subset of control actions which satisfy all the state and control constraints described in Section 3.1.2. This allows us to perform the minimization in (3.21) over a subset of the complete control space, hence reducing computational complexity. A more detailed description of this process is described in Section 3.4.

Overhead Reduction: Simulink$^©$ is a very popular tool for modeling vehicle systems. However it suffers from overhead calculations that are often unnecessary in the context of SDP. Therefore all models are directly coded in Matlab$^©$ with stochastic dynamic programming applications in mind.

There exist a number of focused studies on the computational aspects of stochastic dynamic programming. These include state-control sampling with Barycentric coordinates [41], linear programming approximations [132], iterative dynamic programming [133, 134, 135, 136], and approximate dynamic programming (ADP) [137, 138, 139], to name a few.

Figure 3.1 Modified policy iteration flowchart. The process consists of two successive steps, policy evaluation and policy improvement, repeated iteratively until a convergence criterion is satisfied.

3.2 Optimal Blending without Battery Health

In this section we first consider optimal PHEV power management results without considering battery health. This analysis is important for contextualizing and interpreting the results when battery health is considered. Mathematically, this problem is formulated by disregarding the battery health term in the objective function (3.6).
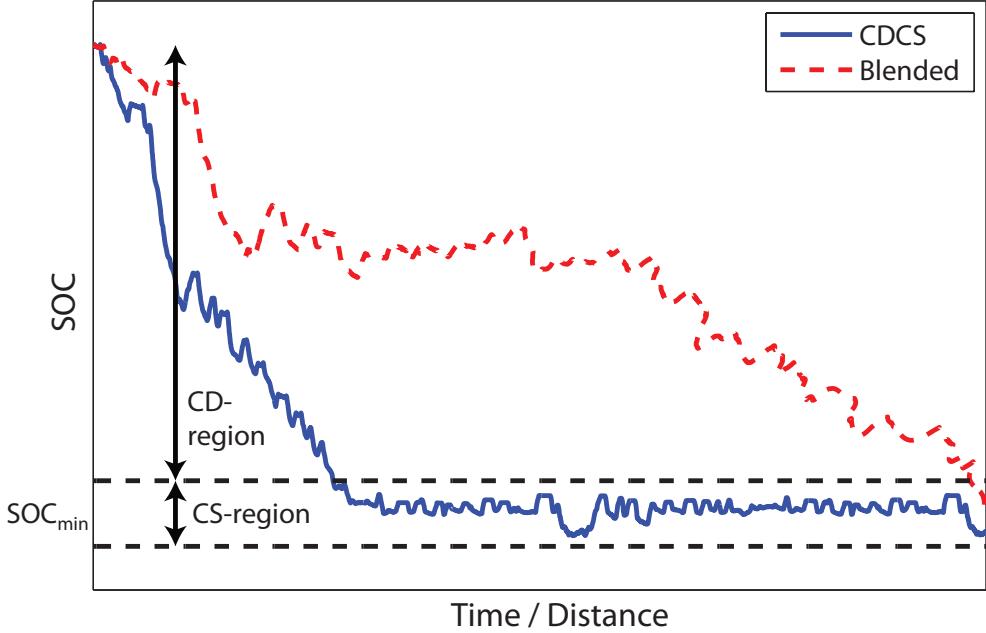
In this section we compare the optimal blending solution resulting from the problem formulated in Section 4.2 to a more conventional strategy. Namely, it is common in PHEV power management research to use control laws that first prioritize battery energy consumption, until they enter a charge sustenance mode like those used by conventional HEVs [140, 141, 142]. We refer to this method as charge depletion, charge sustenance (CDCS). Representative CDCS and blending SOC trajectories are demonstrated in Fig. 3.2. Generally speaking, CDCS seeks to enter the CS-region in minimal time. In contrast, blending attempts to mix engine and battery power such that the SOC reaches the minimum SOC exactly when the trip terminates. CDCS is implemented in the SDP framework here by defining the following cost function.

$$c(x_k, u_k) = \begin{cases} SOC + c_{SOC}(x_k, u_k) & \text{if } SOC \geq 0.3 \\ \alpha_{fuel} W_{fuel} + c_{SOC}(x_k, u_k) & \text{else} \end{cases} \tag{3.22}$$

where c_{SOC} is defined in (3.9). This formulation penalizes SOC in the charge depletion region (see Fig. 3.2), therefore causing the power management algorithm to deplete electricity whenever possible. If the electric machines are capable of meeting the peak power demand of a given drive schedule, this formulation will produce an all-electric range during charge depletion. If the electric machines cannot meet power demand or sufficient SOC does not exist in the battery, then the CDCS algorithm requests engine power to satisfy drive cycle power demand. When the battery reaches the charge sustenance region (i.e. $SOC < 0.3$ in Fig. 3.2), the second case in (3.22) is taken. This cost function forces the power management algorithm to sustain charge in a manner that minimizes fuel consumption. This cost function is extremely common in DP-based HEV power management [37, 38, 73, 41].

3.2.1 Performance

To illustrate the potential performance improvements of a blending strategy over a CDCS strategy, consider their responses for two FTP-72 drive cycles simulated
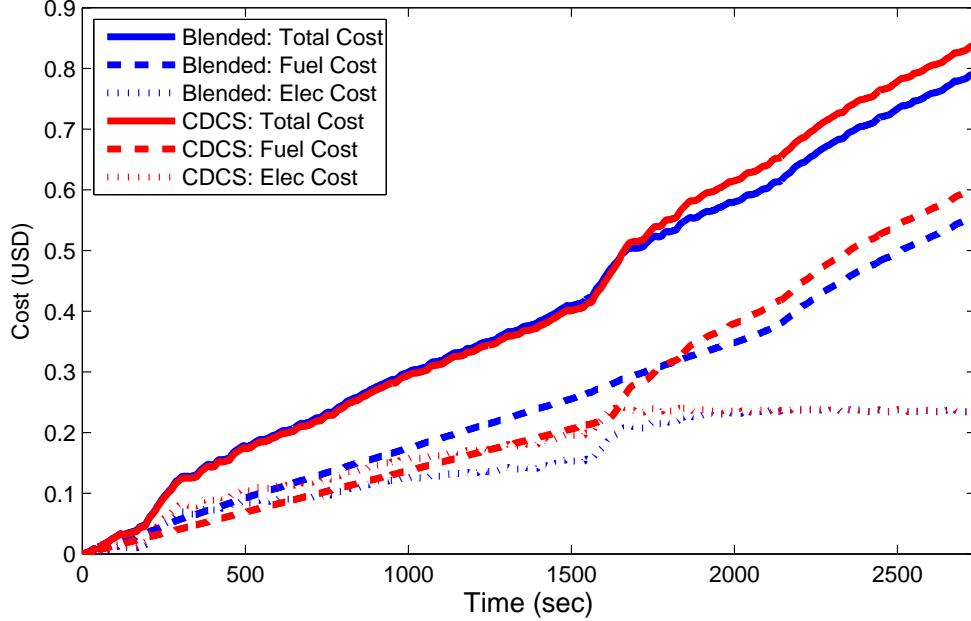
Figure 3.2 Typical SOC trajectories for the charge depletion, charge sustenance (CDCS) and optimal blending strategies.
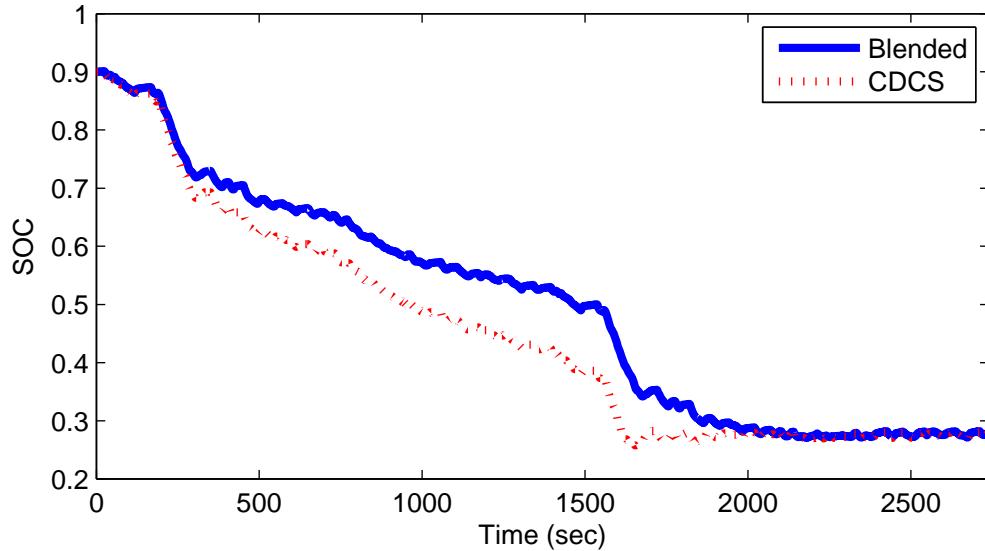
back-to-back, as shown in Fig. 3.3 and 3.4. The total cost of energy for this trip is 6.4% less for the blended strategy relative to CDCS, and fuel consumption is reduced by 8.2%. Blending accomplishes this by utilizing the engine more during the charge depletion phase, thereby assisting the battery to meet total power demand more often than CDCS. Although in the blended case the engine operates at higher loads, therefore consuming more fuel, the engine efficiency is greater and, as demonstrated in Fig. 3.4, battery charge depletes more slowly. As a result, blending and CDCS incur nearly the same total energy costs through the depletion phase (Fig. 3.3), and the advantage of blending in terms of overall cost arises from its delayed entry into charge sustenance.

The benefit of delayed entry into charge sustenance is evident from previous research in the literature in which the PHEV drive cycle and total trip length were assumed to be known *a priori* (e.g., [38], [141]). For example, in [38] deterministic dynamic programming furnished blending strategies that reached minimum SOC exactly when the PHEV trip terminated, thereby never allowing the PHEV to enter the charge sustenance mode. This result agrees with our current findings, namely, that the primary benefit of blending strategies results from their ability to delay or eliminate the need for charge sustenance. However, the approach in [38] requires

knowledge of trip length *a priori*. Since SDP explicitly takes into account a probability distribution of drive cycle behavior, our identified strategy is optimal in the average sense.

Figure 3.3 Running energy consumption costs for blended and CDCS control strategies on two FTP-72 cycles simulated back-to-back. The total cost (solid line) is the sum of fuel (dashed line) and electricity (dotted line) costs.

Figure 3.4 State-of-charge response for blended and CDCS control strategies on two FTP-72 cycles simulated back-to-back.

Performance improvements of blending over CDCS are uniform across all the drive
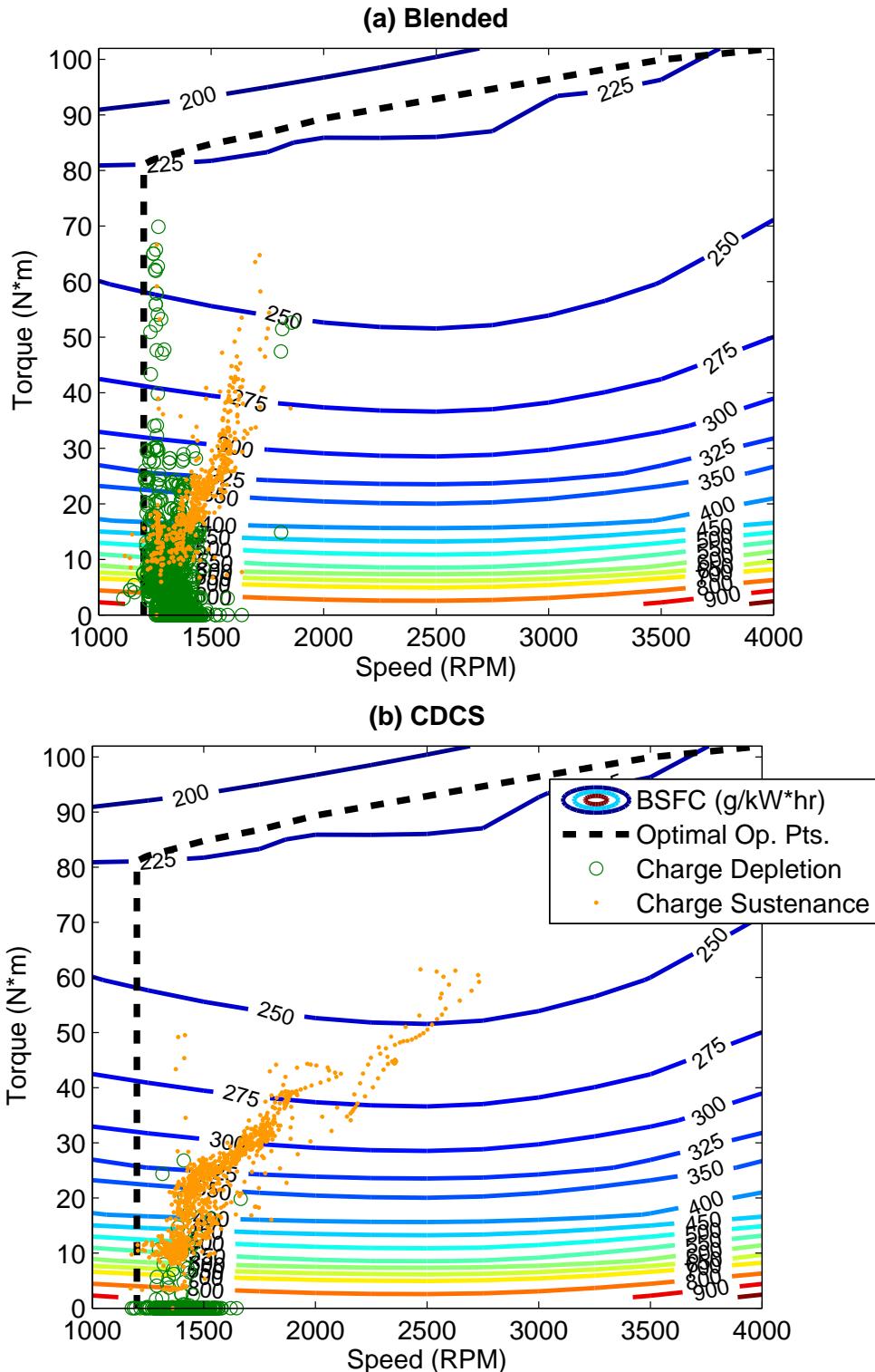
cycles shown in Table II, where the drive cycle lengths are selected to ensure that the vehicle reaches charge sustenance before the trip terminates. If the vehicle reaches its destination before entering charge sustenance phase, however, the total energy consumption costs are nearly identical for blending and CDCS (as demonstrated in Fig. 3.3). Therefore the blending strategy proposed herein has no significant energy consumption cost penalty for early trip termination. Note that some of the largest improvements are observed for drive cycles that were not used to estimate the Markov state transition probability matrix.

3.2.2   Engine Control
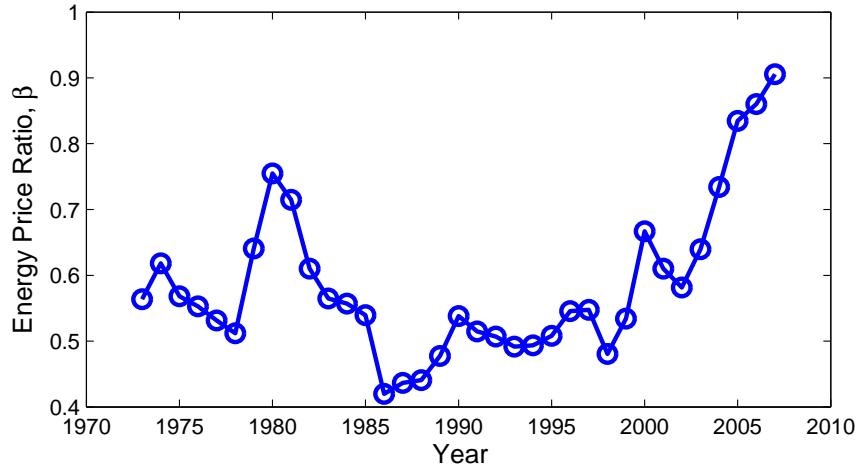
A significant benefit of the power-split architecture is the fact that it decouples the engine crankshaft from the road, and allows the electric machines to move engine speed where fuel efficiency is maximized [5]. This optimal operating line is identified by the black dashed line in Fig. 3.5(a) and 3.5(b). As shown in Fig. 3.5(a), the blending strategy initially operates the engine at fairly low speeds and high torques, close to the optimal fuel efficiency operating line. This occurs even when power demand can be met by the electric motors alone. The excess engine power goes towards regenerating battery charge, which the blended cost function in (3.7) rewards. Moreover, the electric machines are not generally saturated and are thus free to maintain low engine speeds and high efficiencies. In contrast, the CDCS strategy causes the engine to remain at very low brake torque levels during depletion, where fuel consumption is low but so is engine efficiency (Fig. 3.5(b)). Moreover, significant power is requested from the engine only when the electric machines saturate and cannot meet driver power demand by themselves. This limits the control authority of the electric machines when driver power demand is large, thereby reducing their ability to move engine speed to the optimal operating line. These observations explain how the blending strategy utilizes the engine and electric motors more efficiently, thereby delaying the charge sustenance phase and improving overall PHEV operating costs.

3.2.3   Energy Price Ratio
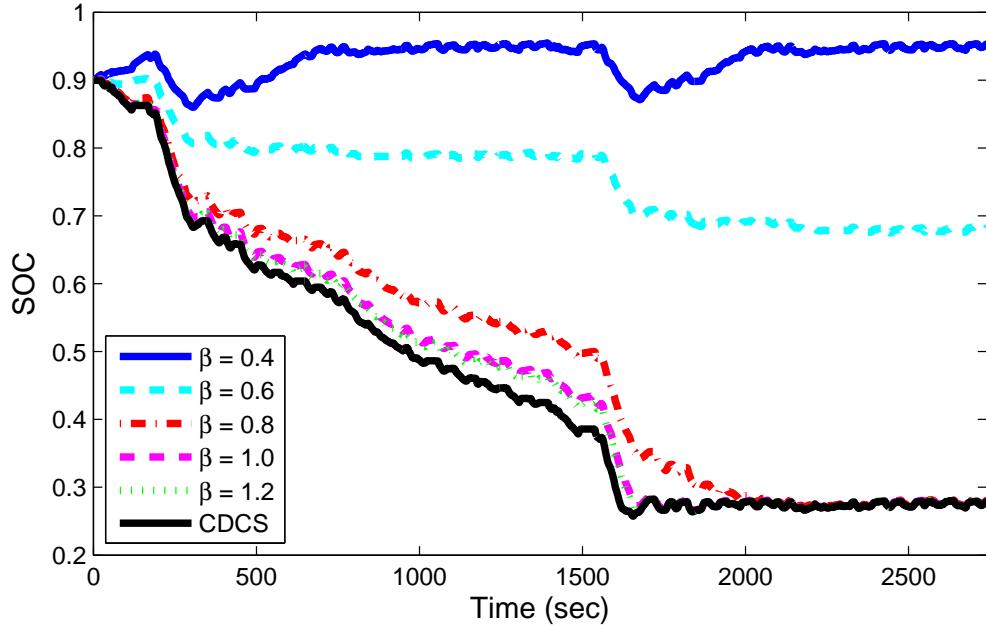
An important feature of the proposed power management algorithm is its dependence on the energy price ratio, β , which varies temporally (e.g., by year) and spatially (e.g., by geographic region). To investigate the nature of this dependence, we obtained the history of energy price ratios since 1973 [6], shown in Fig. 3.6. The value of β

Figure 3.5 Engine operating points for (a) the optimal blended strategy and (b) CDCS strategies on a brake specific fuel consumption map, for two FTP-72 cycles simulated back-to-back.

Figure 3.6 Historic values for the energy price ratio β from 1973 to 2007 [6]. Note how the variation corresponds with shifts in oil and electricity prices.

Figure 3.7 State-of-charge response for varying β (blended) and CDCS control strategies on two FTP-72 cycles simulated back-to-back. Blending approaches CDCS as β approaches infinity.

has clearly changed significantly over the past 35 years due to shifts in both oil and electricity prices. This motivates the need to understand how this parameter impacts optimal PHEV power management.

Consider the SOC depletion responses shown in Fig. 3.7 for controllers synthesized with energy price ratios in the set $\beta \in 0.4, 0.6, 0.8, 1.0, 1.2$ and for a CDCS strategy,

which by definition does not depend on β. Several conclusions can be drawn from this parametric study. First, as β approaches infinity (i.e. fuel becomes infinitely more expensive than grid electric energy), the optimal blending strategy converges to a CDCS strategy. This is consistent with the fact that the CDCS strategy implicitly assumes the cost of fuel is infinitely more than the cost of electricity. Secondly, for sufficiently low β (i.e. electricity becomes more expensive than fuel), the optimal blending strategy *generates* electric energy. The implicit assumption leading to this result is that the driver is able to sell energy back to the grid when the vehicle is plugged in. Although electricity prices are unlikely to be this high in general, real-time pricing could motivate using the vehicle as a distributed power generator during periods of peak demand when conventional generation is scarce [13]. This suggests that, with the appropriate exchange of information, a vehicle could be configured to modify its control policy in real time to reflect grid conditions, a key benefit when considering vehicle-to-grid infrastructures.

3.3   Impact of Varying Battery Size

In this section our goal is to analyze the coupling between battery size and control strategy. Specifically, our aim is to quantify how control strategy choice enables the use of smaller battery sizes, in terms of both operating cost and energy consumption. Smaller battery sizes could be interpreted as a design choice, or a result of capacity fade in a used battery pack. To facilitate this analysis, we first define an analysis methodology. Secondly, we analyze the coupling of control strategy and battery energy capacity in terms of two PHEV performance metrics: operating cost and energy consumption. Third, we consider how daily driving duration (that is, the driving time between PHEV recharge events), affects PHEV performance. Finally, Section 3.3.4 closes with an analysis of control strategy/battery size coupling as a function of the energy price ratio.

3.3.1   Analysis Methodology

Distributions for the PHEV performance characteristics are calculated by simulating each control strategy (Blended and CDCS) and battery size in Table 3.1 configuration over the entire distribution of trip duration and drive cycles. For each battery size option, we synthesize both a blended and CDCS control law as formulated in Section 3.1 - without considering battery health. We then evaluate the performance of the control law / battery size combination by the following approach:

1. Generate optimal control strategies for varying battery sizes (and corresponding vehicle weights) and energy price ratios, subject to the model described in Chapter 2.
2. Randomly generate daily drive cycles from the Markov chain model described in Section 2.3
3. Simulate the closed loop PHEV model across the distribution of random drive cycles, generated in step 2.
4. Record the distribution of performance characteristics
5. Repeat steps 1-4 across a range of energy price ratios

The number of randomly generated drive cycles used to estimate the distribution of performance characteristics is determined by the statistical distribution convergence criterion described in Appendix E. Step 5, which obtains performance characteristics across a range of energy price ratios, furnishes the data presented in Section 3.3.4.
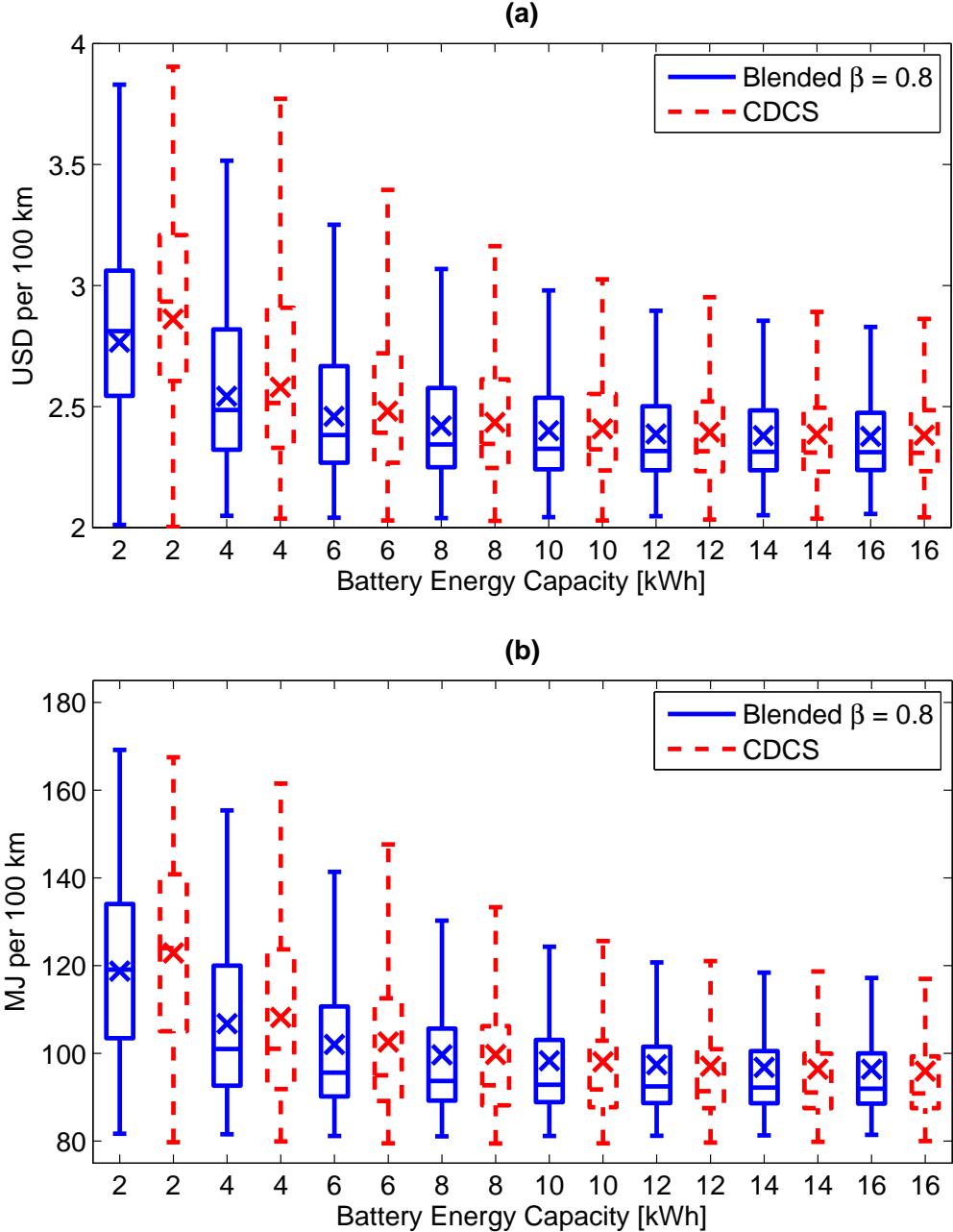
Table 3.1 Battery Pack Energy Capacities, No. of Cells, and PHEV masses

Energy Capacity	No. of Li-ion Cells	PHEV curb weight
2 kWh	263 cells	1374 kg
4 kWh	526 cells	1393 kg
6 kWh	789 cells	1411 kg
8 kWh	1052 cells	1430 kg
10 kWh	1315 cells	1448 kg
12 kWh	1578 cells	1467 kg
14 kWh	1841 cells	1485 kg
16 kWh	2104 cells	1503 kg

3.3.2   Operating Cost & Energy Consumption

Figures 3.8(a) and 3.8(b) respectively depict the distributions of operating cost (USD per 100 km) and energy consumption (MJ per 100 km) across a range of battery energy capacities. The operating cost includes both the cost of fuel from the pump, and electricity from the grid necessary to recharge the battery to its initial SOC level. The distributions are represented by box and whisker plots, where the ($\times$) symbol denotes the distribution average and the whiskers are limited to 1.5 times the interquartile range.

For each battery size we observe that the distribution of operating costs and energy consumption for the blended strategy is consistently better or approximately equal to the CDCS distributions. Moreover, the advantages of blending appear to be more pronounced as battery energy capacity decreases. This can be explained by noting that as battery energy capacity decreases, the probability of fully depleting the battery on a given trip increases for either strategy. This fact is important because, as discussed in 3.2, blending's key advantage is that it increases the time required to fully deplete the battery. This reduces the time spent in costly charge sustenance mode, where the engine is forced out of its sweet spot in order to satisfy drive cycle power demand and regulate the battery SOC. Since the two strategies are roughly cost-equivalent during the charge depletion phase, the differences between them are most prevalent on cycles that force CDCS into charge sustenance mode for a significant period of time. In contrast, for large battery energy capacities, the percentage of trips which fully deplete the battery is relatively small for either strategy. Hence, the two strategies produce almost equivalent performance characteristics for large battery energy capacities.

Figure 3.8 Box and whisker plots of (a) operating cost (USD per 100 km) and (b) energy consumption (MJ per 100 km) distributions for each battery size and control strategy configuration. The symbol (x) denotes the average value of each distribution. Whisker lengths are limited to 1.5 times the interquartile range.

These results are in agreement with prior claims that a blended strategy should enable the use of smaller batteries [140, 141, 143], although in this case the result applies to battery energy capacity, whereas the prior claims are predominantly in reference to battery power capacity. Moreover, this work justifies those claims in
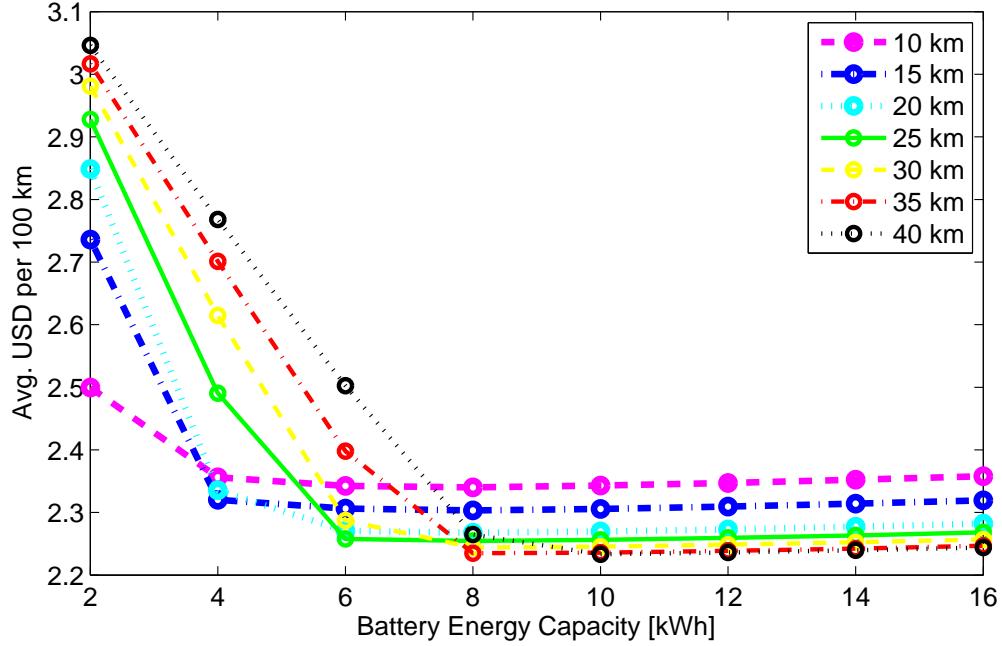
a more rigorous manner by developing blending strategies through optimal control theory. Furthermore, the differences between blending and CDCS are evaluated across a distribution of drive cycle behavior and daily trip times, instead of a small set of certification cycles.

3.3.3   Impact of Varying Daily Trip Distance

This section focuses on the performance of both control strategies across varying daily trip lengths. Namely, we seek to answer the following two questions: (1) Given a fixed daily trip distance, what battery capacity minimizes energy costs? (2) For what range of trip distances does blending provide the greatest improvements over CDCS? The simulation framework used to answer these questions has one important difference with the preceding section: Random drive cycles are simulated for a finite set of trip distances, as opposed to randomly sampled daily trip durations from the distribution described in Section 2.3.

Given a finite set of trip distances, the average operating cost as a function of battery energy capacity is demonstrated in Fig. 3.9, for the blended control strategy. Note that the average is taken over a set of random drive cycles generated by the Markov chain in Section 2.3 (where the simulation is terminated at the specified distance). For each trip distance, operating cost performance is a convex function of battery energy capacity. That is, performance decreases as battery energy capacity increases, up to a critical energy capacity. Beyond this energy capacity, operating cost increases slightly with storage capacity. This slight increase is because vehicle efficiency declines with added battery weight, which is essentially unused for the given trip distance.

The results analyzed in the preceding paragraph can also be leveraged to investigate the relative advantages of blending over CDCS across varying daily trip distances. Figure 3.10 provides the percentage improvement in average operating cost performance of applying a blended strategy over CDCS. In general, blending demonstrates the greatest improvements for small battery energy capacities and long trips - up to 5%. This is because blending rations electric energy storage rather than applying aggressive depletion. The range of battery energy capacity for which blending provides an advantage over CDCS increases as trip distance increases. However, beyond a certain battery size, there is a small probability that either strategy will fully deplete the battery and therefore differences between blended control and CDCS are small. In fact, for large batteries blending provides slightly worse performance than CDCS
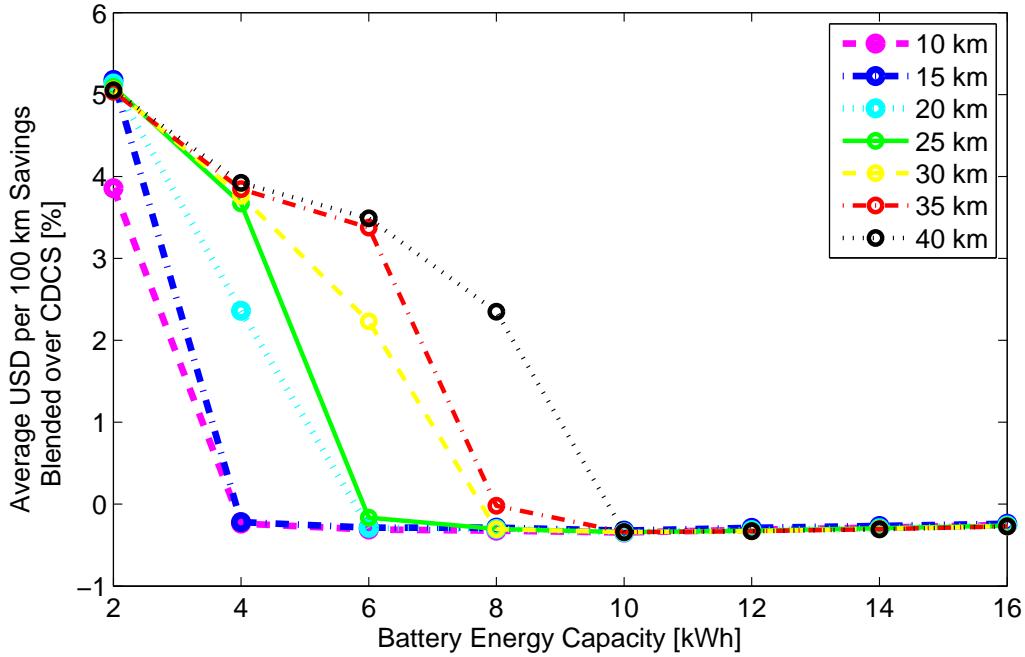
Figure 3.9 Average operating cost (USD per 100 km) for varying daily trip distances and battery energy capacities, for the blended strategy.

because blending applies more engine power during charge depletion to conserve electric energy. Nevertheless, Fig. 3.10 is useful for understanding the ranges of trip distances and battery energy capacities where blending provides significant benefits over the standard CDCS control strategy.

3.3.4 Impact of Varying Energy Prices
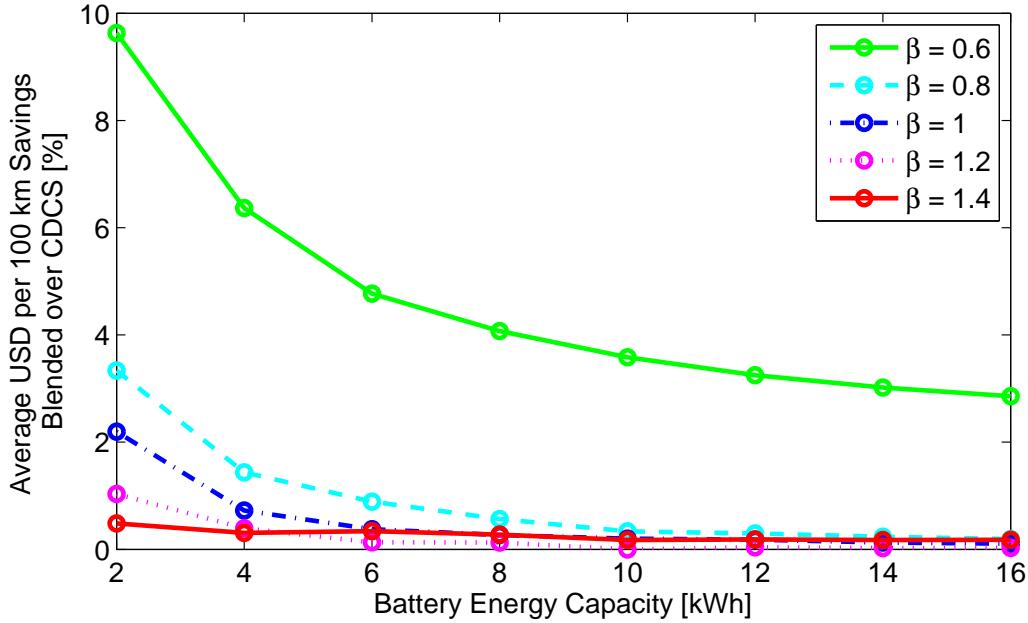
To this point we have reported results corresponding to an energy price ratio of $\beta = 0.8$ (equivalent to the gasoline price per gallon being 27.6 times the electricity price per kWh – for example, 2.76 USD per gallon of fuel and 0.10 USD per kWh of electricity). This parameter is explicitly accounted for in both the control design procedure and simulation results. However, this value varies both temporally (e.g., by year) and spatially (e.g., by geographic region). To highlight the volatility of this parameter, consider the history of average energy price ratios in the United States since 1973 [6], shown in Fig. 3.6. The value of β has clearly changed significantly over the past 35 years due to shifts in both oil and electricity prices. This motivates the need to understand how this parameter impacts the interdependency of optimal power management and battery energy capacity.

Figure 3.10 Impact of daily trip distance on operating cost savings of applying a blended strategy relative to CDCS.

Consider the operating cost savings (given in terms of percentage) of applying a blended strategy over CDCS in Fig. 3.11. Since the proposed simulation method produces a distribution of operating cost savings for each energy price ratio, Fig. 3.11 provides the average values calculated across all the drive cycles.

Two key observations are made from the results depicted in Fig. 3.11. First, the benefits of blending over CDCS is more significant for smaller battery energy capacities, across all values of the energy price ratio. This result matches the trends identified in the previous section and quantifies the benefits across varying energy price ratios. Secondly, the benefits of applying a blended strategy over CDCS become notably more significant for smaller values of β, i.e. as fuel becomes less expensive relative to fixed electricity prices. This result makes intuitive sense for the following reason: Recall that the blended approach explicitly accounts for the cost of fuel *and* electricity, and therefore optimally mixes these energy sources in a manner that minimizes total energy consumption costs. In the case of decreasing values for the energy price ratio, blending utilizes increasing amounts of engine power and fuel. As a result, the optimal fuel/electricity mix deviates further from the CDCS strategy, which always attempts to consume electric battery energy first. The final result is that blending produces
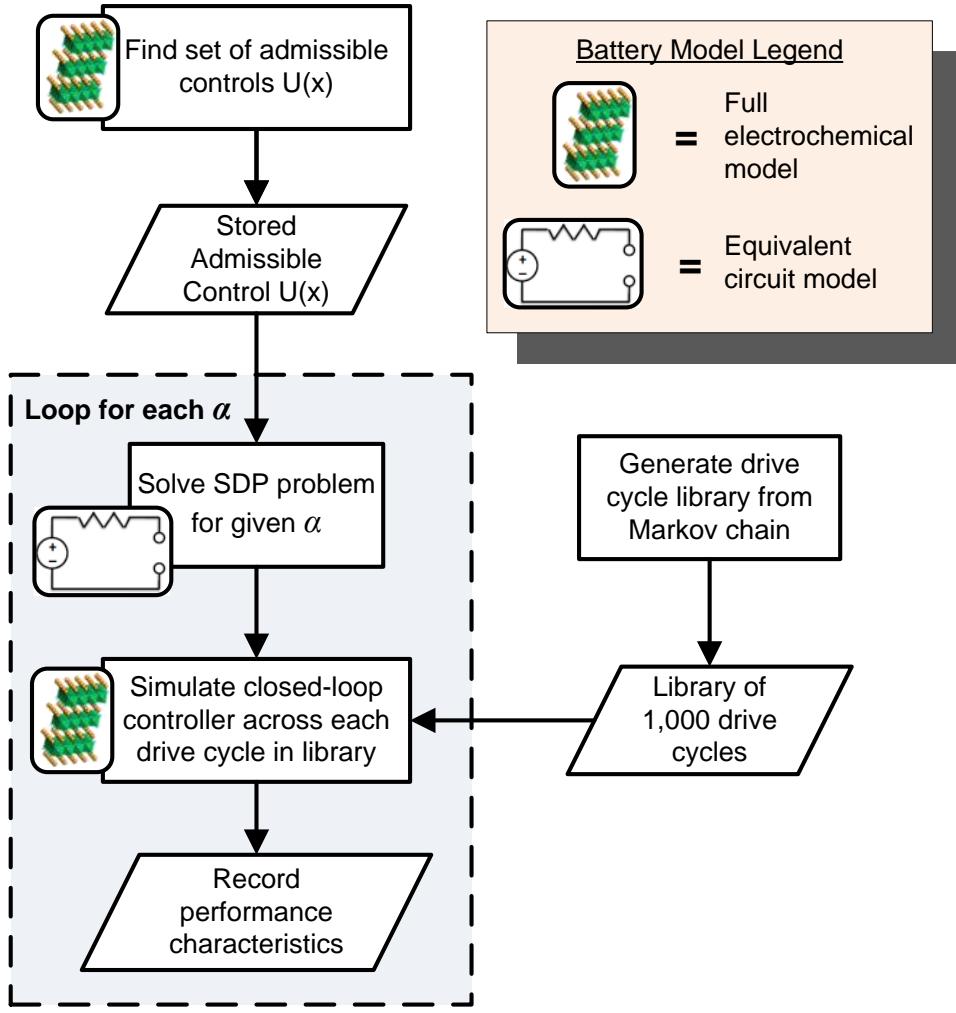
Figure 3.11 Impact of energy price ratio on operating cost savings of applying a blended strategy relative to CDCS. Recall the definition of energy price ratio provided in (3.10).

significantly lower operating cost values relative to CDCS for small energy price ratios.

3.4 Optimal Blending to Minimize SEI Layer

This section examines the performance of supervisory control algorithms that optimally tradeoff SEI film growth with energy consumption cost. To obtain a measure of controller performance across a variety of drive cycle behavior (as opposed to single certification cycles), we apply the process outlined in Fig. 3.12. This can be summarized as follows:

1. The set of admissible controls is determined for each state using the electrochemical model.

2. The Pareto optimal set of controllers is synthesized via the stochastic dynamic program formulated in Section 3.1 by sweeping α and considering the reduced equivalent circuit model.

3. A library of 1,000 drive cycles is generated from the Markov chain described in Section 2.3.

4. Each controller in the Pareto set is simulated for all drive cycles in the library

66
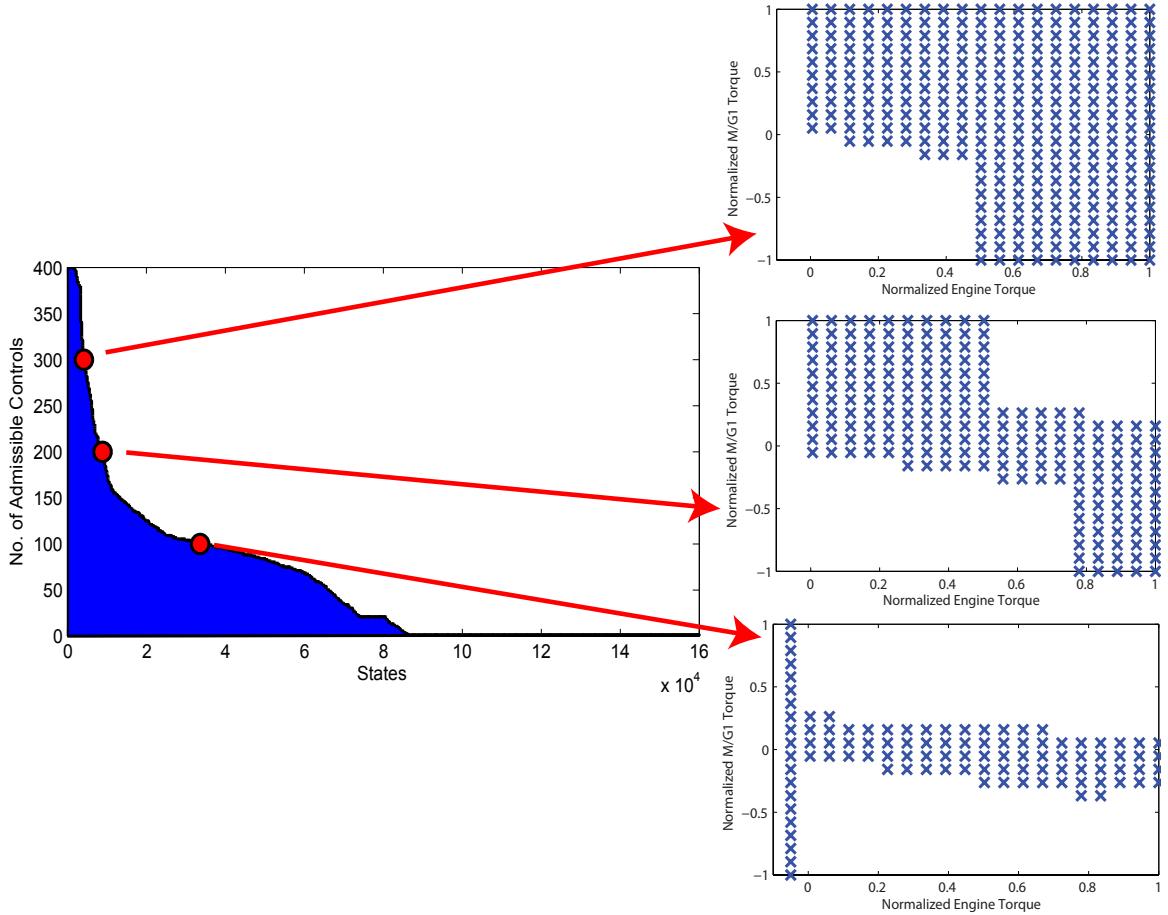
Figure 3.12 Flowchart of the design and analysis procedure. Note that the full electrochemical model is used to compute the admissible control set and simulate the closed-loop system after the SDP problem has been solved. The reduced equivalent circuit model is used to solve the SDP problem, since it contains only one state.

with the full electrochemical model.

5. Performance characteristics, including film growth and energy cost, are recorded.

Subsequently, we analyze three controllers of interest from the Pareto set on single certification cycles to obtain a fundamental understanding of how to optimally tradeoff battery health and energy consumption through proper SOC management.

Figure 3.13 Number of admissible controls for each state, sorted in descending order. Sets of admissible controls for three examples states are shown on the right.

Admissible Controls

At this point we wish to highlight Step 1, where the set of admissible controls is determined for each state using the electrochemical model. This step is critical for three reasons.

First, computing admissible controls for each state off-line guarantees that the constraints are always satisfied. In other words, they are implemented as *hard* constraints. A typically alternative in hybrid vehicle power management applications is to apply penalty functions when constraints are violated - a *soft* constraint approach [37, 73, 53]. The latter has been shown to cause numerical difficulties due to interpolation leakage of the penalty function values into the admissible region [144].

The second critical reason for computing admissible controls offline is that it ensures the controllers satisfy the constraints on the full electrochemical model, despite being

optimized on the reduced equivalent circuit model. This point is crucial for integrating electrochemical models into stochastic dynamic programming - a key contribution of this dissertation.
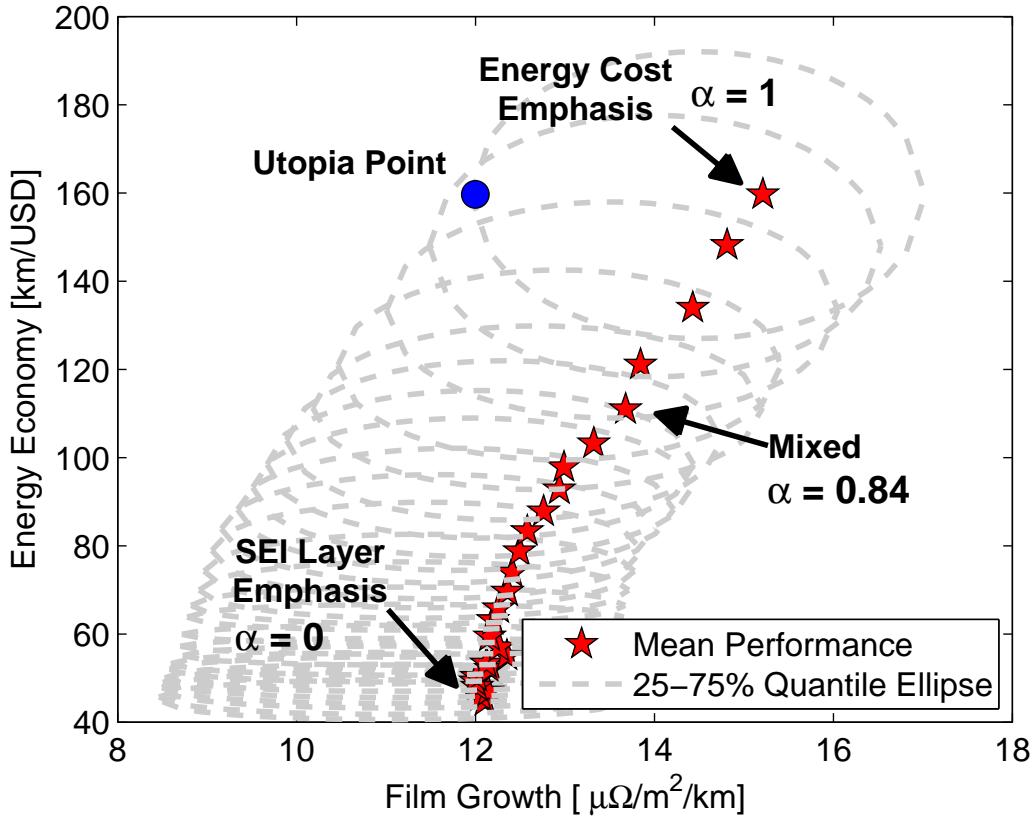
Finally, computing admissible controls offline can dramatically reduce the control space one needs to consider during the online SDP calculation. To demonstrate this point Fig. 3.13 displays the number of admissible controls for each state, sorted in descending order. Note that there are four state variables, quantized at 20 levels each, resulting in 160,000 states. The two control inputs are also quantized at 20 levels, resulting in 400 possible controls. Figure 3.13 demonstrates that 86% of the control space is reduced through this offline calculation, a significant reduction to say the least. The plots on the right-side of Fig. 3.13 further demonstrate the non-trivial nature of determining admissible controls for each state. That is, these three plots show the exact sets of admissible controls for three example states, which contain 300, 200, and 100 admissible controls, displayed respectively from top to bottom.

The results from computing the admissible controls are saved into a database, which SDP uses to determine the set over which to optimize controls for each state. This offline calculation does not depend on the specific optimization objective, and can thus be performed once. As such, the database of admissible controls are used to minimize SEI layer growth and Ah-processed in the subsequent sections.

3.4.1 Energy Consumption vs. Film Growth

Performance results for the Pareto set of controllers that optimally tradeoff SEI layer film growth (per battery cell) with energy consumption costs are presented in Fig. 3.14. This is achieved by sweeping the weighting parameter α in (3.6) from zero to one. A distribution of performance metrics is obtained for simulating the controllers across the entire library of drive cycles. As such, Fig. 3.14 indicates the average values as well as the 25/75% quantile ranges. The horizontal axis reports the SEI layer growth resistance per km, while the vertical axis indicates energy economy in km/USD (analogous to miles per gallon). The utopia point is located in the upper-left, which indicates the individually achievable optimal performance metrics [145].
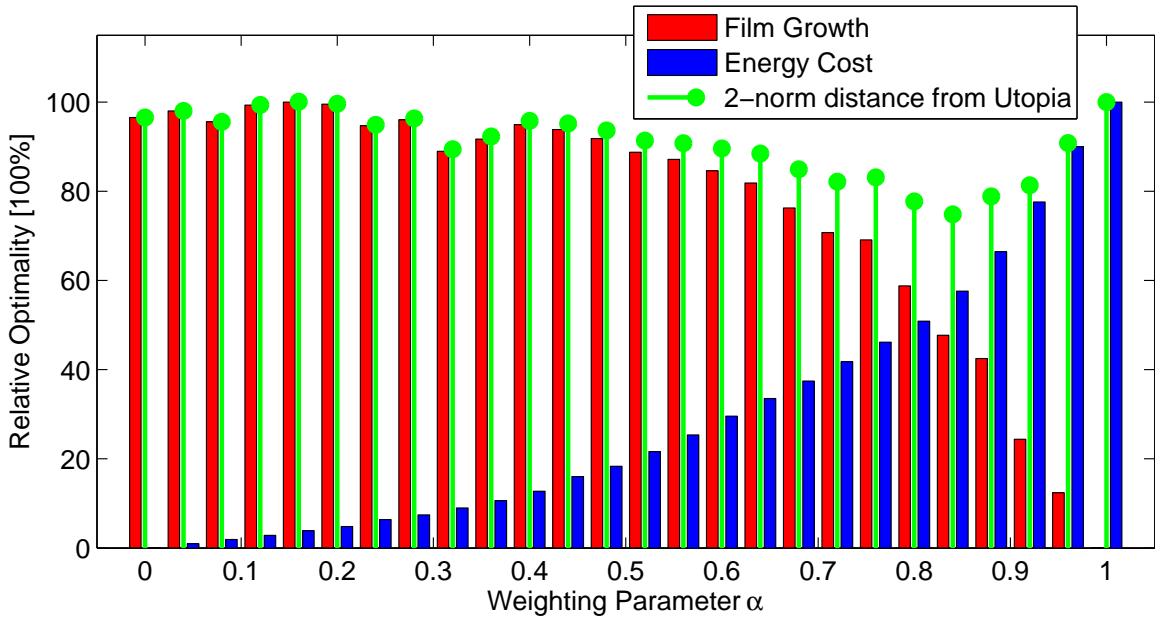
This plot indicates that, indeed, there exists a fundamental tradeoff between anode-side SEI film growth in battery packs and energy consumption costs. Namely, average SEI film growth can be reduced by 20% relative to an "energy-only" controller, but at the sacrifice of a 72% decrease in average energy economy. The reason the distributions of film growth stretch left of the mean is related to the distribution of

Figure 3.14 Pareto set of optimal controllers for anode-side film growth and energy economy, simulated across a library of 1,000 randomly generated drive cycles. Stars ($\star$) indicate the average values and the dashed lines (- -) are the 25/75% quantile range.

trip length. As trips become longer, more battery SOC is depleted and film growth rate decreases. Normalizing this effect against longer distances traveled produces a long tail toward the left side of Fig. 3.14.

One method for analyzing the combined optimality of each controller is to consider the relative optimality analysis depicted in Fig. 3.15. This figure reports on the optimality of each controller with respect to the Utopia point defined in Fig. 3.14. Note that the relative optimality is nearly (but not exactly) a monotonic function of controller weighting α. This is because the stochastic dynamic programming procedure optimizes with respect to the reduced order equivalent circuit battery model, whereas these results are calculated from the full electrochemical model (see Fig. 3.12). One can see that the controller corresponding to $\alpha = 0.84$ provides the minimum 2-norm distance from the Utopia point, and in this specific sense, is the best balance between both objectives. In the following analysis, we discuss the two extreme solutions ($\alpha = 0$
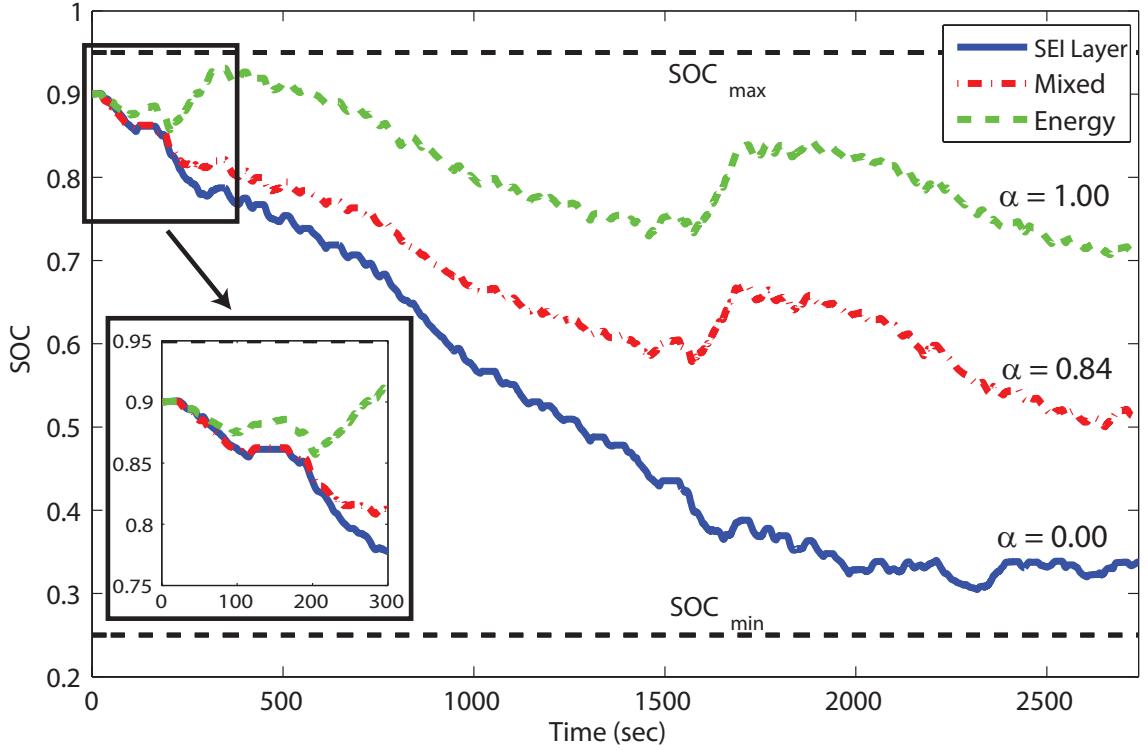
Figure 3.15   Relative optimality of each controller depicted in Fig. 3.14 with respect to each individual objective. The stems are proportional to the 2-norm distance from the Utopia point in Fig. 3.14

and $\alpha = 1$) and the "best mix" ($\alpha = 0.84$).

3.4.2   Analysis and Discussion
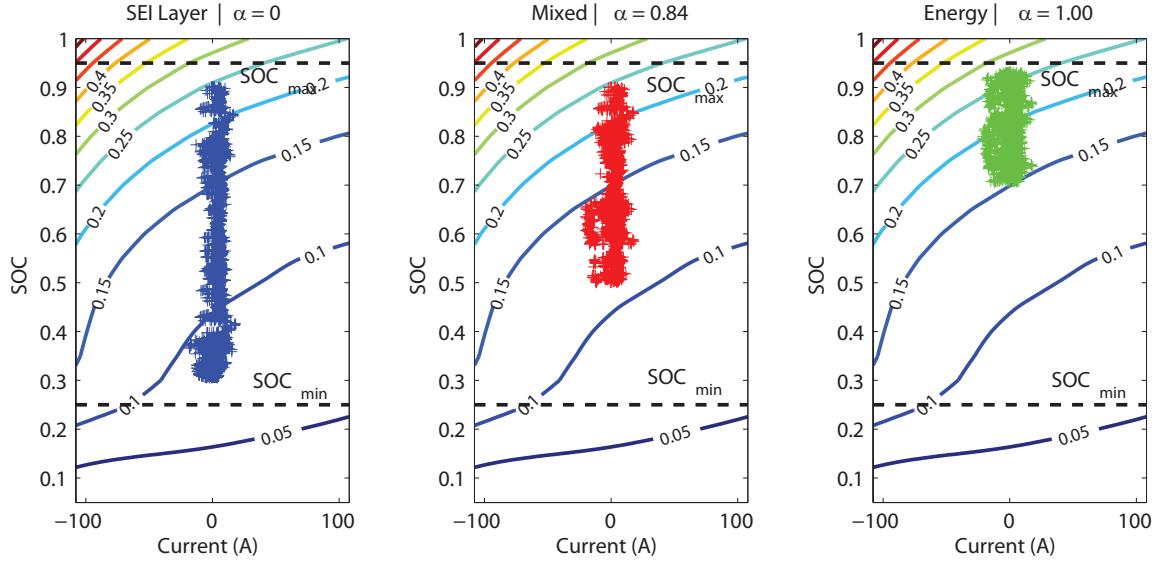
To acquire physical insight into the structural properties of the optimal controllers, we analyze three solutions from the Pareto set, $\alpha = 1.0, 0.84$, and 0. Generally speaking these respectively correspond to emphasizing energy only, balancing energy and SEI layer growth, and SEI layer growth only. The controller corresponding to $\alpha = 0.84$ is chosen because it represents the best balance between both objectives, measured in terms of the normalized 2-norm distance from the utopia point in Fig. 3.14. These controllers are simulated on two concatenated FTP-72 cycles. Performance results for various other drive cycles are reported in Table 3.2.

Figure 3.16 demonstrates the SOC trajectories for each controller. The energy-only controller ($\alpha = 1.0$) conservatively rations battery charge by blending engine and battery power. This process reduces the time spent in charge sustenance mode, where fuel must be consumed to meet power demand and sustain battery charge [42]. Put simply, charge sustenance mode is extremely expensive relative to charge depletion, and should be avoided, if possible, to reduce energy consumption cost. If the drive cycle

Figure 3.16 SOC trajectories for SEI film growth ($\alpha = 0$), mixed ($\alpha = 0.84$), and energy ($\alpha = 1.0$) optimal controllers simulated on two concatenated FTP-72 cycles.

were known beforehand, the optimal strategy would blend engine and battery power so battery SOC reaches its minimum level exactly when the trip terminates. Recall that trip length distributions are directly implemented into the problem formulation through the terminal state of the Markov chain, as described in Section 2.3. Hence the controller is trip length-conscious. In contrast, the SEI layer-only controller ($\alpha = 0$) aggressively depletes battery charge to avoid the high SEI film growth rates seen in Fig. 2.6. This results in a strategy that mimics electric-only operation, followed by charge sustenance. Interestingly, the mixed ($\alpha = 0.84$) controller's characteristics are more similar to $\alpha = 0$ than $\alpha = 1$ during the first 300 seconds (see the zoom-in in Fig. 3.16. The reason can be understood by analyzing the gradient properties of the film growth map. Namely, the steep gradient at high SOC values indicates significant benefits in accumulated film growth can be achieved by quickly depleting charge. This is in spite of heavily weighting energy costs over battery health, since instantaneous energy cost as defined in (3.7) is relatively insensitive to SOC. Conversely, SEI film

Figure 3.17 Operating points on anode-side SEI film growth rate map for SEI layer ($\alpha = 0$), mixed ($\alpha = 0.84$), and energy ($\alpha = 1.0$) optimal controllers simulated on two concatenated FTP-72 cycles.

growth is very sensitive to SOC. Mathematically this is shown from (3.7)-(3.8)

$$\frac{\partial c_{film}}{\partial SOC} \quad \gg \quad \frac{\partial c_{energy}}{\partial SOC} \tag{3.23}$$

$$\Leftrightarrow \frac{\partial \dot{\delta}_{film}(I, SOC)}{\partial SOC} \quad \gg \quad -\alpha_{elec} \frac{Q_{batt} \dot{SOC}}{\eta_{grid}} \frac{dV_{oc}(SOC)}{dSOC} \approx 0 \tag{3.24}$$

where the RHS of (3.24) is approximately zero because a typical Li-ion battery has nearly constant open-circuit voltage with respect to SOC, in the allowable SOC range.

This result is clearly illustrated in Fig. 3.17, which indicates the operating points of each controller superimposed on the film growth map from Fig. 2.6. Observe that adding a small consideration for SEI layer growth (e.g. $\alpha = 0.84$) to an energy-only objective (e.g. $\alpha = 1.0$) dramatically changes the operating point behavior. Namely, it induces the controller to escape high film growth rate regions by depleting battery charge quickly until it reaches a lower SOC level (between 50-60%). However, it leaves enough available battery energy to blend power until the trip ends, without entering charge sustenance (near 25% SOC). In summary, a PHEV power management strategy that considers SEI film growth in addition to energy consumption will, in general: (1) deplete battery charge quickly to reduce film growth rates, then (2) blend engine and battery power to avoid charge sustenance, at least for the models considered in this dissertation.

Table 3.2 Performance over various Certification Cycles

Drive Cycle	Energy Economy [km/USD]			Film Growth [$\mu\Omega/\text{m}^2/\text{km}$]		
	SEI $\alpha = 0.00$	Mixed $\alpha = 0.84$	Energy $\alpha = 1.00$	SEI $\alpha = 0.00$	Mixed $\alpha = 0.84$	Energy $\alpha = 1.00$
3xFTP	46.5	187	434	14.0	17.9	22.4
3xUS06	37.1	80.7	88.3	5.25	6.01	6.58
6xSC03	50.0	170	312	13.2	16.2	20.0
3xHWFET	44.9	173	266	5.15	6.48	7.96
3xLA92	39.6	150	263	10.6	13.0	16.2

3.4.3 Sensitivity to Film Growth Model Parameters

The property that batteries degrade faster at higher SOC strongly influences the results presented here. This fact motivates an analysis of how sensitive the gradient properties of the film growth map in Fig. 2.6 are to variations in the model parameters. Namely, are the gradient properties a fundamental physical property of the film growth mechanism, or a realization of the particular model parameters used in this study? The answer is the former, as shown by the following proposition.

Proposition 1. *Consider a rested battery cell with constant concentration and potential distributions, zero applied current, and hence zero intercalation current $J_1 = 0$. Then the rate of anode-side film growth increases with cell SOC,*

$$\frac{\partial \dot{\delta}_{film}}{\partial \theta_a} > 0 \quad \forall \quad \theta_a \in [0,1] \tag{3.25}$$

where θ_a is the bulk state-of-charge of the anode, which we use as the definition of cell SOC. Moreover, the only model property necessary to ensure this result is that anode equilibrium potential is decreasing with SOC, $dU_{ref,a}/d\theta_a < 0$, which is a thermodynamic electrochemical property of porous lithiated carbon electrodes [146]. Thus film growth rate is an increasing function of SOC, for a rested cell under no loads.

Proof. First consider the Butler-Volmer equation for the anode.

$$J_1 = a_0 i_{0,a} \sinh\left[\frac{\alpha_a F}{RT}\left(\phi_{1,a} - \phi_{2,a} - U_{ref,a} - \frac{J_1}{a_n}R_{film}\right)\right] \tag{3.26}$$

74

The following expression holds true if and only if $J_1 = 0$ in (3.26).

$$\phi_{1,a} - \phi_{2,a} = U_{ref,a}(\theta_a) \tag{3.27}$$

The simplifying condition (3.27) enables us to analytically show $\partial \dot{\delta}_{film}/\partial \theta_a > 0$ through the following arguments. First we derive $\dot{\delta}_{film}$ as an explicit function of θ_a. Then we show its derivative is positive. Rewrite (2.24) and (2.25) by lumping together parameters into positive constants C_1, C_2, C_3, and then combine

$$\dot{\delta}_{film} = C_1 C_2 \exp\left[-C_3 \eta_s\right] \tag{3.28}$$

Use the definition of η_s from (2.18) and condition (3.27) to write

$$\eta_s = U_{a,ref}(\theta_a) - U_{s,ref} \tag{3.29}$$

noting that the third term in (2.18) is dominated by the others and can be approximated as zero. Substitute η_s into (3.29)

$$\dot{\delta}_{film} = C_1 C_2 \exp\left[-C_3\left(U_{a,ref}(\theta_a) - U_{s,ref}\right)\right] \tag{3.30}$$

Now differentiate with respect to θ_a

$$\frac{\partial}{\partial \theta_a}\left(\dot{\delta}_{film}\right) =$$
$$\left[-C_1 C_2 C_3 \exp\left(-C_3(U_{a,ref}(\theta_a)) - U_{s,ref})\right)\right]\left[\frac{dU_{a,ref}}{d\theta_a}\right] \tag{3.31}$$

The first term in brackets on the RHS of (3.31) is negative for all θ_a, since the constants C_1, C_2, C_3 are positive by definition and the exponential function is always positive. Hence, $\partial \dot{\delta}_{film}/\partial \theta_a > 0$ if and only if the second term in brackets in (3.31) is negative. That is, the equilibrium potential of the anode decreases with bulk anode SOC. This condition is a thermodynamic property of lithiated carbon electrodes [146]. Therefore (3.25) holds true, which completes the proof. □

This result implies anode-side film growth rate increases as SOC increases irrespective of the model parameters, at least for a rested battery under zero loads. Experimental validation of this result has been reported in the literature [106] and is currently underway in our laboratory. This evidence provides confidence in the trends and insights reported here.

In this study we focus on one particular battery degradation mechanism - anode-side film growth. In truth a myriad of mechanisms exist that cause capacity fade in lithium-ion batteries, although film growth has been identified as one of the most significant [30]. A comprehensive review of these mechanisms can be found in [30] and the references therein. From a systems-level perspective degradation can be associated with SOC, temperature, depth of discharge, cycling, etc. Experiments identifying several of these relationships are currently underway in our laboratory. Nonetheless the application of an established degradation model [7] represents a reasonable first step toward health-conscious power management.
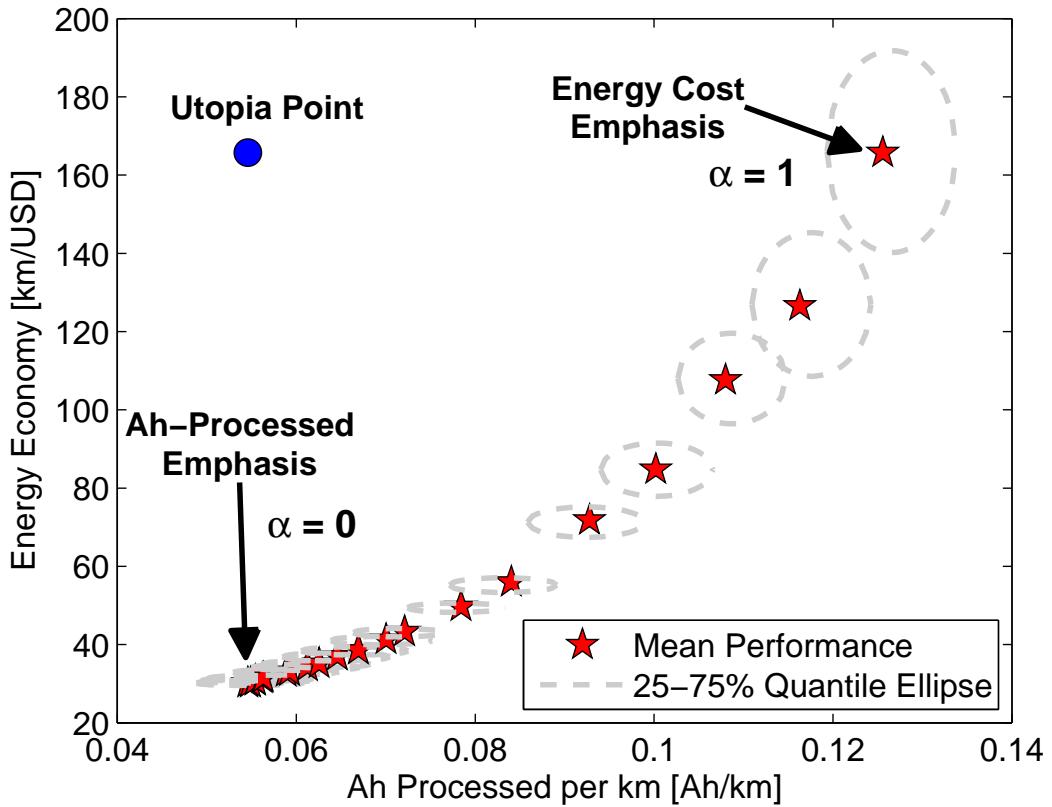
3.5   Optimal Blending to Minimize Ah-Processed

In this section we examine the performance of supervisory control algorithms that optimally tradeoff Ah processed with energy consumption cost. The analysis follows the exact same procedure outlined in the previous section (Section 3.4) and Fig. 3.12. In particular we analyze the Pareto frontier of optimal solutions and their relative optimality. For additional insight, we consider the controllers which optimize each objective individually and compare their performance on three concatenated US06 cycles.

3.5.1   Energy Consumption vs. Ah Processed

Performance results for the Pareto set of controllers that optimally tradeoff Ah processed (per battery cell) with energy consumption costs are presented in Fig. 3.18. As before, this is achieved by sweeping the weighting parameter α in (3.6) from zero to one. A distribution of performance metrics is obtained for simulating the controllers across the entire library of drive cycles. As such, Fig. 3.14 indicates the average values as well as the 25/75% quantile ranges. The horizontal axis reports the Ah processed per km, while the vertical axis indicates energy economy in km/USD (analogous to miles per gallon). The utopia point is located in the upper-left, which indicates the individually achievable optimal performance metrics [145].

This plot indicates that a fundamental tradeoff also exists between reducing energy consumptions costs and Ah processed in battery packs, for PHEVs. Specifically, the average Ah processed can be reduced by 57% relative to an "energy-only" controller, but at the sacrifice of an 82% decrease in average energy economy. One method

76
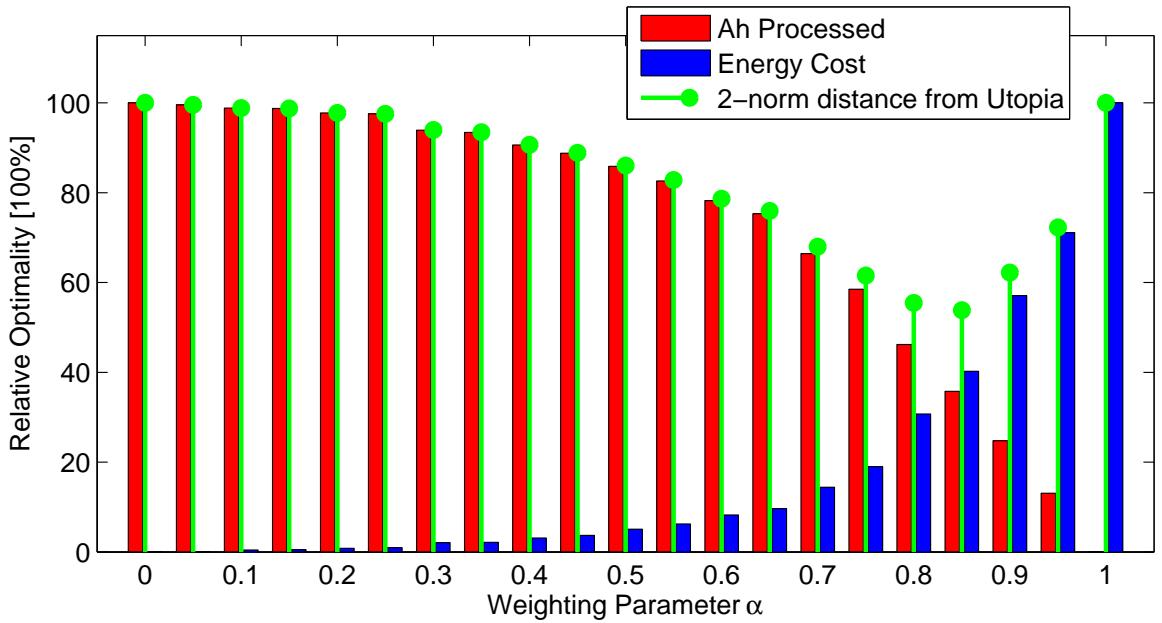
Figure 3.18 Pareto set of optimal controllers for Ah processed and energy economy, simulated across a library of 1,000 randomly generated drive cycles. Stars ($\star$) indicate the average values and the dashed lines (- -) are the 25/75% quantile range.

for analyzing the combined optimality of each controller is to consider the relative optimality analysis depicted in Fig. 3.19. This figure reports on the optimality of each controller with respect to the Utopia point defined in Fig. 3.18. One can see that the controller corresponding to $\alpha = 0.85$ provides the minimum 2-norm distance from the Utopia point, and in this specific sense, is the best balance between both objectives.

3.5.2   Analysis and Discussion

As before, we acquire physical insight into the structural properties of the optimal controllers by analyzing the two extreme solutions from the Pareto set, $\alpha = 0$ and 1.0. These two controllers corresponding to emphasizing minimum Ah-processed and minimum energy consumption cost, respectively. These controllers are simulated on two concatenated US06.
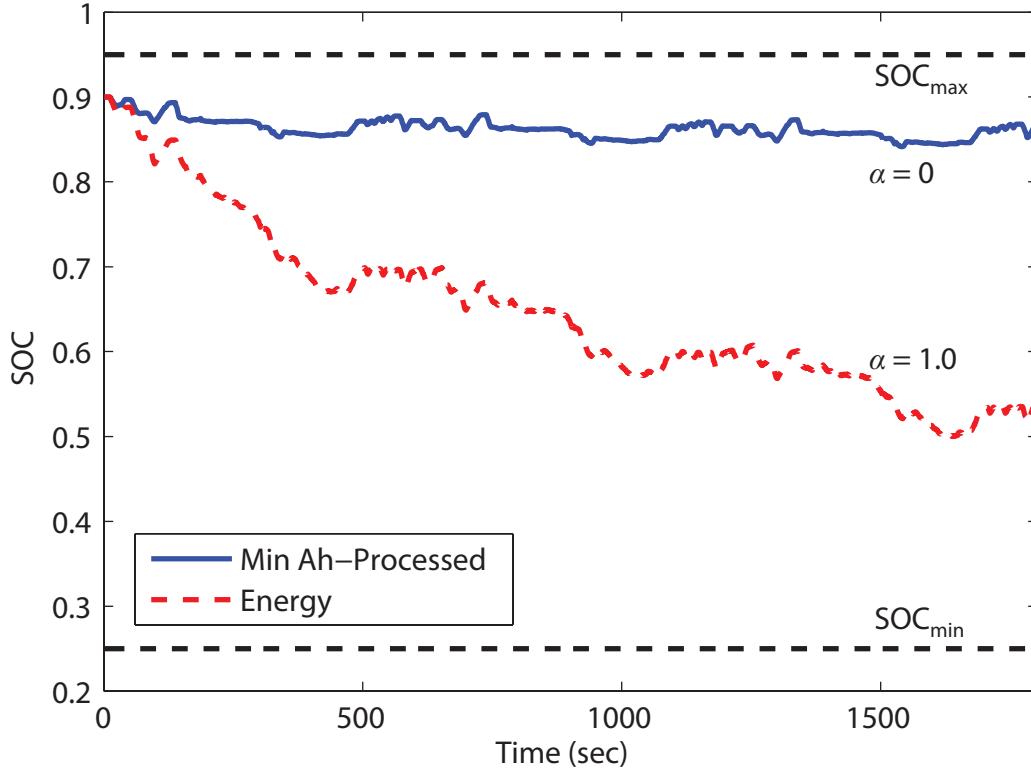
Figure 3.19 Relative optimality of each controller depicted in Fig. 3.18 with respect to each individual objective. The stems are proportional to the 2-norm distance from the Utopia point in Fig. 3.18

Figure 3.20 portrays the SOC trajectories for each controller. As before, the energy-focused controller rations battery charge such that the PHEV reaches the minimum SOC over the course of an average drive cycle. This effectively reduces the time spent in charge sustenance mode while completely utilizing the relatively cheap electric energy store. In contrast to the results shown in Fig. 3.16, the minimum Ah-processed controller severely limits high C-rates and therefore consumes a very small amount of battery energy (about 5% depth of discharge).

This behavior can be understood further by analyzing the distribution of power demand on the engine and battery, depicted in Fig. 3.21. This figure elucidates how the minimum Ah-processed controller constraints the distribution of battery power demand to a small range around 0 kW, which limits the depth of discharge. The tradeoff is a larger number of high engine power occurrences, as shown in the top subplot of Fig. 3.21, to satisfy the total power demand. In contrast, the energy-focused controller experiences a broad range of battery power demand and a distribution of engine power more closely concentrated toward lower values, which decreases total energy consumption cost. Therefore, a PHEV supervisory control algorithm which attempts to minimize battery health degradation by reducing Ah-processed will be extremely cautious of using the battery as a depletable energy store. Interestingly
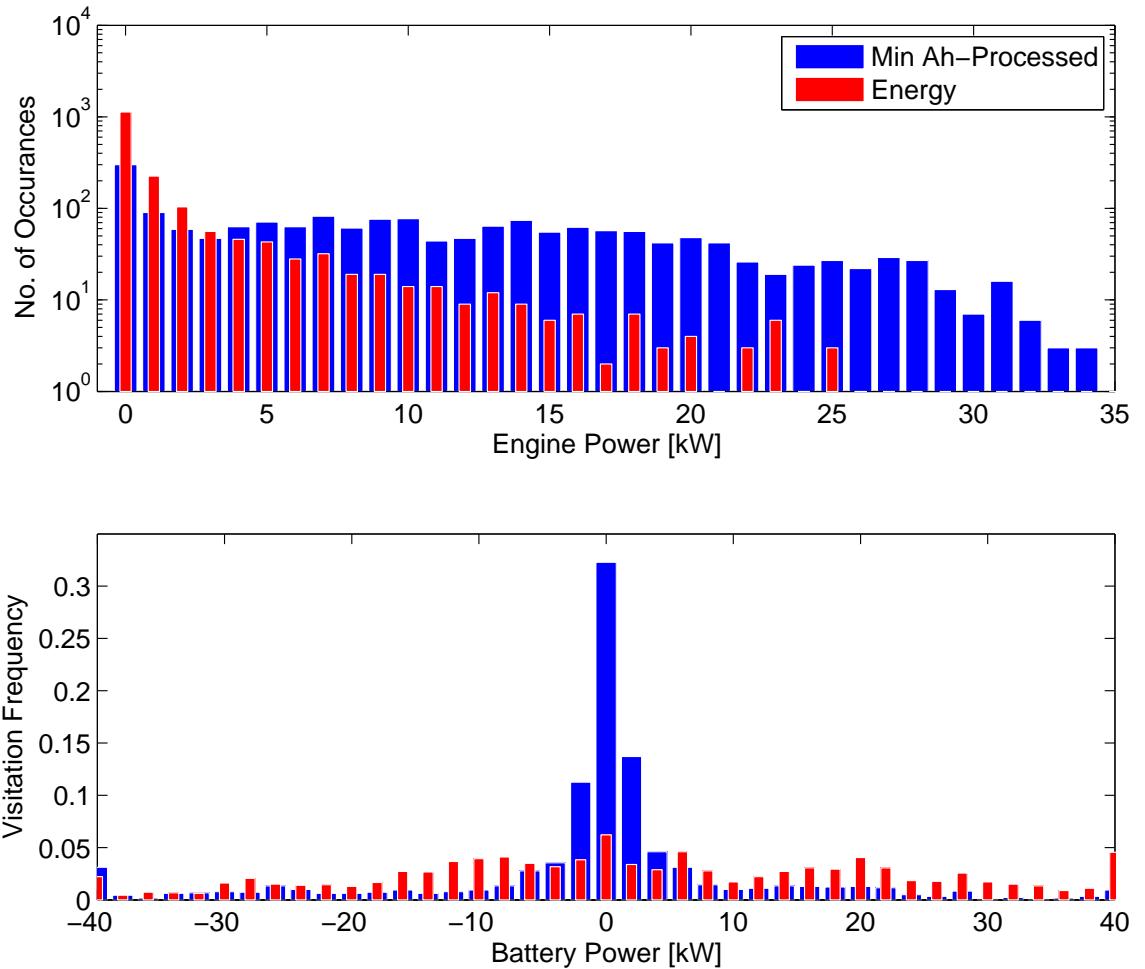
this action fundamentally opposes the key advantageous feature of a PHEV - the depletable battery pack energy store.

Figure 3.20   SOC trajectories for minimum Ah-processed ($\alpha = 0$) and energy ($\alpha = 1.0$) simulated on three concatenated US06 cycles.

3.6   Summary

This chapter examines health-conscious power management in plug-in hybrid electric vehicles through electrochemical modeling and stochastic control. The framework presented here is the first integration of electrochemical modeling and stochastic control. First we consider the optimal blending problem without consideration for battery health. The results here demonstrate how blending maintains the engine operating points near the contours of greatest efficiency relative to CDCS. The battery size sensitivity analysis demonstrates that blending has greater impact as battery size decreases. Next, we formulate a multi-objective optimal control problem which optimally trades off battery health in terms of two aging metrics (SEI layer and Ah-processed) with energy consumption cost (fuel and grid electricity). The problem formulation includes

Figure 3.21 Distributions of engine and battery power for minimum Ah-processed ($\alpha = 0$) and energy ($\alpha = 1.0$) simulated on three concatenated US06 cycles.

two levels of battery model fidelity. The first is a reduced degrading electrochemical battery model for control optimization. The second is a full-order electrochemical model for constraint satisfaction and control validation. Throughout this chapter we apply a shortest path stochastic dynamic programming formulation. This enables us to directly encode real-world daily trip length distributions reported by the National Household Travel Survey [121] into the Markov chain drive cycle model.

Analysis of the optimal power management algorithms indicates that an energy-focused controller *conservatively* depletes SOC by blending engine and battery power. This reduces the time spent in charge sustenance mode, where relatively expensive fuel is required to meet driver power demand and sustain battery charge. An SEI-focused

controller *aggressively* depletes SOC, since the SEI layer grows faster at high SOC levels. For the models we study, a controller which considers both objectives will aggressively deplete SOC first, to reduce film growth rates, then conservatively blend engine and battery power to limit entry into charge sustenance mode. In the case of anode-side film growth, we have demonstrated this result is fundamental to the thermodynamic properties of the anode in the battery cell. An Ah-focused controller depletes SOC *extremely conservatively* since it avoids battery power demands with large magnitudes.

The modeling, control design, and analysis procedure presented in this chapter represents a fundamental framework for analyzing power-management of systems with multiple energy stores/conversion devices, stochastic inputs, multiple objectives, complex physics, and state/control constraints.

Chapter 4

Optimal Switching Control of Parallel Connected Batteries

Recent advances in lithium ion battery modeling suggest unequal but controlled and carefully timed charging of individual cells may reduce degradation. This chapter compares anode-side SEI layer formation for a standard equalization scheme versus unequal charging through switches controlled by deterministic dynamic programming (DDP) and DDP-inspired heuristic algorithms. The control optimization utilizes a reduced order model for SEI growth, developed in Section 2.1.3. Using this model, we consider two cells connected in parallel via relay switches. The key results are: (1) Optimal unequal and delayed charging indeed reduces film buildup; (2) A near-optimal state feedback controller can be designed from the DDP solution and film growth rate convexity properties. Simulation results indicate the heuristic state-feedback controller achieves near optimal performance relative to the DDP solution, with significant reduction in SEI growth compared to charging both cells equally, for several film growth models. Moreover, the algorithms achieve similar SEI reduction on the full electrochemical model. These results correlate with the convexity properties of the film growth map. Hence, this chapter demonstrates that controlled unequal charging may indeed reduce SEI growth in parallel connected batteries, given that certain convexity properties exist. Broadly speaking, these techniques introduce a new control paradigm for battery management systems which may significantly improve battery pack life.

4.1   Battery Pack Charge Management Techniques

Existing research on battery management systems (BMS) generally addresses three tiers of objectives. First, researchers have developed cell-to-cell charge equalization circuits that protect cells connected in series strings from over-charging or over-discharging

due to capacity imbalances [147, 148, 112, 111]. Second, researchers have developed thermal models and management systems to ensure cell temperature remains within an optimal efficiency range [103, 125, 104, 102]. These first two tiers usually consider phenomenological lumped parameter models of cells to protect them from abuse. The third tier of health-conscious BMS objectives considers electrochemical-based models, which can potentially predict physical degradation mechanisms with higher fidelity [149]. BMS algorithms within this tier are at a relatively nascent stage, since electro-chemical battery models are significantly more complex than their phenomenological counterparts. Our proposed heterogeneous charging scheme falls within this third tier of objectives. Specifically, we consider the potential advantages of allowing *unequal* charge values across modules connected in parallel, and allow flexibility in determining the *timing* of the charge process. The goal is to leverage this flexibility to suppress capacity fade.

4.2   Problem Formulation

The control objective is to determine the optimal switching sequence that minimizes the total resistive film growth in the battery pack described in Section 2, given a current trajectory, i_0, known *a priori*. We formulate this as a finite horizon constrained optimal control problem

$$\min_{(q_1,q_2)} J \;=\; \sum_{k=0}^{N} \left[\sum_{j=1}^{2} \dot{\bar{\delta}}_{film}(z_{j,k}, i_{j,k}) + g_z(z_k) \right] \\ +\alpha_N \|z_N - 0.95\|_2^2 \tag{4.1}$$

subject to

$$z_{k+1} \;=\; f(z_k, i_k) \tag{4.2}$$

$$i_k \;=\; h(q_k, i_{0,k}) \tag{4.3}$$

$$z_0 \;=\; z_{ic} \tag{4.4}$$

where

$$(q_1, q_2) \in \{0,1\} \times \{0,1\} \tag{4.5}$$

$$g_z(z_k) = \alpha_z \left[\sum_{i=1,2} \max\{0.05 - z_{i,k}, 0, z_{i,k} - 0.98\} \right]^2 +$$

$$\alpha_v \left[\sum_{i=1,2} \max\{2.0 - v_{i,k}, 0, v_{i,k} - 3.6\} \right]^2 \tag{4.6}$$

$$z_k = [z_{1,k} \ z_{2,k}]^T \tag{4.7}$$

$$i_k = [i_{1,k} \ i_{2,k}]^T \tag{4.8}$$
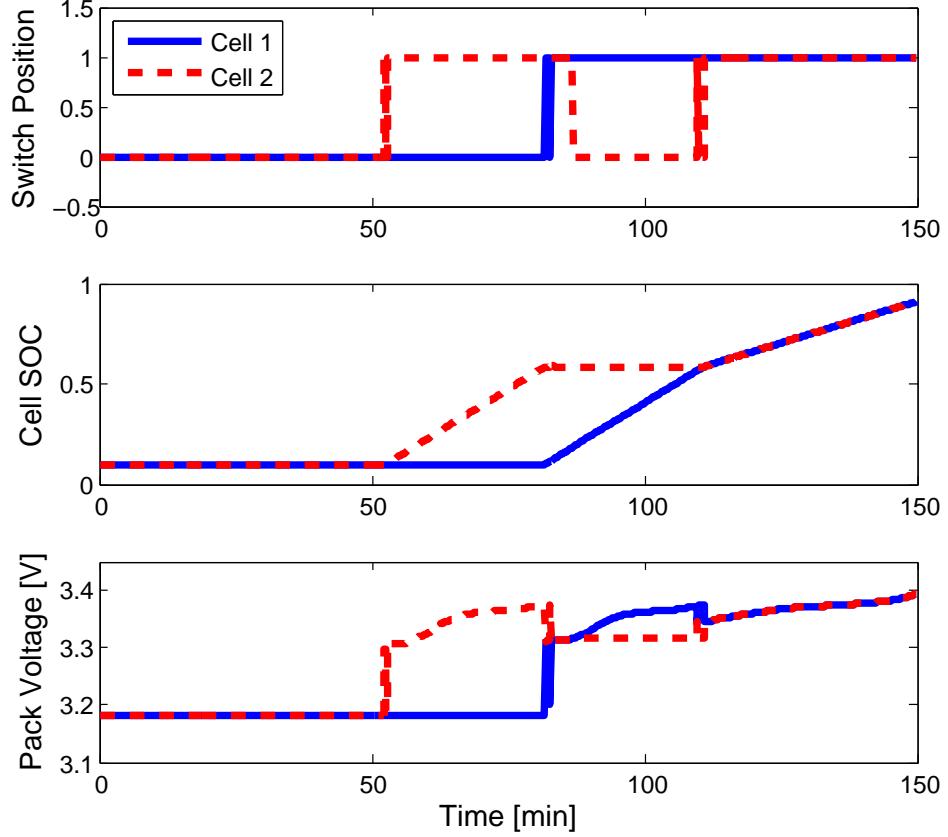
where the function $\dot{\bar{\delta}}_{film}$ maps SOC and current to average film growth rate according to the relationship depicted in Fig. 2.6. The function $g_z(z_k)$ denotes soft constraints that limit cell SOC and cell voltage to protect against over-charging and over-discharging. However, for the simulation described in this article, these constraints never become active due to the modest charging rate employed. A terminal constraint with weighting α_N is provided to ensure the battery pack charges to the SOC corresponding to the desired final voltage. The function $f(z_k, i_k)$ represents the dynamic equation in (2.29)-(2.30). The function $h(q_k, i_{0,k})$ maps the switch position and battery pack current to cell current in (2.31)-(2.32). Finally, we impose a fixed initial condition z_{ic}.

To solve the optimization problem in (4.1)-(4.8), we re-express the equations as a dynamic programming problem by defining a value function as follows [115]: Let $V_k(z_k)$ represent the minimum total film growth from discrete time k to the end of the time horizon, given that the cell SOC in the present time step k is given by the vector z_k. Then the optimization problem can be written as the following recursive Bellman optimality equation and boundary condition.

$$V_k(z_k) = \min_{(q_1, q_2)} \left\{ \begin{array}{l} \sum_{j=1}^{2} \dot{\bar{\delta}}_{film}(z_{j,k}, i_{j,k}) \\ +g_z(z_k) + V_{k+1}(z_{k+1}) \end{array} \right\} \tag{4.9}$$

$$V_N(z_{N-1}) = \min_{(q_1, q_2)} \{\alpha_N \|z_N - 0.95\|_2^2\} \tag{4.10}$$

The above dynamic programming problem is solved via a full enumeration algorithm. That is, we compute a family of optimal trajectories for a set of fixed initial conditions. This approach enables us to analyze an ensemble of trajectories to gain insight on how DDP minimizes total film growth.
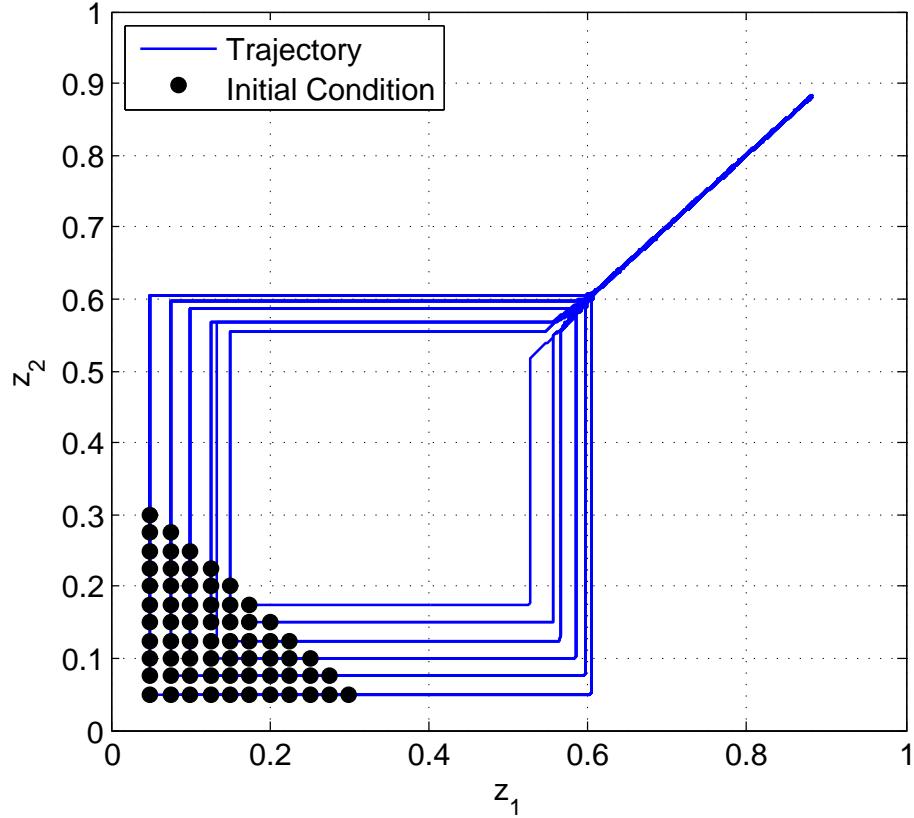
Figure 4.1 Time responses for optimal charging pattern identified by DDP, given a 1C battery pack charge rate.

4.3 Solution Analysis

4.3.1 Analysis of Optimal Trajectories

To acquire insight on the optimal switching sequence for minimizing resistive film growth, we consider a constant 1C (2.3 A) charge rate applied to the battery pack. Note that while the battery pack experiences a constant current charge rate, the individual cells will have time-varying charge rates. Time responses for an initial SOC of 0.1 for each cell are provided in Fig. 4.1. Figure 4.2 demonstrates the optimal trajectories for a set of initial battery cell SOC conditions. These figures indicate that the optimal switching sequence follows a consistent pattern:

1. Leave the battery pack uncharged for as long as possible. This minimizes the duration of time over which the pack's cells have large SOC values and, consequently, large film buildup rates.
2. Charge the cell with greater initial SOC.
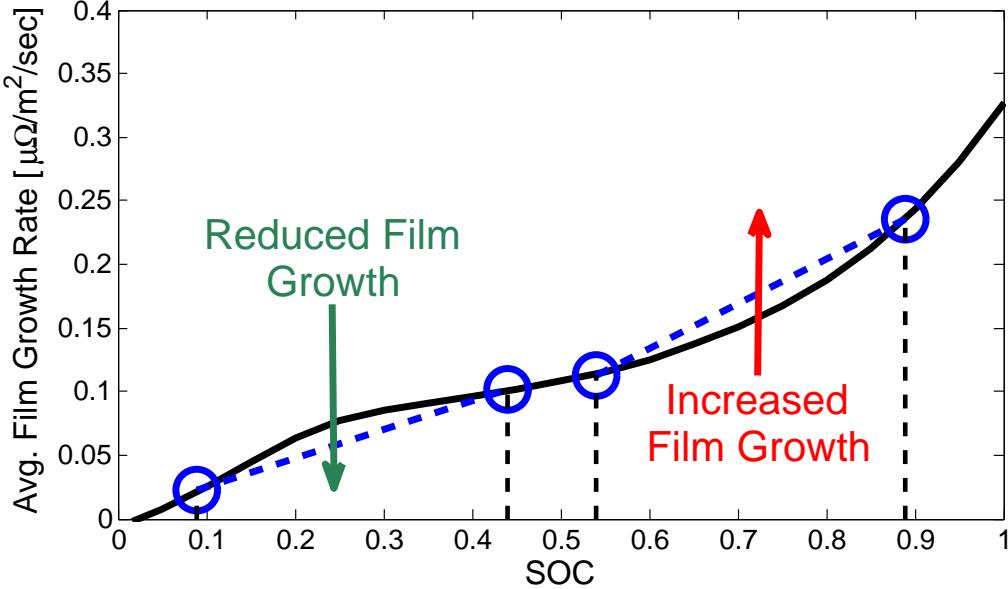
Figure 4.2 Optimal trajectories for various initial conditions, given a 1C battery pack charge rate.

    3. Charge the cell with less SOC until both cells approximately equalize.
    4. Charge both cells together, at approximately equal current values, until the final state is reached.

The key question is why does DDP identify the pattern in Steps 2-4 above as the optimal switching sequence for minimizing film growth?

4.3.2   The Energy Storage-Film Growth Tradeoff

First, consider the result that film growth is minimized by leaving the battery pack uncharged for as long as possible. This is, film growth is minimized if battery packs are charged only immediately before use. This result was also found in a recent study on charge trajectory optimization for plug-in hybrid electric vehicles [150]. The reason for this result can be seen by observing that the film growth rate increases with SOC in Fig. 2.6. Therefore, maintaining each cell in a low SOC reduces the overall film buildup. However, this requires *a priori* knowledge of when the battery pack will be

Figure 4.3 Convexity analysis of spatially-averaged film growth rate for zero applied current.
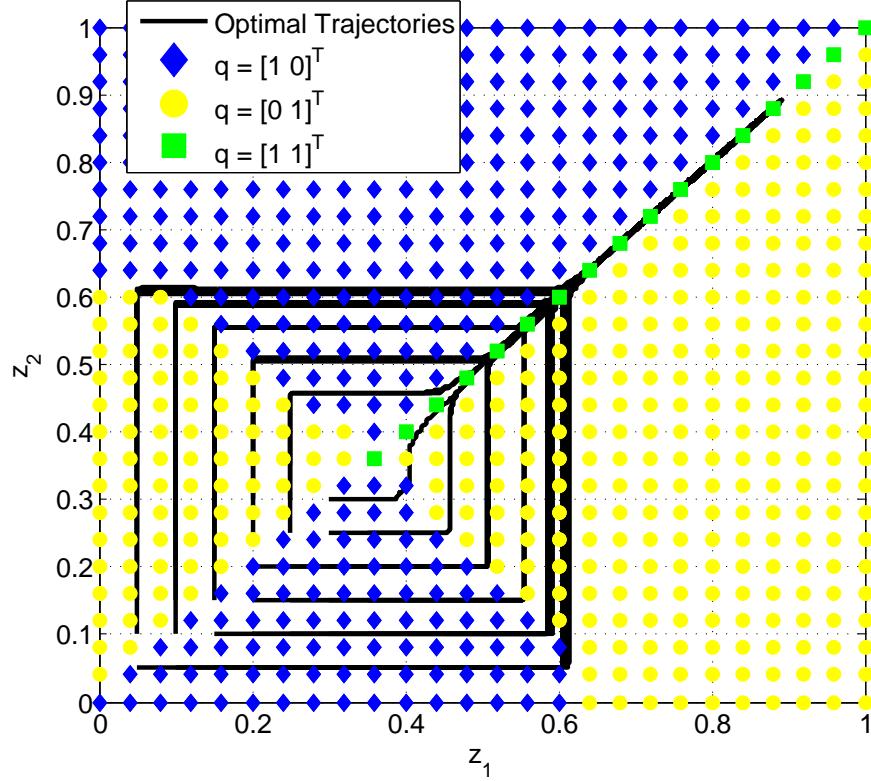
used. Moreover, if the battery is discharged sooner than expected, only a fraction of the total energy capacity is available for use. This suggests a fundamental tradeoff between electric energy storage and reducing anode-side film growth.

4.3.3 Convexity Analysis of Film Growth Rate

To answer the fundamental question of why DDP identifies the particular charging pattern described above, let us focus on the switching pattern exhibited by the optimal solution when charging does occur. Consider the film growth rate for varying SOC and zero current input, as portrayed in Fig. 4.3. For small SOC values, $\dot{\bar{\delta}}_{film}$ is concave. Along this portion of the curve, the total film growth rate for two cells at different SOC values is less than the total film growth rate for two cells at the same SOC value. However, for large SOC values $\dot{\bar{\delta}}_{film}$ is convex. This implies that the total film growth rate for two cells at different SOC values is greater than the total film growth rate for two cells at equal SOC values. If one assumes the solution is infinitely greedy, these observations for reducing film growth can be applied as follows:

1. In the concave region of $\dot{\bar{\delta}}_{film}$, drive the individual SOC values apart.
2. In the convex region of $\dot{\bar{\delta}}_{film}$, equalize the individual SOC values.

In other words, charge each module one-by-one through the concave region and then charge them all simultaneously.

Figure 4.4 DDP-inspired heuristic rule for charging, with optimal state trajectories superimposed.

These results indicate that a reduction in total film growth can be achieved by allowing individual modules to have unequal SOC values - particularly within concave regions of film growth. Additionally, the optimal policy follows a consistent pattern that may be closely approximated by a heuristic feedback control law, which leaves the battery discharged for the maximum allowable time.

4.3.4   DDP-inspired Heuristic Control
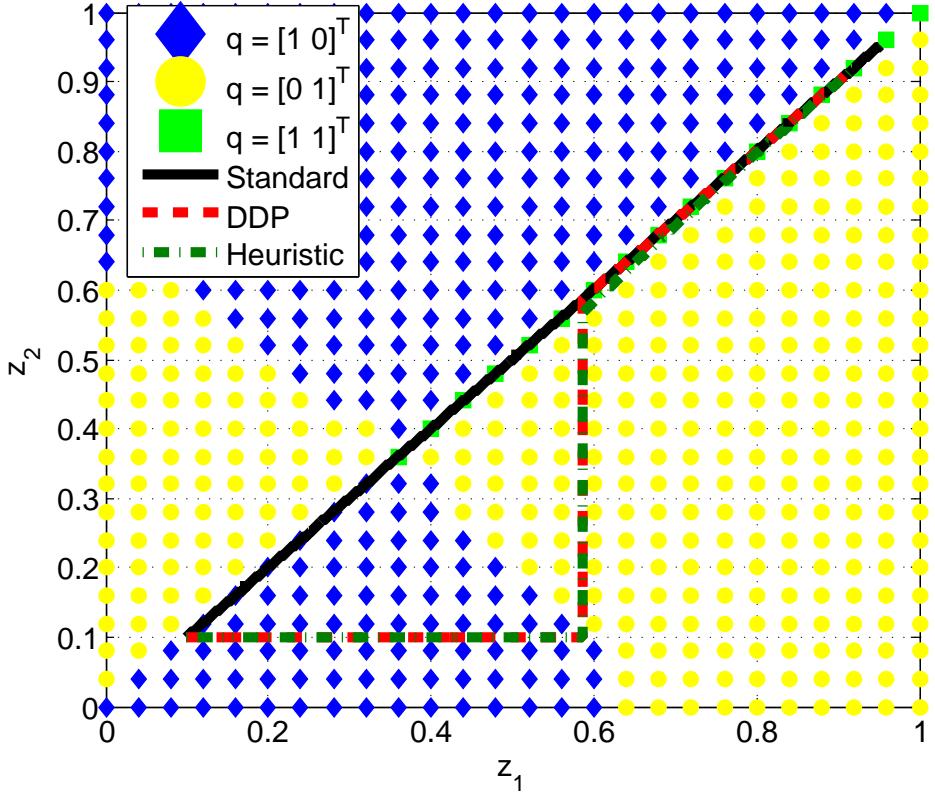
Inspired by these results, and the convexity analysis presented in Section 4.3.3, we examine a heuristic control scheme for minimizing film growth, depicted in Fig. 4.4. The advantage of a heuristic control scheme over the optimal trajectories computed by DDP is that the former can be implemented in a time-invariant feedback loop. Additionally, one expects the heuristic scheme to achieve nearly optimal performance, due to the consistent pattern exhibited by the DDP solutions. The process of converting optimal trajectories into an explicit feedback map has been studied in the context of

DDP [36, 53] and model predictive control theory [151] before. These concepts are potentially applicable here, but a simpler less formal approach is used in this initial study. Note that the switching pattern defined by the heuristic rule should not be initiated until the last possible opportunity. In this example, each cell has a 1.8 A-h charge capacity and thus the total pack charge capacity is 3.6 A-h. Therefore charging both cells from 0.1 SOC to 0.95 SOC at a 1C (1.8 A) rate requires about 100 minutes. As a result, we initiate the heuristic charging scheme 100 minutes prior to the final time.

The design of the heuristic control law follows two steps: First, we simulate the optimal trajectories from a family of initial conditions, such as shown in Fig. 4.2. Second, we identify regions of the state-space corresponding to a certain switch config-uration. For regions in which the optimal state trajectories do not enter, we select a switch configuration that steers the state toward an optimal trajectory. This step is required, because for the 1C charge rate input studied here, feasible trajectories do not cover the entire state-space. The final result of this procedure is depicted in Fig. 4.4, where several optimal state trajectories are superimposed on the proposed heuristic rule. Note how the heuristic controller follows the general guidelines of SOC separation and equalization in the respective concave and convex regions of Fig. 4.3.

4.4   Comparative Analysis and Sensitivity Studies

To evaluate the performance of the proposed heuristic controller, we compare it to the optimal DDP-based and standard equalization schemes (i.e. both switches closed during charging). We perform this study by simulating the closed loop battery pack degradation control system for a 1C (2.3 A) constant current charge rate cycle. This study is performed on both the equivalent circuit model and static map of film growth rate (which was used for optimization, and henceforth is referred to as the "Control" model) and the full electrochemical model. In both cases the initial cell SOC values are 0.1 each. In practice, the standard charge method is to apply constant current to every cell in the pack until the voltage reaches a maximum value, then the voltage is held constant at this maximum value until the applied current reaches some minimal level. This is known as a constant current, constant voltage (CCCV) charge cycle [7]. Here, we only investigate the potential improvements incurred during the period when the cells charge up to a maximum voltage limit, corresponding to 0.95 SOC in our simulations. Subsequently, we report on similar results obtained for constant
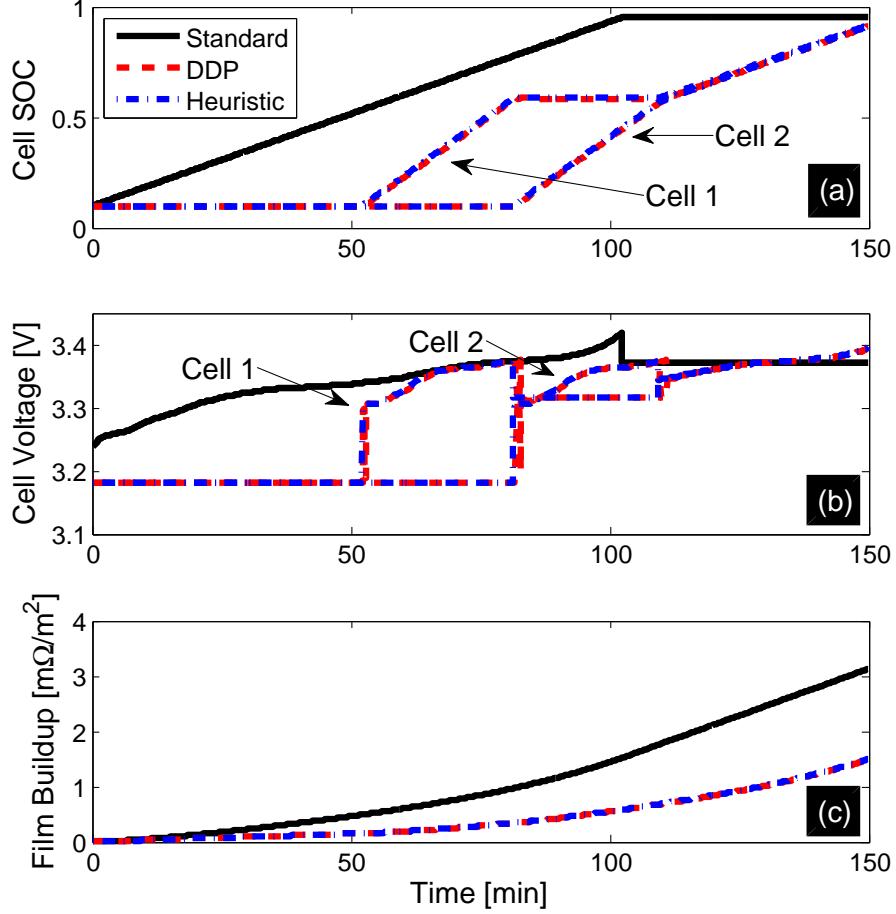
Figure 4.5 SOC trajectories for each control scheme, superimposed on the heuristic control map.

current *discharge* inputs. Finally, we analyze optimal switch patterns for alternative film growth maps, created using different assumption sets or model parameters. The latter analysis is motivated by the fact that accurately modeling aging in lithium batteries is extremely difficult - due to the extensive array of degradation mechanisms and materials within lithium-ion batteries. Regardless of these differences, the link between convexity properties and unbalanced cells remains in our studies.

4.4.1 Control Model Charge Cycle Simulation
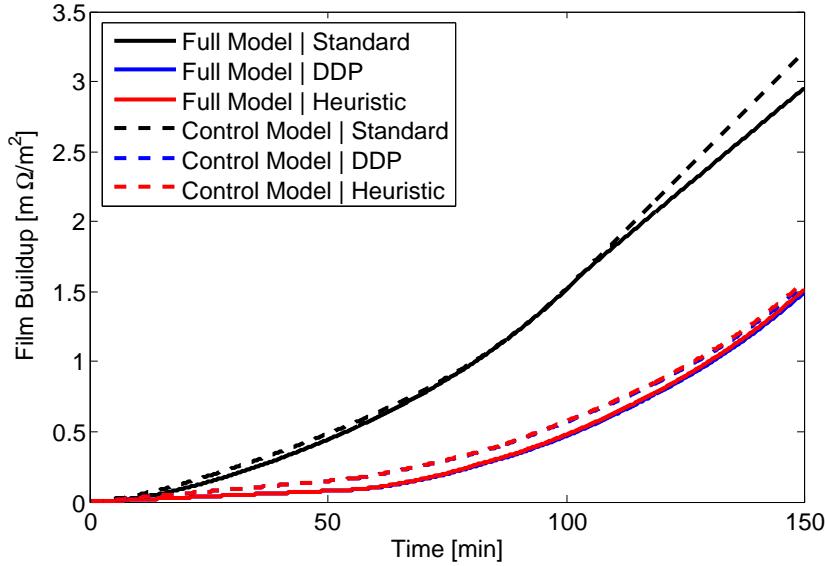
The cell SOC trajectories for each control scheme simulated on the Control model are provided in Fig. 4.5, superimposed on the heuristic rule. Observe that the standard charging scheme maintains each cell at equal SOC values as the battery pack charges. In contrast, the trajectories corresponding to DDP and the heuristic rule follow trajectories similar to Fig. 4.2 and 4.4. Namely, both methods charge one cell at a time in the concave region of $\dot{\bar{\delta}}_{film}$, and then apply charge equalization in the convex

Figure 4.6   Time responses for each control scheme.

region of $\dot{\bar{\delta}}_{film}$. Also observe that trajectories for DDP and the heuristic controller match closely, indicating that the proposed heuristic controller closely approximates the optimal solution for the trajectory shown here.

Time responses for the cell SOC, current, and battery pack voltage are provided in Fig. 4.6. Here we see that the heuristic rule is initiated approximately 50 minutes into the simulation, allowing 100 minutes of charging time. Figure 4.6(a)-(c) further demonstrate how closely the heuristic controller and DDP solution match, with respect to time. Since the standard method initiates charging immediately, the cells remain idle at 0.95 SOC once charging is complete. This is important because film builds up at a faster rate for high SOC relative to low SOC, which is the intuitive reason why delayed charging significantly reduces total film buildup. The impact of this property can be seen in Fig. 4.6(c). Figure 4.6(b) demonstrates each cell's voltage, which increases only when that particular cell is charging. Note that all schemes maintain

Figure 4.7 Film Buildup for each control scheme, simulated on the control model and full electrochemical model.

the cell voltage within the safety range of 2.0V to 3.6V.

4.4.2 Film Buildup Validation on Full Electrochemical Model

To this point, all simulation results have been performed on a reduced equivalent circuit model and static film growth rate map in Fig. 2.6 used for control optimization. In this subsection we study (1) if optimal switching indeed reduces film buildup for a high-fidelity electrochemical battery model, and (2) if the static approximation of film growth reasonably matches the film model prediction. Towards this goal, we apply all three controllers (standard, DDP, and heuristic) on the full electrochemical model (Full).

The aggregated film buildup for the Control and Full models, simulated using each control scheme, are provided in Fig. 4.7. This figure indicates that the DDP and heuristic control schemes indeed reduce film buildup on the full electrochemical model, despite being synthesized for the Control model. Specifically, the open-loop DDP control and closed-loop heuristic controller reduced buildup by 49.5% and 48.7%, respectively. Moreover, the total film growth predicted by the Control model differ from the Full model by less than 10% for all control schemes. Therefore, we conclude that the reduced order model, taking the form of a static nonlinear map, enables the

accurate minimization of film growth for the charge cycles studied here.

4.4.3 Performance Results
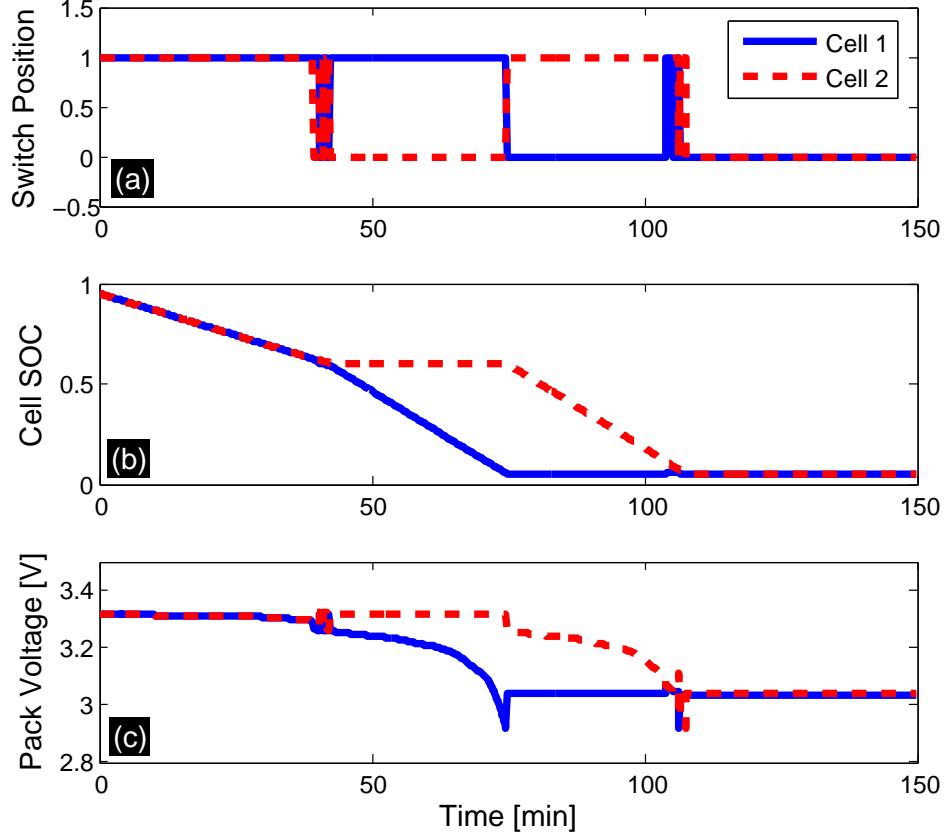
A comparison of the performance for each control scheme is provided in Table 4.1. For the 2.3A rate charge cycle studied in this article, the heuristic controller produces an additional 20 $\mu\Omega/m^2$ (0.8%) of resistive film buildup over the DDP solution on the full electrochemical model. Hence, the heuristic scheme exhibits nearly identical performance to the optimal control design. Both DDP and the heuristic controller reduce film buildup by about 50%, for this charge cycle. It is important to note that the reduction in film buildup is a function of the particular charge cycle and time horizon. That is, cycles that remain within the concave region of $\dot{\bar{\delta}}_{film}$ may experience greater improvement, because the switched scheme proposed in this article has the greatest advantage in this domain. Moreover, the bulk of film reduction occurs due to delaying the charging process to the end of the time horizon. For the example studied here, 48% of film buildup reduction is due to delaying charging until the final 100 minutes.

4.4.4 Optimal Trajectories for Discharge

Throughout this chapter we have considered optimally charging battery cells in parallel with relay switches to minimize total film growth - under charging events only. Here we consider constant current *discharge* events. The problem is formulated exactly as before, except now we apply a 2.3A discharge current input. The optimal switch, SOC, and voltage trajectories are provided in Fig. 4.8, with the battery pack initialized at 95% SOC for each cell. Optimal SOC trajectories for various initial conditions are provided in Fig. 4.9. Under a discharging scenario, these results indicate the optimal constant current discharging trajectories follow a consistent pattern.

1. Discharge the pack immediately. This moves the system away from regions of fast film growth - so less interfacial film accumulates over time.
2. Equalize both cells as they discharge.
3. Continue to discharge both cells at equal charge levels, until a certain point.
4. Discharge each cell individually until the battery pack is fully discharged.

In essence, these discharge trajectories follow the optimal charge trajectories backwards. Moreover, the breakpoint between charge equalization and unequalization is approximately the same - 60% for both cells. Convexity arguments for infinitely greedy trajectory optimization solutions can be applied, once again, to interpret these results.
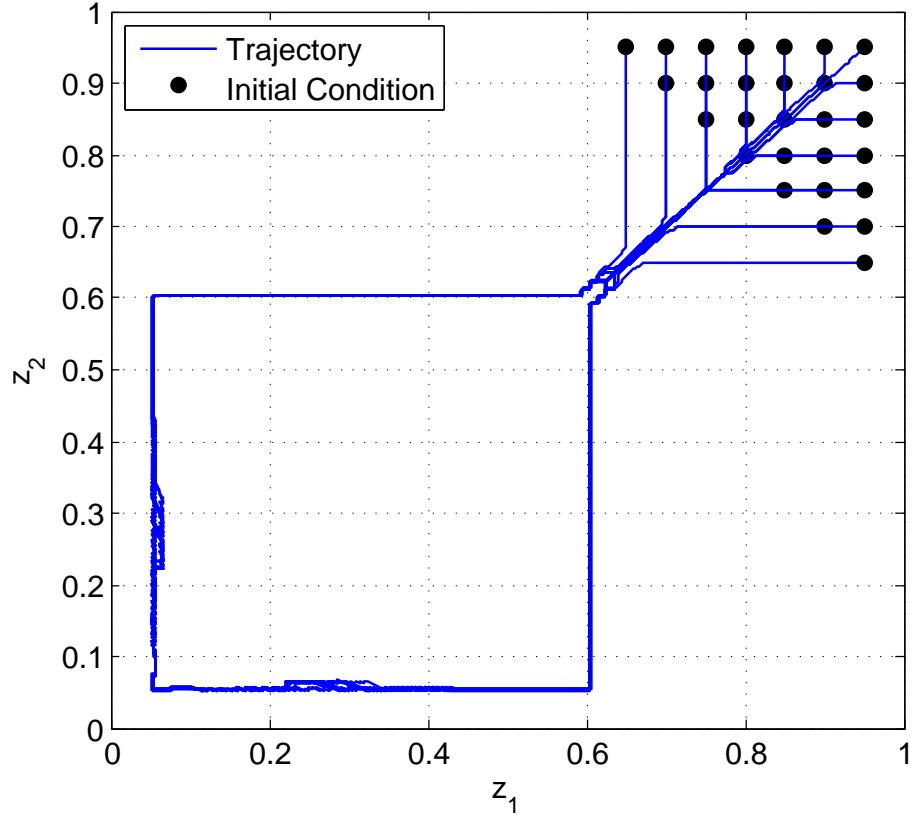
Figure 4.8 Time responses for optimal discharging pattern identified by DDP, given a 1C battery pack discharge rate.

Hence, allowing unequal charge levels in battery management systems may provide long-term health benefits when concavity properties exist in the aging mechanics.

4.4.5 Sensitivity to Alternative Film Growth Parameterizations

Anode-side film growth has been recognized as a significant contributor to lithium-ion battery health degradation [30]. However a plethora of other difficult-to-model aging mechanisms can contribute to capacity and power fade. Moreover, modeling and accurately parameterizing these models across a wide range of lithium-ion cell chemistries and manufacturers can be difficult. This motivates the sensitivity analysis presented here. Specifically, we consider alternative film growth maps to evaluate the generality of unbalanced charging to varying model assumptions and parameterizations.
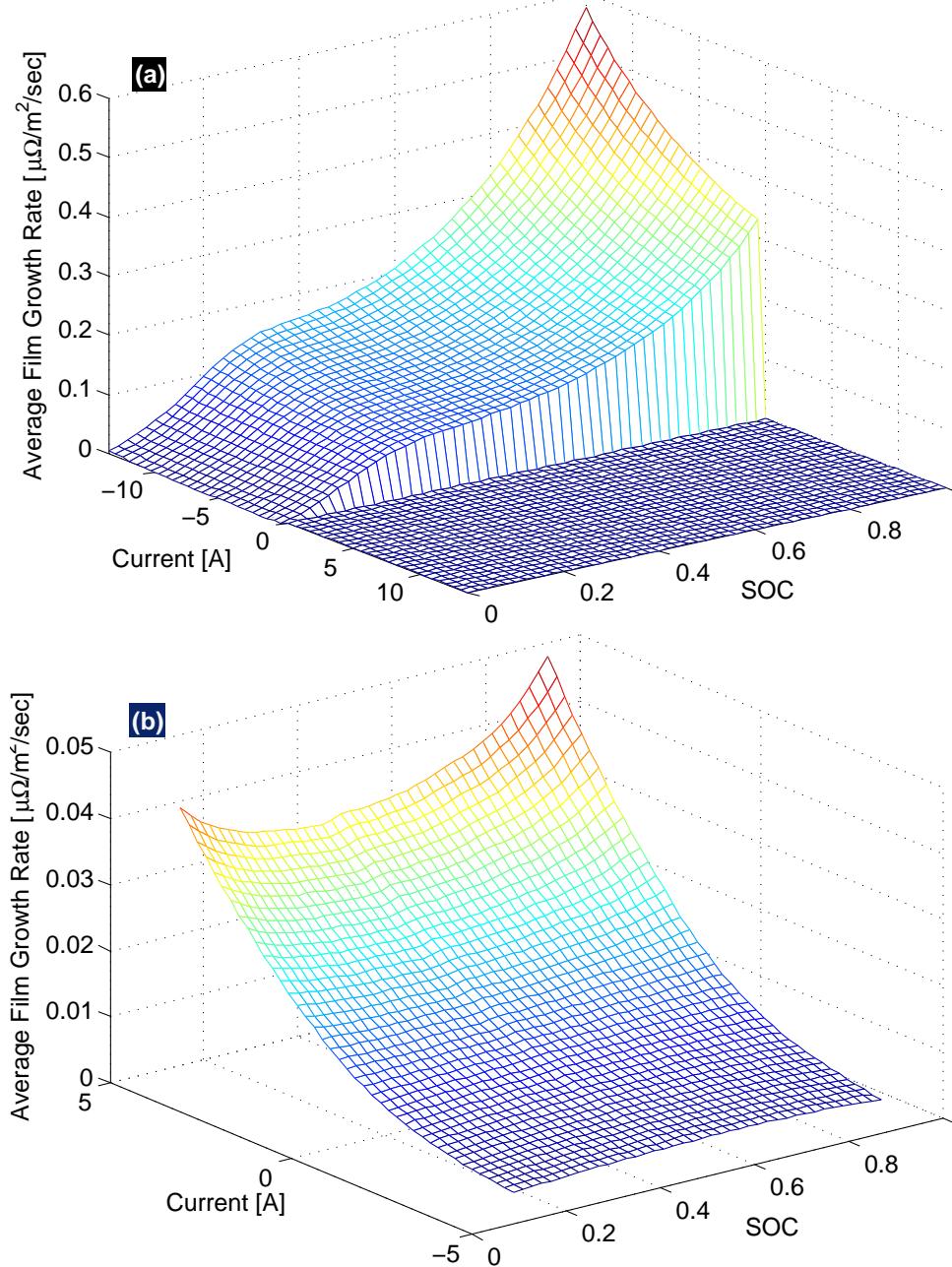
The first map, shown in Fig. 4.10(a), is equivalent to Fig. 2.6 except we enforce

Figure 4.9 Optimal trajectories for various initial conditions, given a 1C battery pack discharge rate.

Assumption 2 of [7] which states that film growth occurs only during charging events, i.e. zero growth during rest and discharge conditions. The optimal charge trajectories for a 1C constant current rate are shown in Fig. 4.11(a). In this case the optimal solution charges each cell individually and in succession. This result can be understood by noting that one cell charged at 1C and the other at rest (no growth) produces less total film growth than two cells charged simultaneously at 0.5C. Also note that although Fig. 4.11(a) shows a delayed charging strategy, delaying charging provides equivalent film growth as immediate charging since zero film growth occurs during rest. Therefore when Assumption 2 of [7] holds true, unbalanced charging provides a 53% reduction in total film growth, which is a greater reduction from unbalanced charging when using the original film growth map.

The second map, shown in Fig. 4.10(b), is based upon the same model equations used for Fig. 2.6 but with an alternative parameter set. This parameter set has been identified to produce capacity fade trends that match the manufacturer's cycling

Figure 4.10 Film growth maps for alternative electrochemical model parameterizations: (a) No film growth occurs during discharge or rest conditions, which follows Assumption 2 of [7]; (b) Preliminary parameterization to match the manufacturer's cycling and storage performance data.

and storage data [150]. The two parameter sets used for each map are provided in Appendix D. The optimal charge trajectories for a 1C constant current rate are shown in Fig. 4.11(b). Unlike the previous two cases the optimal solution does not unequalize

the cells' charge levels. This result can be interpreted through the convexity arguments of Section 4.3.3 by observing that Fig. 4.11(b) contains no concave regions. Thus charge balancing minimizes film growth. However, delayed charging still provides benefits by maximizing the time spent to low SOC levels, where film growth is slow.

4.5 Summary
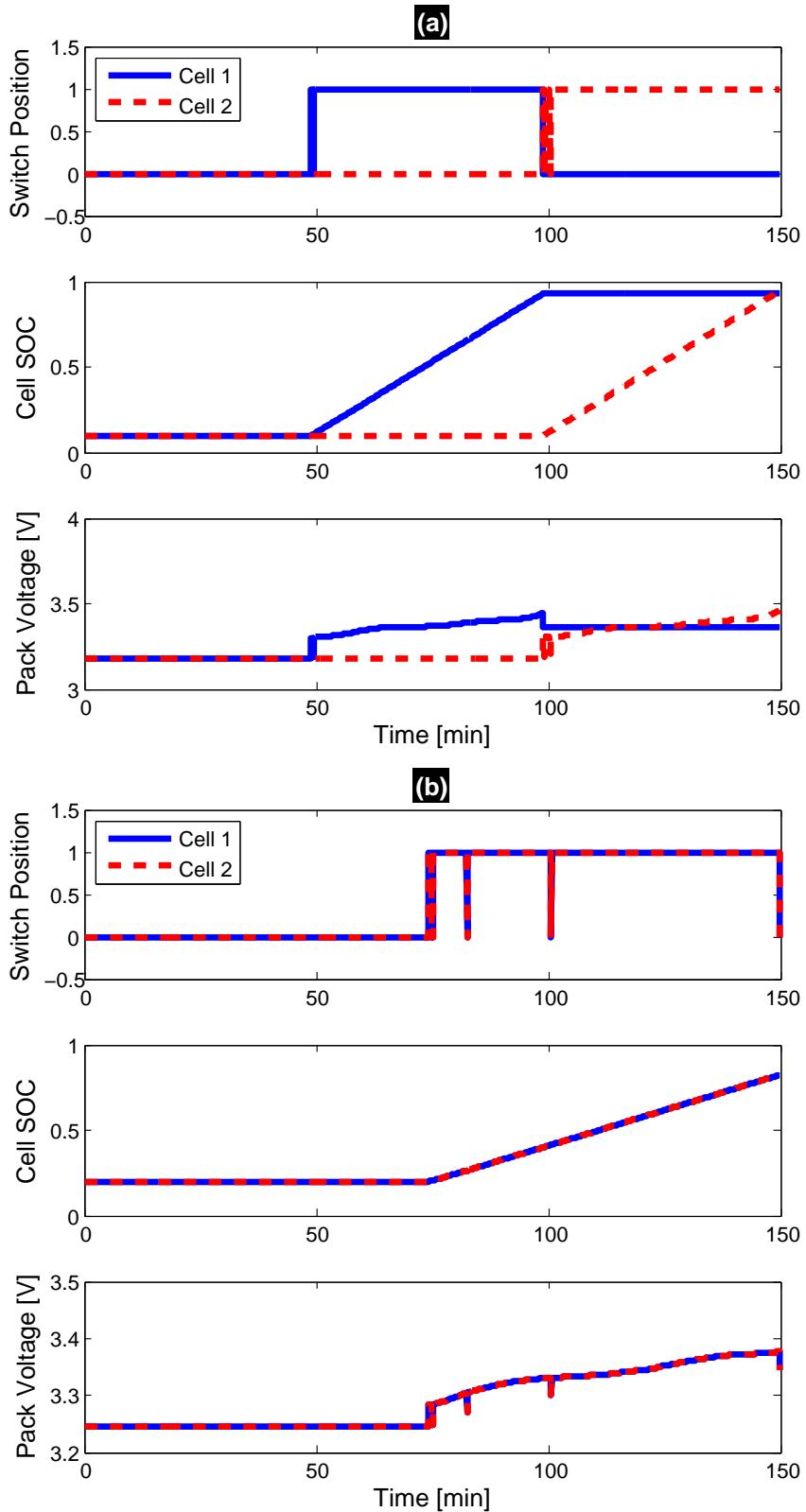
This chapter investigates battery health management in Li-ion battery packs using relay switches for modules connected in parallel. To facilitate control design and analysis, we consider the electrochemical battery cell model with irreversible solvent reduction reaction dynamics at the anode, developed by Ramadass *et. al.* [7] from Chapter 2. From this high fidelity model, we approximate film growth rate as a static map that functionally depends on cell SOC and applied current. Using this map, we formulate an optimal control problem to minimize total battery pack film growth for a constant current charge trajectory. Inspired by the optimal trajectories, and the convexity properties of the film growth map, we design a heuristic rule base that produces nearly optimal performance. Further optimization results for constant current discharge trajectories and alternative film growth models demonstrate the generality of charge unequalization to varying input profiles, model assumptions, and parameterizations.

The key result demonstrated by this work is that health degradation due to film growth can be reduced by: (1) Allowing battery modules connected in parallel to attain unequal SOC values when concavity features exist; and (2) Delaying charging until immediately before discharging. Indeed, the optimal solution approximately separates SOC in the concave region and equalizes SOC in the convex region of film growth rate at the end of the time horizon. This process can be implemented using a heuristic static feedback controller designed from optimal trajectories computed via dynamic programming. Individual control of module SOC is achieved via relay switches typically used for safety precautions. Within each module, individual cell SOC may be equalized via traditional switched capacitor circuits [111, 112] to protect against over-charging or over-discharging. Simulation results indicate this approach may significantly reduce total battery pack film growth, if one can identify concavity features in the degradation performance map. This motivates future work focused in two directions. First, experimentally identifying a data-driven degradation map similar to Fig. 2.6 may enable significant improvements in lithium ion battery lifetime
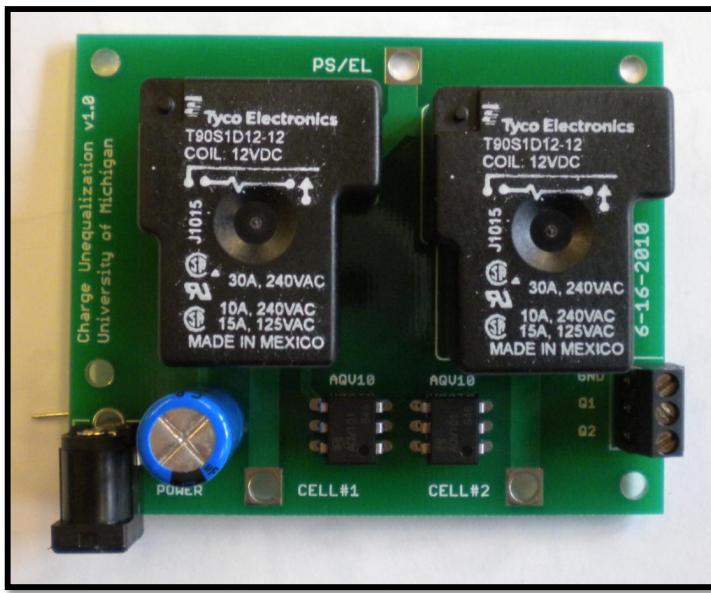
through controlled unequal charging schemes. This effort is currently underway within the laboratory using the multi-channel tester described in Section 2.1.3 and Fig. 2.7. Second, experimental verification of these algorithms designed from data-driven degradation models will provide the ultimate proof-of-concept. Controlled switching equipment has already been designed and fabricated for this purpose, as shown in Fig. 4.12.

Table 4.1 Controller Performance Comparison on Control Model and Full Electrochemical Model.

Control Scheme	Control Model		Full Model		
	Resistance of Total Film Buildup	Reduction in Film Buildup	Resistance of Total Film Buildup	Reduction in Film Buildup	Control vs. Full Error
Standard	3.20 mΩ/m²	0%	2.95 mΩ/m²	0%	8.47%
DDP	1.55 mΩ/m²	51.8%	1.49 mΩ/m²	49.5%	4.03%
Heuristic	1.56 mΩ/m²	51.2%	1.51 mΩ/m²	48.7%	3.31%

Figure 4.11 Time responses of optimal charging trajectories for the alternative film growth maps. (a) Response for map in Fig. 4.10(a). This map suggests charging the battery pack one cell at a time. (b) Response for map in Fig. 4.10(b). This map suggests charge equalization is optimal.

100

Figure 4.12   Printed circuit board of controlled relay switches to test the charge unequal-ization concept.

Chapter 5

Conclusion

5.1   Dissertation Summary

The optimal control and electrochemical modeling framework proposed in this dissertation provides a systematic methodology for formulating, solving, and analyzing power management problems in battery-electric systems. In particular, we apply these techniques to lithium-ion battery pack health in plug-in hybrid electric vehicles (PHEVs). Moreover, the results demonstrate what control opportunities exist in PHEVs, given certain mathematical structural properties in the battery health degradation physics. As a consequence, the proposed algorithms may improve the useful life of battery packs. This is critically important for large-scale battery energy storage systems - ranging from PHEVs to stationary grid-scale storage - where replacement cost, bulk, and cycle life are inhibiting factors associated with the uncertainty in maintaining operation within safe limits.

In Chapter 2, three types of models were presented to study optimal PHEV and battery pack energy management. First, a dynamic model for the mechanical and electrical subsystems of a PHEV drivetrain was presented. These include inertial dynamics of the vehicle, engine, and motor/generators coupled together though a planetary gear set in a power-split configuration. Second, a Markov chain model for drive cycle dynamics was presented. This model has a special feature useful for capturing the distribution of daily trip lengths - namely a terminal state associated with "vehicle off". Finally, a detailed electrochemistry-based battery cell model was presented. This model captures Li-ion diffusion dynamics, intercalation kinetics, and electrode thermodynamics. This chapter also presents two important types of battery health degradation models: a physics-based solid electrolyte interphase (SEI) layer film growth model and an empirically-based "Ah processed" model. Together these models constitute the essential elements for studying supervisory control in PHEVs

and battery pack charge management.

Chapter 3 investigates supervisory control algorithms that manage the tradeoff between battery pack health and energy consumption cost in plug-in hybrid electric vehicles (PHEVs). This study leverages both stochastic control theory and reduced electrochemical battery models to achieve its goal. First, a multiobjective stochastic control problem is formulated and solved via stochastic dynamic programming techniques. To contextualize the multiobjective battery-health conscious results, we first analyze the single objective control results which consider energy consumption cost only. This analysis describes the underlying advantages of a blended strategy versus charge depletion, charge sustenance. A sensitivity analysis is then performed to understand the impact of variations in battery pack size, daily trip length, and fuel/electricity price. Next we consider battery-health conscious power management control algorithms to minimize two quantitative metrics of capacity fade: SEI layer film growth and Ah processed. Control results for SEI layer film growth model quickly deplete battery SOC to escape the regions of fast film growth. Control results for the Ah-processed model are extremely tentative to consume battery energy, and therefore rely more heavily on engine power.

Chapter 4 introduces a novel concept in the arena of battery management systems - charge unequalization. Specifically, this chapter analyzes the potential health advantages of allowing unequal yet controlled charge levels across batteries connected in parallel. Towards this goal, we consider two cells connected in parallel in which charge levels are controlled via relay switches. The control problem is then to determine the optimal sequence of switch configurations which minimize the total battery pack SEI layer film growth. In general the optimal solutions unequalize SOC at low values and equalize SOCH at high values. This result is directly related to the convexity properties of SEI layer film growth. To analyze the impact of variations in the battery health model, we consider two alternative SOH degradation models. Ultimately, we find the existence of concavity in the SOH model is what leads directly to charge unequalization.

In summary, the research reported in this dissertation advances knowledge on managing power and energy flow in energy storage and conversion systems by combining optimal control and electrochemical battery models, for this first time. This dissertation has demonstrated this is critically important for enhancing the useful battery lifetime, replacement costs, and power efficiency in energy storage systems. In particular, these developments take steps towards increasing the wide-spread adoption of lithium-ion batteries for systems in which energy storage is the linchpin enabling

technology.

5.2   Summary of Contributions

This dissertation provides four distinct and original contributions toward optimal energy management control for Li-ion battery health in PHEVs.

1. A coupled PHEV powertrain and electrochemistry-based Li-ion battery model was presented for supervisory control design studies. Although this model is generally too complex for solving optimal control, it provides a high fidelity platform to test and analyze controllers based upon reduced order models. An experimental battery-in-the-loop test system was also developed to identify the parameters of the battery model. (Chapter 2)

2. A multi-objective stochastic optimal control approach was presented for studying the tradeoffs between energy consumption cost and battery health. This problem formulation utilizes the PHEV drivetrain model, the stochastic drive cycle model, and reduced-order battery models which include various SOH degradation metrics (i.e. SEI layer growth and Ah-processed). Mathematically, the problem is solved as a shortest-path stochastic dynamic program. Nonetheless, the framework is general and application to many scenarios characterized by multiple objectives, stochastic processes, and various levels of model complexity. (Chapter 3)

3. A novel charge unequalization concept for battery pack management systems was proposed, designed, and analyzed. This concept explores the battery health benefits of allowing unequal yet controlled charge levels in batteries connected in parallel via relay switches. This concept is also generalizable to heterogeneous groups of batteries and more advanced interface topologies. (Chapter 4)

4. Opportunities for novel control techniques were identified given certain mathematical structural properties in the battery degradation physics (i.e. slope and convexity). Clearly, these properties vary depending on the battery chemistry, mechanical design, manufacturing process, environmental conditions, operating scenarios, etc. The critical contribution of this thesis is to understand which properties are important to identify for enabling opportunities that enhance battery health through control. (Chapters 3 and 4)

5.3 Perspectives on Future Extensions

The proposed control problem formulations and resulting algorithms make notable steps towards developing PHEVs with enhanced lithium-ion battery lifetime. Nonetheless, there exist several opportunities to advance the work presented here. These are presented in three categories (modeling, power management, and battery management) described below.

5.3.1 Electrochemical Modeling

Temperature[152, 92, 94] and intercalation-induced stress [26] have critical impacts on the capacity and power fading characteristics of lithium-ion batteries. Several recent studies have constructed coupled thermo-electrochemical [153, 154] and mechanical-electrochemical [26, 27, 155] models. Similar modeling efforts could be utilized in the battery-health conscious power management framework considered here.

Opportunities exist for improved model reduction techniques for the PDAE-based electrochemical model. In particular, control-oriented "proper" models which balance predictive ability and simplicity are desired [156]. Towards this goal, there exists a burgeoning body of research on electrochemical battery model reduction. These techniques include the single particle model [157], residue grouping [65], modal expansions [158, 159, 160], volume averaging [158, 159, 67], constant electrolyte concentrations [67], proper orthogonal decomposition [161], electrode averaged models [162, 163], quasi-linearization and Padé approximations [99]. Nonetheless, these models are not completely commensurate with the broad spectrum of control design problems, thus motivating further research.

5.3.2 Optimal Power Management

Opportunities exist for improvements in the dynamic programming formulation. These include true multi-objective DP [128, 164], two-time scale DP [165, 166], and adaptive algorithms. These improvements are especially relevant toward power management of energy conversion systems where multiple objectives (e.g. energy consumption, battery health) and dynamic time scales (battery SOC, battery degradation) are present.

Another interesting extension might provide a more thorough investigation of the interaction between control and design. Theoretical [167, 168] and applied approaches [169] provide interesting pathways. Moreover, the framework provided in this dis-

sertation would be generally applicable to alternative hybrid design configurations, such as series hydraulic [117], parallel [37], series-parallel [48, 44], and output-split architectures [170].

Ultimately, PHEVs will interact with the electric grid while plugged in. Analysis, design, and control of the dynamic coupling between PHEVs and electric power systems remains a relatively open research question [171, 82, 83, 172, 173].

5.3.3 Battery Management

In theory, the switching control concept for unequal charging proposed in this dissertation may mitigate the SEI layer film growth. It would be of great interest to demonstrate this result experimentally, using the battery-in-the-loop hardware presented in Appendix A for example. Extensions of this concept might also consider more advanced power electronics topologies [174, 175] and adaptive algorithms.

The battery management control algorithms considered in this work limit their scope outside of state/parameter estimation [149]. A future direction might consider output-feedback algorithms using recently developed control and estimation theory for linear parabolic PDEs [84, 176, 177].

Appendices

Appendix A

Fabrication of an Experimental Battery-in-the-Loop Test System
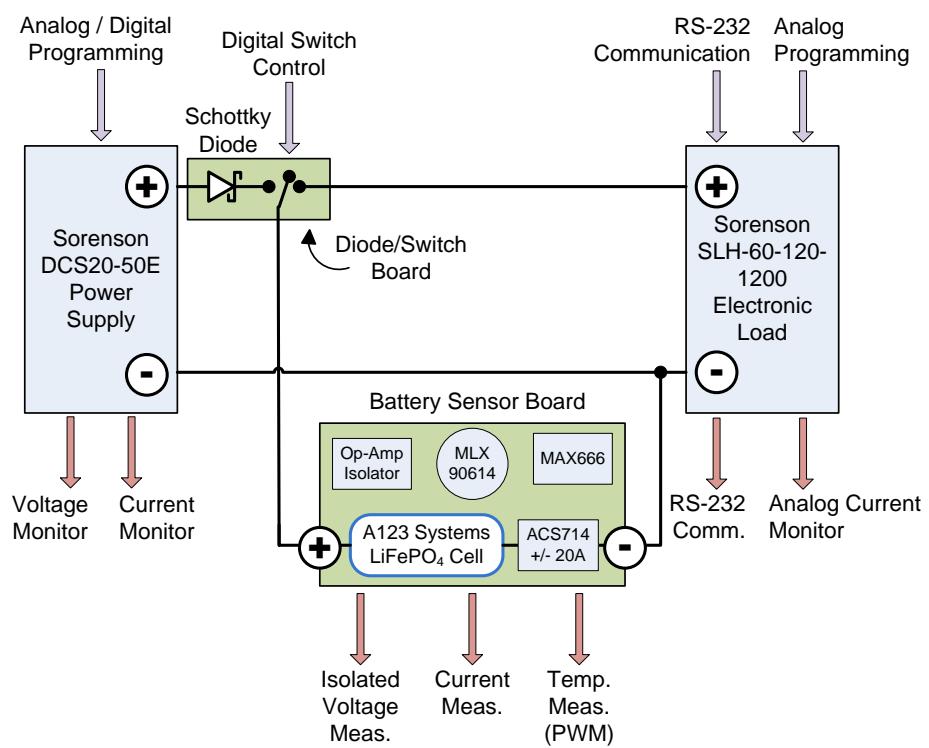
Experimental data has been collected using a custom built battery tester. This tester is capable of highly transient current/voltage profiles and quickly switching between charging and discharging. These characteristics make it ideal for testing batteries under conditions similar to those experienced in PHEV battery packs. Additionally, this setup is capable of Hardware-In-the-Loop (HIL) experimentation which will be advantageous for future battery control and estimation studies [178].

This battery tester is a combination of three major components: an electric load (SLH-60-120-1200), a power supply (DCS20-50E), and a Real-Time (RT) controller and I/O board (DS1104). A photo of the battery tester was shown in Fig. 2.5. Figure A.1 is a schematic of the setup where all signal lines are connected to the I/O board. The power supply and electric load handle battery charging and discharging respectively. The RT I/O board coordinates the electric load, power supply and switching board. In addition, the RT I/O board records sensor signals including voltage, current, and temperature, obtained from a custom built battery sensor board shown in Fig. A.2. The battery sensor board measures battery voltage through a voltage isolating differential op-amp and battery current via a bi-directional 20A Hall effect sensor (ACS714). An infrared thermopile (MLX90614) measures temperature. An electrical schematic and PCB layout of this board designed in EAGLE are shown in Fig. and , respectively. The switch board switches the setup between charging and discharging by swapping the battery's connection between the supply and load. A photo of this switch board is shown in Fig. A.5. The Schottky diode protects the power supply from absorbing battery energy. Using printed circuit boards (PCBs) has greatly improved the reliability and accuracy of the sensor electronics and switch/diode combination. A variety of signals interface the battery tester's components, including: analog, basic digital, PWM, SMBus, RS-232, and TTL. A list of the main components,
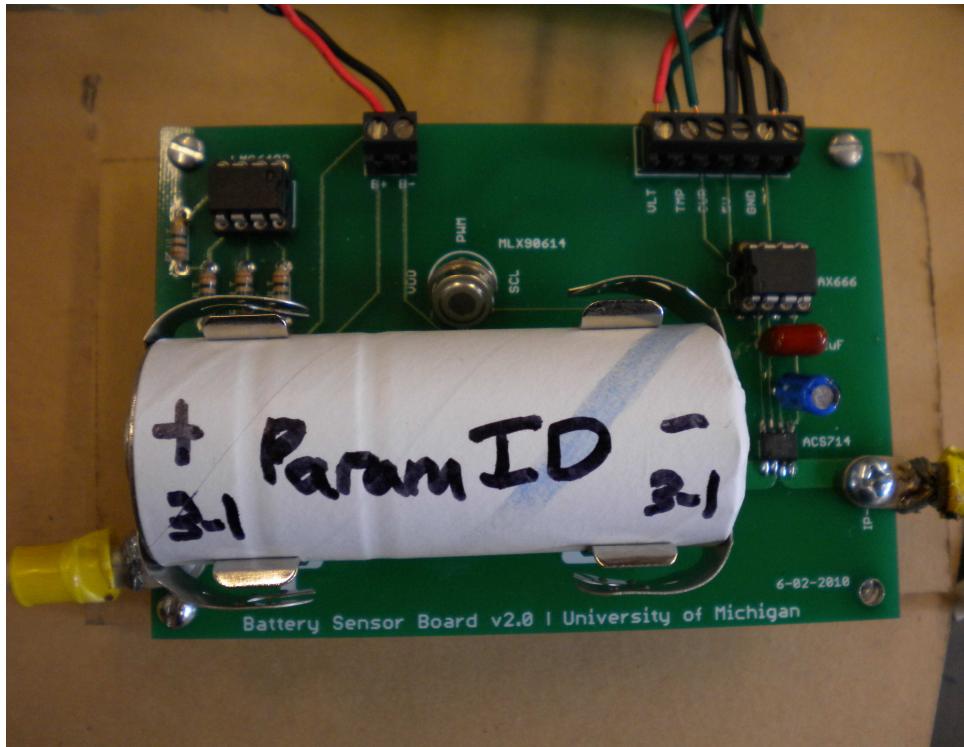
their manufacturers/model numbers, and general features are provided in Table A.1

Table A.1   Components of the Battery-in-the-Loop Tester
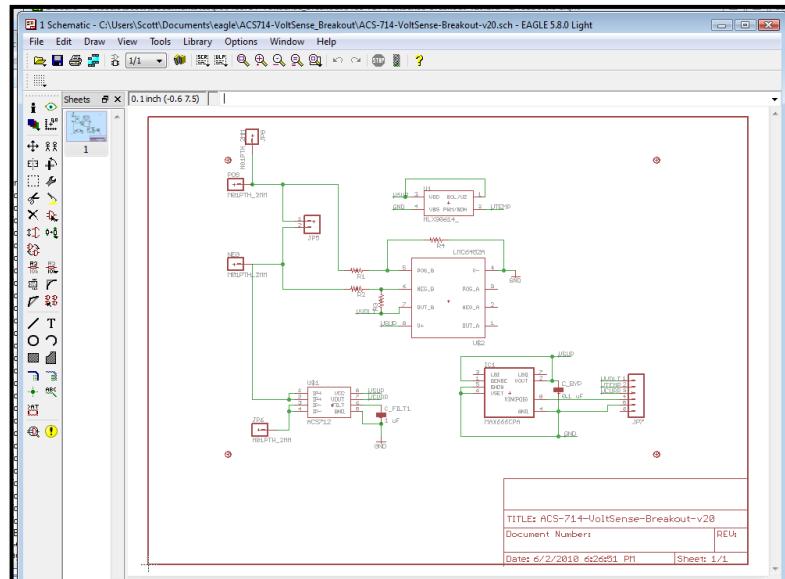
Component	Manufacturer/Model	General Features
Li-ion Battery Cells	A123 Systems ANR26650M1A	2.3 Ah, 3.3V nominal voltage, 70C max. continuous discharge
Power Supply (PS)	Sorenson DSC20-50E	0-20V, 0-50A range
Electronic Load (EL)	Sorenson SLH-60-120-1200	0-60V, 0-120A, 1.2 kW range
Real-time control and measurement	dSPACE DS1104	PowerPC 603e CPU, 32 MB SDRAM, PCI interface, 8 ch. 16/12-bit ADC, 8 ch. 16-bit DAC, Digital I/O, Serial
Voltage sensor	Custom-built voltage isolating differential op-amp	0-5V range
Current sensor	Allegro Microsystems ACS714	$\pm$ 20A range
Temperature sensor	Melexis MLX90614 Infrared thermopile	-40°C to 85°C
Voltage regulator	Maxim MAX666	5V output, 2V-18V input
PS blocking diode	S60HC3 Schottky Barrier Diode	60A forward current, 30V reverse voltage
PS-to-EL Relay	Panasonic CB1-P-12V	12 VDC power, 30A load
Switch for PS-to-EL Relay	Panasonic AQV101 Optical Relay	700mA load, 50mA LED current
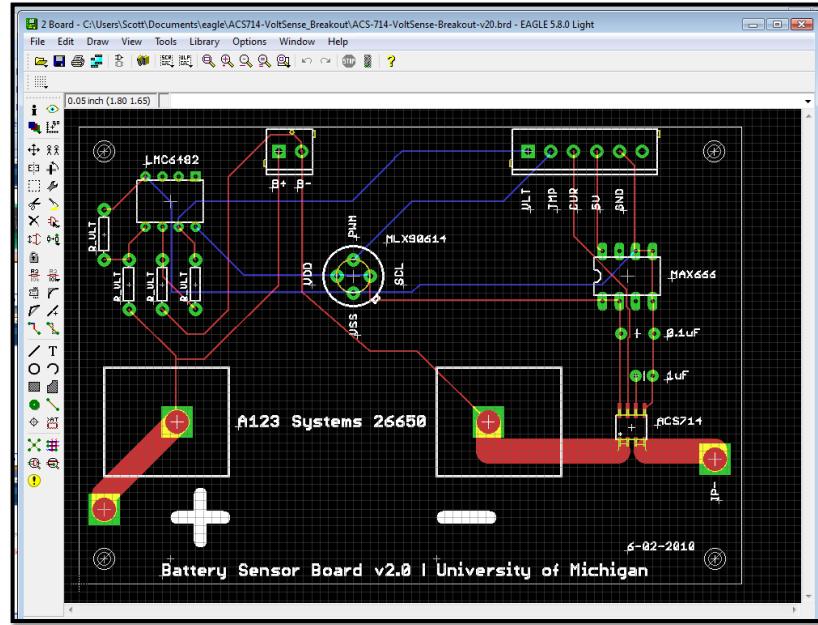
Figure A.1   Schematic of battery-in-the-loop hardware configuration.
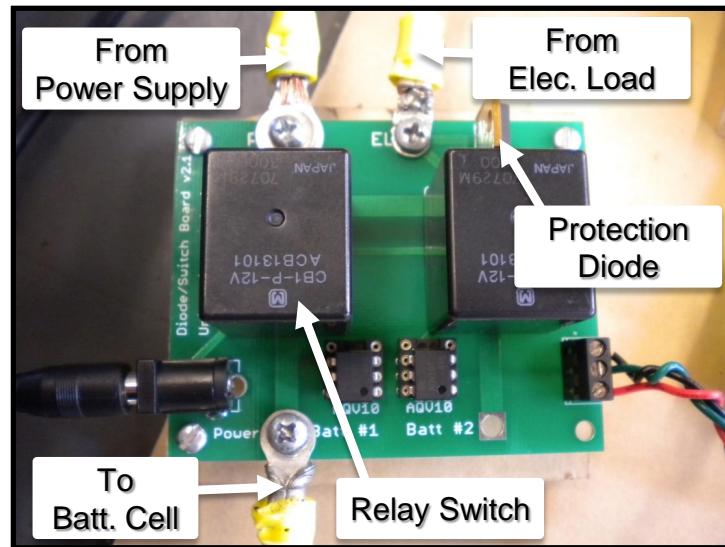
Figure A.2 Custom designed battery cell sensor board. Components include an A123 Systems 26650 2.3Ah cell, an isolated voltage sensor, a 20A current sensor, and infrared temperature sensor.

Figure A.3 Circuit schematic of battery cell sensor board created in EAGLE.

Figure A.4 Board layout of battery cell sensor board created in EAGLE.

Figure A.5 Custom designed switch/diode board used to switch between the power supply and electronic load. The Schottkey diode blocks current from flowing into the power supply.
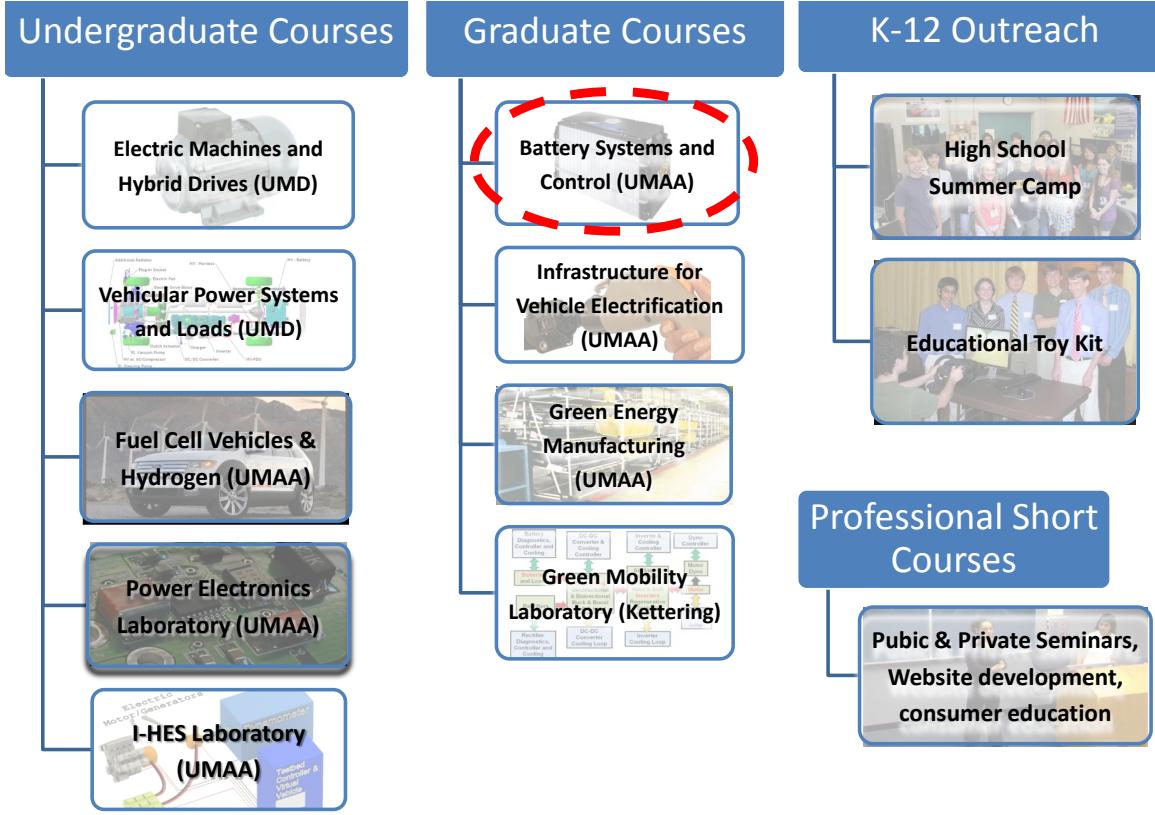
Appendix B

ME 499/599: Battery Systems and Control

This appendix describes a new course on battery systems and control (ME 499/599). This course has served as a vehicle to disseminate knowledge obtained from this dissertation to the community - a unique feature of any doctoral research project. The objective is to provide to undergraduate, graduate, and professional students the technical skills necessary for developing a new generation of green vehicle technology. Emphasis is placed upon systems-level modeling, design, and control, oriented towards solving issues relevant for new vehicle development. The battery course specifically focuses on system-level modeling, model order reduction from electrochemical models to surrogate models for load control, estimation, on-board identification and diagnostics for lithium-ion batteries. Ultimately this course aims to transform the automotive industry's workforce into the leading experts on vehicle electrification technologies.

This course is a single component of a much broader educational program funded by a 2.5 million USD grant from the America Recovery and Reinvestment Act (ARRA) [11], supported through the Department of Energy. This program is entitled "Transportation Electrification Education Partnership for Green Jobs and Sustainable Mobility". Three universities within the state of Michigan are involved: the University of Michigan - Ann Arbor, the University of Michigan - Dearborn, and Kettering University. The project scope is to educate the next generation of engineers and workers and develop an outreach program in electrified transportation. An overview of the course and laboratory hierarchy within this program is provided in Fig. B.1. The program's scope spans vertically across educational levels (K-12 to professionals) and horizontally across academic disciplines (e.g. electric machines to green manufacturing). The battery systems and control course represents one course within this larger effort.

The course enrollment numbers for the Winter 2010 and Winter 2011 terms are

Figure B.1 Hierarchy of DOE ARRA Green Vehicle Technologies Educational Program.

summarized in Table B.1. The on-campus students include undergraduates (ME 499) and graduate students (ME 599) from a wide variety of academic backgrounds such as mechanical engineering, chemical engineering, energy systems engineering, physics, electrical engineering, computer science, materials science, and mathematics). The off-campus students are generally working professionals in industry from organizations such as General Motors, Tesla Motors, Roush, Denso Corp., General Dynamics, U.S. Army TARDEC, etc. The breadth of backgrounds and experience demonstrates the broad impact of this course.

Table B.1 Course Enrollment to date.

Term	On-campus	Off-campus	Total
Winter 2010	54	5	59
Winter 2011	24	26	50

The outline of this appendix is as follows: In Section B.1 we discuss the course's primary goals and desired outcomes. In Section B.2 we provide an overview of the covered topics. Section B.3 describes some example homework problems, including

state-of-charge estimation and charge balancing control, to illustrate the course content. Finally Section B.4 summarizes the course objectives and planned improvements. A portion of the material presented here is based upon a previously published conference paper written by the course instructors [85].

B.1   Course Goals and Outcomes

Course Statement

This course covers battery modeling, control and diagnostic methodologies associated with battery electric and battery hybrid electric vehicles. Emphasis is placed upon system-level modeling, model order reduction from micro-scale to macro-scale and surrogate models for load control, estimation, on-board identification and diagnostics for Lithium Ion batteries. The electrochemical, electrical, and transport principles for battery modeling are reviewed. Spatiotemporal models of coupled concentration, potential, and thermal phenomena are introduced. Simulation of the resulting partial differential equations using software tools will be introduced with selected topics on numerical issues. Model order reduction techniques, parameter estimation, filtering, and control theory will be covered and applied to state of charge estimation. Additionally, electric-circuit battery models, DC/DC converters, and other vehicle implementation issues of power management and balancing will be introduced.

Desired Outcomes

The desired course outcomes are constructed to align with the various levels of Bloom's Taxonomy [179] as follows:

   Knowledge: Students will be able to identify high-level technical challenges related to battery systems, especially as applied to vehicle electrification.

   Comprehension: Students will be able to distill high-level challenges into technical, solvable engineering problems through strong fundamental understanding of battery systems.

   Application: Students will be able to apply their fundamental knowledge about battery physics and control systems to solve concrete problems.

   Analysis: Students will be able to analyze and model battery systems via theoretical electrochemical physics and experimental characterization techniques.

Synthesis: Students will be able to formulate and design control algorithms to manage battery systems. These include state-of-charge estimation, thermal management, hybrid vehicle power-split control between engine and battery power, etc.

Evaluation: Students will be able to evaluate their models and control systems through simulation-based and experimental-based investigations.

Further detail on the course goals and outcomes is included in the ABET course profile provided in Fig. B.7 at the end of this appendix.

B.2 Course Topics

An outline of course topics is provided in Table B.2. The pedagogical approach throughout this course is to (1) examine high-level technical challenges and applications, (2) focus in on fundamental tools and theory necessary to solve specific problems, and (3) allow students to exercise these tools on practical issues through application driven homework assignments and projects. In the following discussion we provide an overview of each chapter's content.

B.2.1 Introductory Material

The course opens with a broad overview of global issues associated with energy storage. These include the spatial mismatch between resources and demand, and the intermittency of renewable energy. The performance characteristics of batteries are placed in context with other energy storage & conversion devices by their specific power and energy density, as demonstrated by the Ragone plot in Fig. B.2. The sloped lines indicate the relative time required to extract and/or store energy from the device. This figure demonstrates that batteries and have high theoretical specific energy, but lower power density when compared to conventional internal combustion (IC) engines. For this reason, batteries are often combined with high specific power devices to form "hybrid" vehicle propulsion systems that achieve the desirable power characteristics. Batteries, by themselves, also encompass a broad range of energy and power densities depending on their chemistry (e.g. lead acid, Ni-Cd, NiMH, Li-ion, Li-ion polymer) and cell packaging (pouch, cylindrical, prismatic).

Several fundamental topics are also introduced to provide the necessary foundation for future course material. These include Kirchhoff's voltage and current laws, battery test procedures (e.g. constant current, constant voltage, impedance measurements,

Table B.2 Outline of Course Topics

Chapter 1: Introduction
- Overview of chemistries, technologies, and challenges
- Kirchhoff's Laws
- Equivalent circuit models
- Test methods and parameter identification

Chapter 2: Physics-Based Models
- Material properties and electrode thermodynamics
- Butler-Volmer kinetics
- Diffusion and electric potential
- Numerical techniques
- Model Reduction
    - Single particle model
    - Padè Approximations
    - Quasi-linearization
    - Projections onto Legendrè polynomials

Chapter 3: Battery Management Systems
- State of charge estimation
    - Coulomb counting
    - Estimation theory
    - Kalman filters
- State of health estimation
    - Overview of degradation mechanisms
    - Electrochemical impedance spectroscopy
- Charge balancing
    - Passive techniques
    - Active balancing
- Thermal dynamics and models
- Thermal management
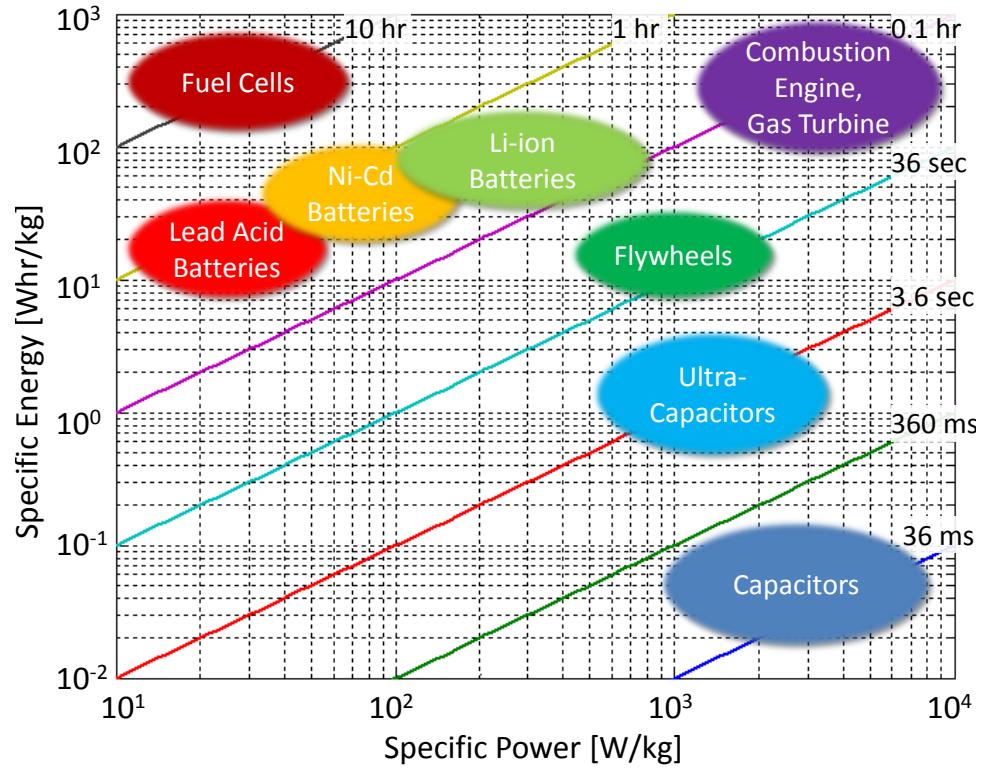
Chapter 4: Vehicle Power Management
- Electric architectures
- Hybrid vehicle power management
- Interaction between electrified transportation and power grids

---
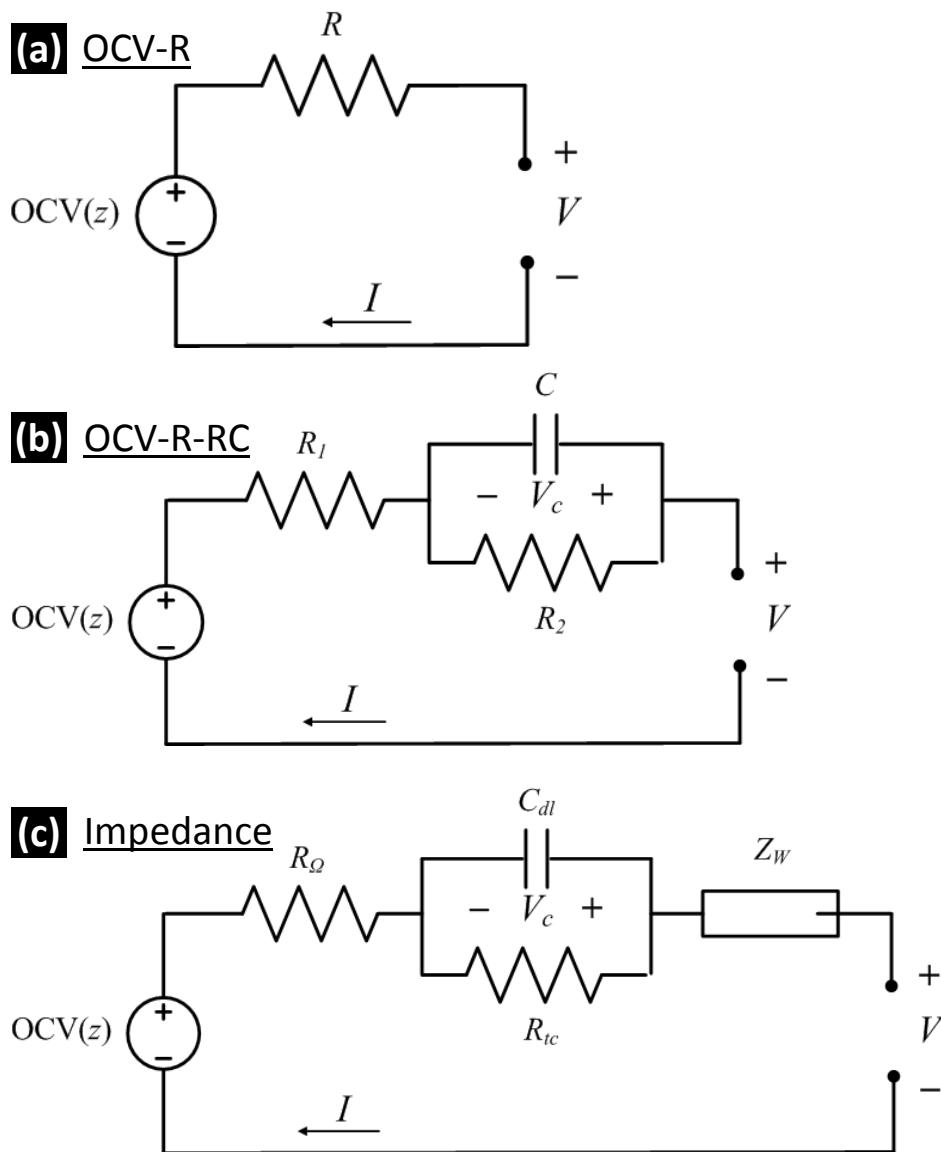
capacity tests, pulse tests), and parameter identification techniques (e.g. least squares). All of these tools will return within the context of upcoming course material.

Next, we introduce the simplest category of mathematical battery models - equiva-

Figure B.2 Ragone plot of various energy storage/propulsion devices and their "charge" times. Adapted from US Defense Logistics Agency Report [8].

lent circuits. These models seek to capture the salient physical phenomena through representative electric circuit elements. Examples include the OCV-R, OCV-R-RC, and impedance model, depicted in Fig. B.3. The OCV element is a variable voltage source whose value depends on cell SOC. It represents the equilibrium voltage of a battery at various charge levels. The R element represents the internal resistance, and can be a function of SOC and current direction. The RC element captures the relaxation effect. That is, immediately following a charge/discharge event one sees the terminal voltage slowly fall/raise as concentration gradients slowly reach equilibrium. The RC element produces the same behavior. The impedance model separates dynamic phenomena by their frequency range. For example, a resistor in series R_Ω typically captures the electrolyte and current collector resistance. An $R_{ct}C_{dl}$-pair represents the charge-transfer dynamics which occur at the solid particle surface. Finally, a Warburg element Z_W models semi-infinite linear diffusion. Its properties include a constant phase of 45°. In total, these models represent the simplest category of battery models. Their simplicity is a key advantage, as it easily facilitates analysis and control design. However, the model parameters are non-physical and difficult to generalize to other

Figure B.3 Various equivalent circuit models: (a) OCV-R, (b) OCV-R-RC, (c) Impedance-based.

chemistries.

B.2.2   Physics-Based Models
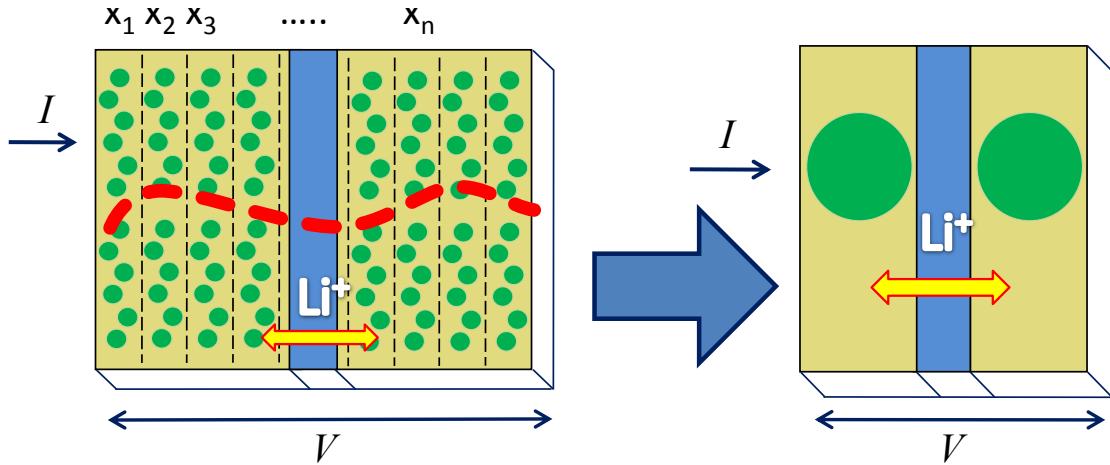
Mathematical models of electrochemical propulsion devices span a spectrum - from high-fidelity physics-based models to simplified phenomenological models. The appropriate balance between model accuracy and simplicity depends on the specific

modeling objective. For example, if one desires to design improved material structural properties for a battery or fuel cell electrode, it may be important to account for particle-level mechanical stresses and electrochemical kinetics. However, if the aim is to analyze life cycle carbon footprints, then a relatively simple phenomenological model may suffice.

In the introductory material, we introduced equivalent circuit models which are phenomenological in nature. In this chapter, we focus on physics-based models. This material is strongly based upon Section 2.1 of this dissertation. Specifically, we discuss how material properties can be used to calculate theoretic cell voltage, charge capacities, and energy densities. Next we focus on deriving the Butler-Volmer equation through the fundamental kinetic principles of reduction-oxidation reactions. The next topic covers diffusion, in both spherical and Cartesian coordinates, and electric potential manifested by distributed form versions of Ohm's law. To unify these principles, we demonstrate how all these phenomena integrate to form a complete electrochemical battery model.

In total the physics-based battery model is a coupled set of partial differential algebraic equations, where the controllable inputs and measurable outputs are represented by boundary conditions. This model is well-suited toward high accuracy simulation and validation. However, this model is not easily implementable on a real-time on-board electronic control unit for automotive applications. As such, we introduce the students to approximation methods that preserve important system dynamics while eliminating unnecessary complexity within the context of the control objective. This process, known as model reduction, is fundamental to almost all practical system-level modeling and control problems.

Several battery model reduction techniques are discussed in the class, including the single particle model [163], Padé approximations, constraint linearization [180], and projections onto Legendre polynomials. For several assignments we consider the following example: Suppose our battery system does not experience extreme charge/discharge loads such that the concentration distributions along the length of the electrodes and separator remain fairly constant. In this case, it may be reasonable to approximate the spatial distributions by their average values. This produces the so-called single particle model shown schematically in Fig. B.4. The reduced model equations that result after applying this concept produce a state-space system with linear dynamics and a nonlinear output equation. The linear dynamics correspond to spherical diffusion in the solid material of the electrodes. The output equation computes cell voltage, which is nonlinear due to the thermodynamic and kinetic

Figure B.4 Conceptual description of the single particle model, which approximates each electrode as a single porous particle immersed in a zero-dimensional electrolyte.

properties of the battery. The structure of this reduced model is extremely appealing for control applications, rendering it amenable to a vast range of control and estimator design techniques. In Section B.3 we describe how students utilize this model to design a Kalman filter for SOC estimation.

B.2.3 Battery Management Systems

This chapter focuses on cell and pack-level control systems. These control systems include state of charge estimation, state of health estimation, charge balancing, and thermal management. During the lectures we introduce the problem background and fundamental tools required to design each control system. Students then apply this knowledge in the homework assignments. The results of Chapter 4 provide a portion of this section's content.

The state of charge estimation problem is introduced and contextualized against various applications (e.g. hybrid vehicles, plug-in vehicles, space vehicles, etc.). We discuss the various categories of estimation methods, including coulomb counting, voltage inversion, impedance measurements, and Kalman filters. In particular, we focus attention to Kalman filter estimation theory and its application to the single particle model discussed above. Homework problems are assigned to progressively build the single particle SOC estimation scheme and explore Kalman filters, as described in Section B.3.

Next we cover state of health (SOH) estimation. First, we provide an overview
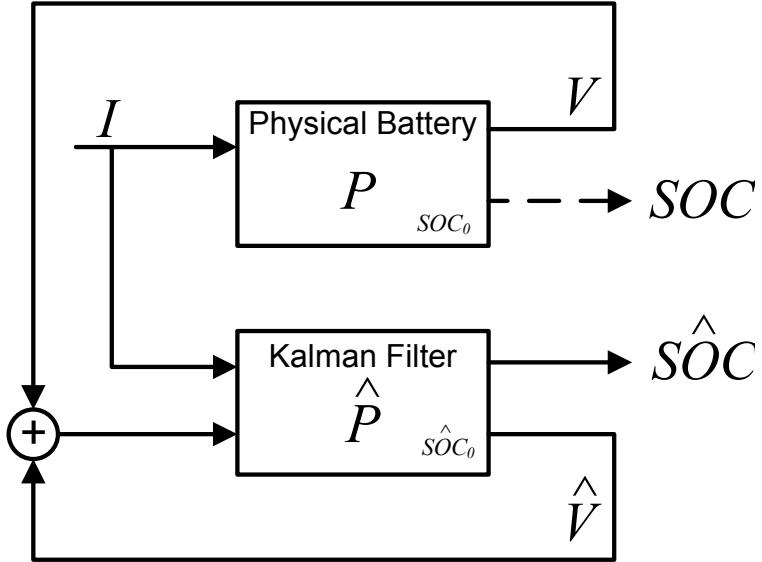
of the salient degradation mechanisms in Li-ion batteries. Then we formulate the SOH estimation problem as a parameter identification problem. That is, we postulate that parameters within equivalent circuit models change slowly over time. Our goal is to identify those parameter values from measurement data using, for example, least squares identification.

The next topic is charge balancing. Charge balancing is motivated by the desire to ensure individual cells connected in series do not over-charge or over-discharge. This situation arises when one can only afford to monitor and control groups of cells, as opposed to each individual cell. Moreover, the characteristic behavior may vary slightly from cell to cell. This is especially true for high energy capacity battery packs which can contain thousands of cells. As such, we introduce passive balancing techniques (e.g. shunt-resistors or switched capacitors) and active balancing techniques (e.g. SOC-polling or power electronics). To demonstrate these methods, an example homework problem is included in Section B.3. We also discuss the charge balancing concept from Chapter 4 of this dissertation.

The final section of this chapter discusses thermal modeling and management of batteries. Thermal management is a critical challenge for vehicular battery systems for several reasons. First, vehicles may encounter a wide range of environments, from the freezing temperatures of Oslo, Norway to the scorching hot desert regions in the Middle East. Second, the high charge/discharge rates and tight packaging associated with vehicle systems can produce elevated temperature levels. Third, temperature has a direct impact on health degradation and efficiency. Motivated by these challenges, we introduce the students to lumped thermal models of individual cells. These models are identified through least squares identification techniques. To close this chapter we provide an overview of the various thermal management actuation methods and how they scale from cells to packs.

B.2.4 Vehicle Power Management

The final chapter discusses vehicle power management. This chapter demonstrates how battery systems integrate within vehicle powertrains. First we review various hybrid and electric architectures. These include series, parallel, and power-split hybrids. We also discuss the power electronics and electric motor topologies typically used in electrified vehicles. Next we discuss hybrid vehicle power management, which seeks to design control systems which manage the power split between batteries and other power sources (e.g. IC engine, fuel cell, ultracapacitor). This component is strongly

Figure B.5 Block diagram of SOC estimation scheme using the single particle model and a Kalman filter.

based upon the models, problem formulation, and results described in Chapters 2 and 3 of this dissertation. The final topic covers the interaction between electrified transportation and power grids. Specifically, we discuss consumer-side charge trajectory optimization and power demand prediction for grid-connected PHEVs. The PHEV/grid interaction material is also based upon an outgrowth of research from this dissertation [82, 83].

B.3 Example Assignments

This section describes several homework problems which exercise the fundamental tools developed in lecture. These assignments are the mechanism by which we execute the third step of our pedagogical philosophy: exercise fundamental tools on application relevant problems. In this appendix we describe the SOC estimation and charge balancing problems.

B.3.1 The SOC Estimation Problem

In the battery course the students are instructed to solve the most prominent battery estimation problem - SOC estimation. In many battery powered systems (e.g. laptops,
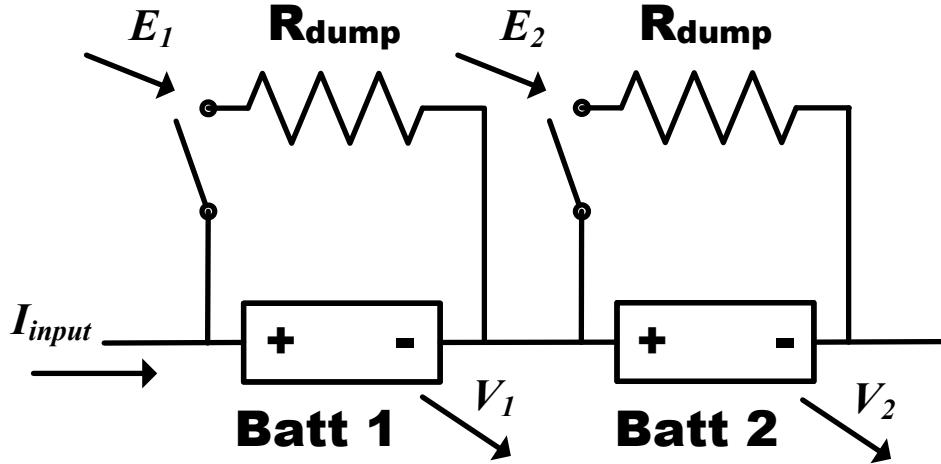
electronic portable devices, and electric vehicles) one typically desires to know the battery SOC level, which represents the remaining available energy. Unfortunately, it is often impractical to implement sensors that directly measure the lithium-ion concentration in the solid material of the electrodes. We do, however, typically have access to voltage and current measurements. These measurements in combination with a control-oriented battery cell model allow us to dynamically estimate SOC [163]. A block diagram of the estimation scheme is provided in Fig. B.5.

In this assignment the students apply a linearized version of the single particle model described in section B.2.2 with a Kalman filter to estimate battery SOC. The students then learn how Kalman filters can be tuned to tradeoff sensor noise with modeling errors by injecting Gaussian noise into the measured signals and applying incorrect initial conditions to the estimator. Consequently, the students learn about Kalman filtering theory while simultaneously solving a very practical battery systems problem using physical models developed in class.

B.3.2   The Charge Balancing Problem

A second battery systems and control problem relevant for vehicle applications is charge balancing. This problem is motivated by the fact that cells connected in series within battery packs may have unequal charge levels. This situation is problematic because individual cells can be inadvertently overcharged or over-discharged because the battery management system considers total battery pack voltage without knowledge of individual cell voltage. The end result is accelerated battery pack degradation and possibly catastrophic thermal runaway. This situation can be mitigated via a charge balancing scheme. A survey of such schemes can be found in [101].

In this assignment the students design and simulate a battery management system that utilizes shunt resistors to balance the voltage levels of two unbalanced cells connected in series. A schematic of the balancing scheme is shown in Fig. B.6. The students are instructed to use their creativity to design logic that compares the individual voltage levels to actuate the switches in a manner that equalizes cell voltage. Moreover, they are free to design the resistance value of the shunt resistors. They use simulation results and mathematical arguments to analyze how the shunt resistor method suffers from an inherent tradeoff between equalization time and power efficiency. Finally, they discover how voltage balancing does not necessarily balance SOC, motivating the application of SOC balancing schemes [181].

Figure B.6 Circuit diagram of shunt resistor equalization circuit.

B.4 Conclusion

This appendix describes a newly developed course on battery systems and control which has been directly impacted by the present dissertation. Like this dissertation, the course is focused on system-level modeling, design, and control. The objective of this courses is to educate a new generation of engineers capable of developing advanced sustainable transportation systems powered by batteries.

For the first two offerings topics were covered in a conceptual manner. However, we recognize that student engagement thrives on application case studies and hardware experiments. In future terms we will add laboratory components to each course. This equipment will be shared for instruction across multiple courses and research across multiple teams/departments, thus financially benefiting from high-throughput. Images of this equipment are provided in Fig. 2.7 and 2.8 of Section 2.1.3. We envision that the students will solve homework problems via analysis and simulation first, then apply their designs to the laboratory battery test system. Pedagogically, these enhancements will marry conceptual analysis with hardware implementation - effectively increasing the impact and accessibility of each course. Through these efforts we anticipate a profound impact on job creation in sustainable transportation systems through education.

Acknowledgment

COURSE #: ME 499 / 599	COURSE TITLE: BATTERY SYSTEMS & CONTROLS
TERMS OFFERED: Winter	PREREQUISITES: ME 360 Modeling, Analysis and Control of Dynamic Systems ME 400 Mechanical Engineering Analysis
TEXTBOOKS/REQUIRED MATERIAL: A coursepack of lecture notes and handouts will be distributed through Ctools.	COGNIZANT FACULTY: Stefanopoulou, Fathy, Moura
INSTRUCTOR: Stefanopoulou and Moura	FACULTY APPROVAL:
CoE BULLETIN DESCRIPTION: Introduction to battery modeling, control, and experimental characterization as related to electrified transportation systems. Emphasis is placed upon system-level modeling, system identification, model reduction, control and estimation. Specific topics include state-of-charge estimation, thermal dynamics, charge management, power electronics, and hybrid vehicle power management.	COURSE TOPICS: (approximate number of hours in parentheses) 1. Introduction, chemistries, circuit analysis, and test protocols (4) 2. Modeling and simulation of equivalent circuit and electrochemical models (9) 3. Battery control problems (8) 4. Thermal modeling and control (2) 5. Vehicle and Vehicle-to-Grid level problems (4)

COURSE STRUCTURE/SCHEDULE: 2 lectures per week @ 1.5 hours	
COURSE OBJECTIVES	Links shown in brackets are to course outcomes that satisfy these objectives. 1. Introduce students to the broad issues and challenges associated with electrified transportation [1,6] 2. Show students how to design, execute, and analyze laboratory experiments [7] 3. Link fundamental physics and mathematics principles to application-oriented problems in electrified transportation [1-7] 4. Provide opportunities for solving practical problems, through computer simulation or experimentation [1-7]
COURSE OUTCOMES	Links shown in brackets are to program educational outcomes. 1. Identify high-level technical challenges and distill them into technical, solvable engineering problems [a-k] 2. Derive equation s that model battery dynamics, from circuit or electrochemical principles [a,c,e,k] 3. Apply model reduction techniques to complex dynamic models [a,c,e,k] 4. Synthesize Kalman filters for battery state-of-charge estimation [a,c,e,k] 5. Design charge management algorithms [a,c,e,k] 6. Apply control and estimation techniques to vehicle-level and vehicle-to-grid level problems [a,c-e, g-k] 7. Design experimental protocols for general battery characterization [a-g,k]
ASSESSMENT TOOLS	1. Ten homework assignments assess outcomes 1-6. 2. A group laboratory project assesses outcome 7. 3. End of term course evaluation provides student self-assessment of all course outcomes, 1-7.

Figure B.7 ABET Course Profile

Appendix C

Nomenclature

Symbol	Description	Units
A_{fr}	Effective frontal area of vehicle	[m^2]
a	Vehicle acceleration	[m/s^2]
a_n	Specific surface area of anode	[m^2/m^3]
C_d	Aerodynamic drag coefficient	[-]
$c(\cdot, \cdot)$	Instantaneous cost function	
F	Faraday's constant	[C/mol]
F_g	Planetary gear force	[N]
I	Current through each cell	[A]
I_e	Engine inertia	[kg·m^2]
$I_{M/G1}$	Motor/generator 1 inertia	[kg·m^2]
$I_{M/G2}$	Motor/generator 2 inertia	[kg·m^2]
I_w	Wheel inertia	[kg·m^2]
i_0	Battery pack current	[A]
$i_{0,s}$	Exchange current density for side reaction	[A/m^2]
i_1, i_2	Cell current	[A]
J^g	Optimal cost for control policy g	[-]
J_s	Current density of side reaction	[A/m^3]
K	Final drive ratio	[-]
M_P	Molecular weight of product from side reaction	[mol/kg]
m	Vehicle mass	[kg]
n_p	Number of parallel strings of cells	[-]
n_s	Number of cells in series per string	[-]
P_{batt}	Power transfer from battery pack	[W]
Q_{batt}	Battery pack charge capacity	[A·s]
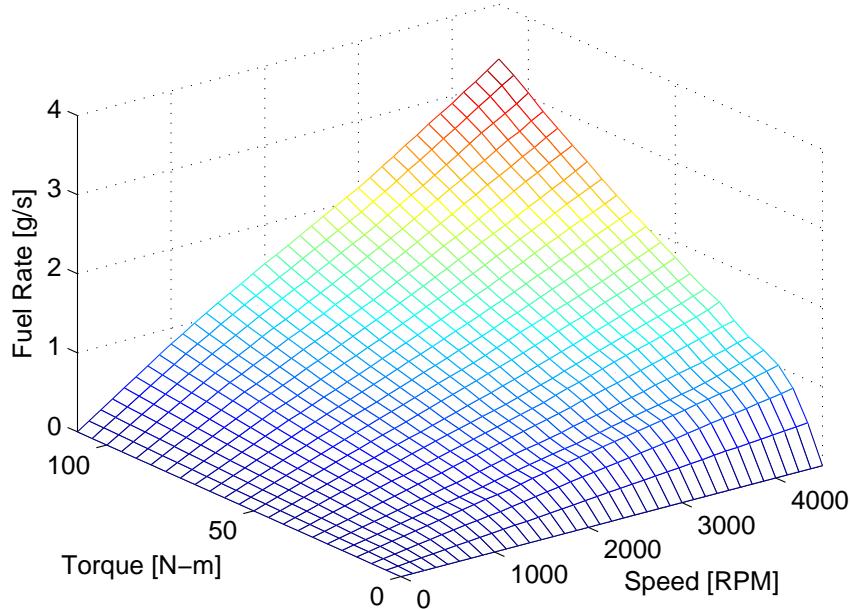
Symbol	Description	Units
R	Number of teeth on ring gear	[-]
R_{gas}	Universal gas constant	[J/K/mol]
R_{batt}	Internal resistance of battery pack	[Ω]
R_{SEI}	Resistance of solid electrolyte interphase (SEI) layer	[Ω/m^2]
R_{tire}	Tire radius	[m]
S	Number of teeth on sun gear	[-]
SOC	Battery state of charge	[-]
T_e	Engine torque	[N·m]
$T_{M/G1}$	Motor/generator 1 torque	[N·m]
$T_{M/G2}$	Motor/generator 2 torque	[N·m]
$U_{s,ref}$	Equilibrium potential of side reaction	[V]
$U(x)$	Admissible set of controls	
V_{cell}	Voltage of individual battery cell	[V]
V_{oc}	Battery pack open circuit voltage	[V]
v	Vehicle speed	[m/s]
W_{fuel}	Mass flow rate of fuel	[g/s]
X	Admissible set of states	
x	Spatial coordinate across cell	[m/m]
α	Linear objective weight	[-]
β	Energy price ratio	[USD/USD]
$(\overline{\delta_{film}})\ \delta_{film}$	(Spatially averaged) anode-side resistive film thickness	[pm/m^2]
η_{grid}	Grid-to-PHEV charging efficiency	[-]
$\eta_{M/G1}$	Motor/generator 1 power efficiency	[-]
$\eta_{M/G2}$	Motor/generator 2 power efficiency	[-]
η_s	Over potential driving side reaction	[V]
κ_P	Conductivity of electrolyte	[1/m/Ω]
μ_{roll}	Rolling friction coefficient	[-]
ρ	Air density	[kg/m^3]
ρ_P	Side reaction product density	[kg/m^2]
ϕ_1, ϕ_2	Solid, electrolyte potential	[V]
ω_e	Engine crankshaft speed	[rad/s]
$\omega_{M/G1}$	Motor/generator 1 speed	[rad/s]
$\omega_{M/G2}$	Motor/generator 2 speed	[rad/s]

Appendix D
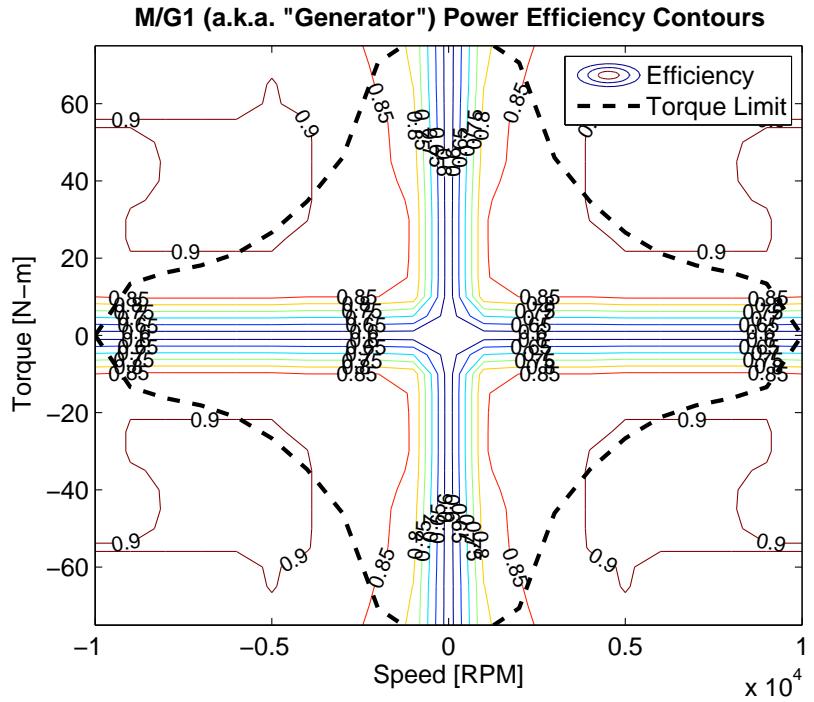
Model Parameters

D.1 PHEV Model
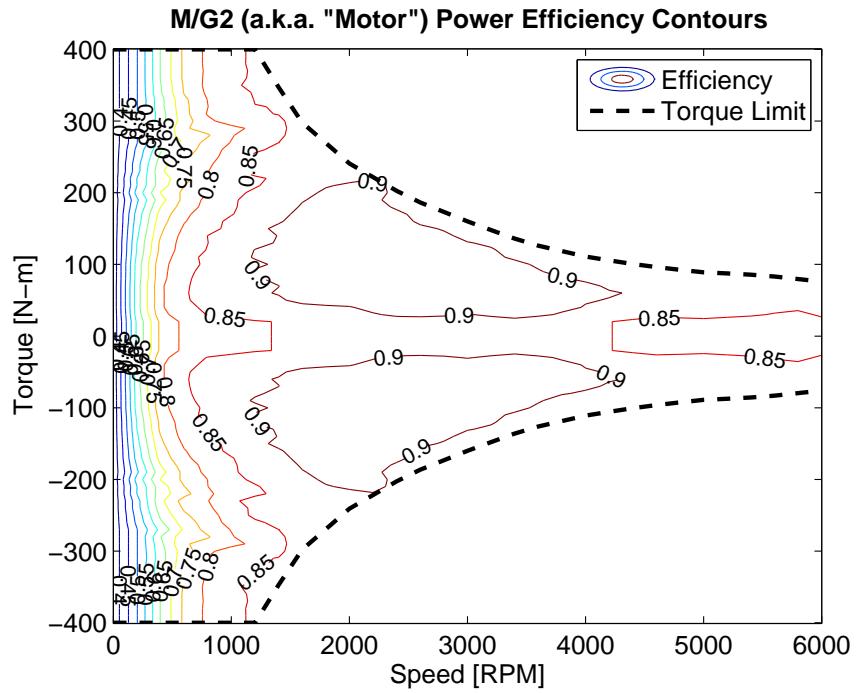
The engine fuel rate, $W(T_e, \omega_e)$, in terms of g/s are provided in Fig D.1 as a function of engine torque and speed. Figures D.2 and D.3 show the power efficiency contours of M/G1 and M/G2 respectively as functions of torque and speed. In both plots the dotted lines indicate torque limits as functions of speed. These constraints are implemented as described in Section 3.1.2. These empirical models are adapted from Argonne National Laboratory's PSAT software program [9].

Figure D.1 Empirical model of engine fuel rate versus engine speed and torque from PSAT [9]
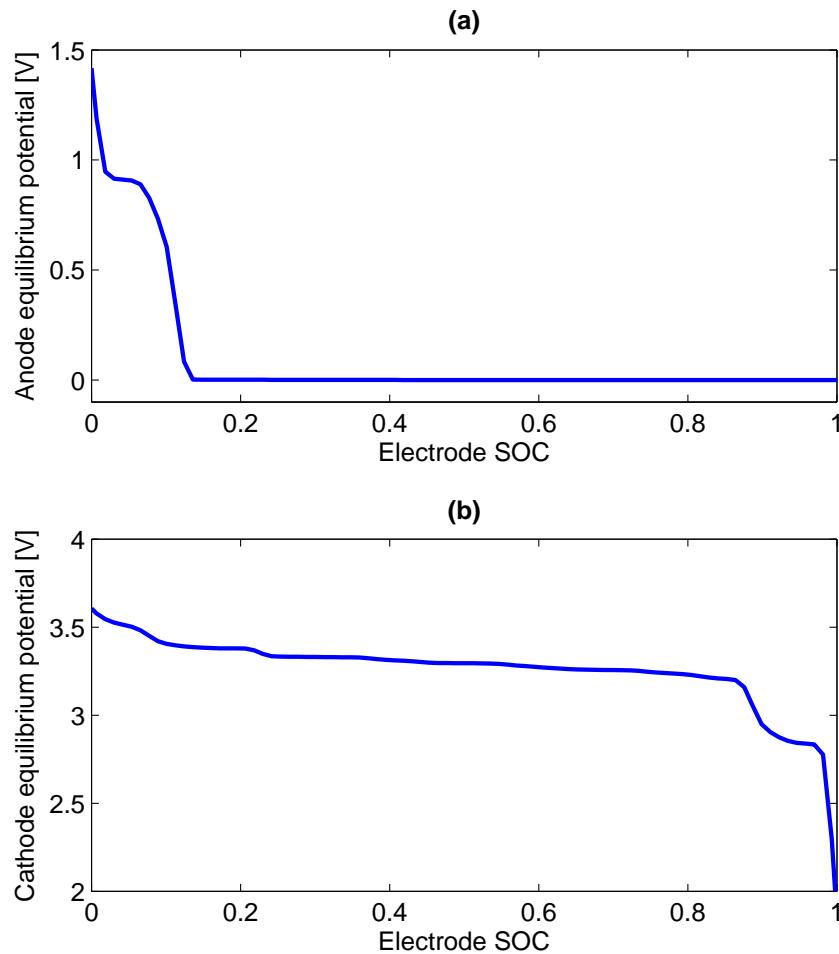
Figure D.2 Empirical model of M/G1 (a.k.a. "generator") power efficiency versus speed and torque from PSAT [9]

Figure D.3 Empirical model of M/G2 (a.k.a. "motor") power efficiency versus speed and torque from PSAT [9]

D.2 Equilibrium Potentials of Battery Electrodes

Section 2.1.2 describes the electrochemical battery model, in which the term $U_{ref,j}(\theta_j)$ appears in the overpotential equation (2.18). This term represents the equilibrium potential of each electrode ($j \in \{n, p\}$ corresponds to the negative and positive electrodes, respectively) as a function of that electrode's bulk SOC, θ_j. These equilibrium potential functions were identified from the genetic parameter identification procedure described in [10] and are provided in Fig. D.4.

Figure D.4 Equilibrium potentials of the (a) anode and (b) cathode as identified from the genetic parameter identification procedure in [10].

D.3 SEI Growth Model Parameters

Table D.1 provides parameter values for each SEI growth model analyzed in the sensitivity analysis of Section 4.4.5. The first column of parameters shown in Table D.1 are adopted from [7]. The second column of parameters have been identified to produce capacity fade trends that match the manufacturer's cycling and storage data [150].

Table D.1 SEI Growth Model Parameters for Sensitivity Analysis in Section 4.4.5

| | Values for map depicted in | |
Symbol	Fig. 2.6 & 4.10(a)	Fig. 4.10(b)
$i_{0,s}$	1.5×10^{-6} A/m^2	4×10^{-8} A/m^2
M_P	73000 mol/kg	73000 mol/kg
R_{SEI}	7.4 mΩ·m^2	7.4 mΩ·m^2
$U_{s,ref}$	0.4 V	0.4 V
κ_P	1 (m·Ω)$^{-1}$	1 (m·Ω)$^{-1}$
ρ_P	2100 kg/m^2	2100 kg/m^2
$U_{ref,n}(\theta_n)$	Adopted from [7]	Adopted from [150]

Appendix E

Distribution Convergence via the Central Limit Theorem

The simulation method in Section 3.3 calculates the PHEV performance characteristics across a number of randomly generated drive cycles. The stopping criterion in this appendix seeks to answer the question: how many drive cycles are necessary to ensure the distribution of simulated PHEV performance characteristics has converged to the true distribution? Specifically, we seek convergence for the trip cost distribution. The central limit theorem (CLT) allows us to approximate how many iterations n we must simulate the study (see Section 3.3) in order that the sample mean is within a fraction a of the population mean with probability of at least b [182]. Mathematically, the main result is provided by the following proposition:

Proposition 2. *Suppose C_i is a random variable representing the trip cost for the ith drive cycle simulation. Furthermore, suppose that the C_i's are independently and identically distributed with mean $E[C]$ and standard deviation std(C) for the true population. Then the number of iterations n for which*

$$Pr\left(\left|\frac{\frac{1}{n}\sum_{i=1}^{n} C_i - E[C]}{E[C]}\right| \leq a\right) \geq b \tag{E.1}$$

is satisfied is given by:

$$n \geq \left[\frac{std(C)}{E[C]a}\Phi^{-1}\left(\frac{b+1}{2}\right)\right]^2 \tag{E.2}$$

Proof. Let us attempt to re-write the left hand side of (E.1) to represent a random variable with zero mean and unit variance, which will satisfy the key hypothesis of

the CLT. This can be accomplished through the following algebraic manipulations:

$$\Pr\left(-a \leq \frac{\frac{1}{n}\sum_{i=1}^{n} C_i - \mathrm{E}[C]}{\mathrm{E}[C]} \leq a\right) \geq b \qquad (\text{E.3})$$

$$\Pr\left(-an\mathrm{E}[C] + n\mathrm{E}[C] \leq \sum_{i=1}^{n} C_i \leq an\mathrm{E}[C] + n\mathrm{E}[C]\right) \geq b \qquad (\text{E.4})$$

$$\Pr\left(-an\mathrm{E}[C] \leq \sum_{i=1}^{n} (C_i - \mathrm{E}[C]) \leq an\mathrm{E}[C]\right) \geq b \qquad (\text{E.5})$$

$$\Pr\left(\frac{-an\mathrm{E}[C]}{\mathrm{std}(C)} \leq \sum_{i=1}^{n} \left(\frac{C_i - \mathrm{E}[C]}{\mathrm{std}(C)}\right) \leq \frac{an\mathrm{E}[C]}{\mathrm{std}(C)}\right) \geq b \qquad (\text{E.6})$$

$$\Pr\left(\frac{-a\mathrm{E}[C]}{\sqrt{n}\mathrm{std}(C)} \leq \frac{1}{\sqrt{n}}\sum_{i=1}^{n} \left(\frac{C_i - \mathrm{E}[C]}{\mathrm{std}(C)}\right) \leq \frac{a\mathrm{E}[C]}{\sqrt{n}\mathrm{std}(C)}\right) \geq b \qquad (\text{E.7})$$

Let us define the random variable in the center of the inequality to be equal to Y_n, which has zero mean and unit variance for all values of n.

$$\Pr\left(\frac{-a\mathrm{E}[C]}{\sqrt{n}\mathrm{std}(C)} \leq Y_n \leq \frac{a\mathrm{E}[C]}{\sqrt{n}\mathrm{std}(C)}\right) \geq b \qquad (\text{E.8})$$

The CLT states $\lim_{n\to\infty} F_{Y_n}(y) = \Phi(y)$, where Φ denotes the cdf of a zero mean, unit variance normal distribution. Therefore, we may approximate the left hand side of (E.8) by:

$$2\Phi\left(\frac{a\mathrm{E}[C]}{\sqrt{n}\mathrm{std}(C)}\right) - 1 \geq b \qquad (\text{E.9})$$

which uses the property of normal cdf's $\Pr(-\alpha \leq Y_n \leq \alpha) = 2\Phi(\alpha) - 1$, for some $\alpha \in \mathbb{R}$. Solving for n allows us to arrive at the following criterion:

$$n \geq \left[\frac{\mathrm{std}(C)}{\mathrm{E}[C]a}\Phi^{-1}\left(\frac{b+1}{2}\right)\right]^2 \qquad (\text{E.10})$$

where Φ^{-1} is the inverse of the zero-mean, unit variance normal cumulative distribution function. $\square$

The exact derivation of (E.10) requires knowledge of the population's mean $\mathrm{E}[C]$ and standard deviation $\mathrm{std}(C)$ beforehand. However we approximate these values by the sample mean and sample standard deviation since we do not know the true population metrics exactly. In practice, we run 100 simulations before computing the stopping condition (E.10) in order to obtain a reasonably accurate estimate and avoid premature termination. The stopping criterion parameters used in this study

are $a = 0.05$ and $b = 0.95$.

Bibliography

[1] "States with Renewable Portfolio Standards," May. 2009. [Online]. Available: http://apps1.eere.energy.gov/states/maps/renewable_portfolio_states.cfm#chart

[2] M. Hoexter, "The Renewable Electron Economy Part VII: Stationary Energy Storage — A Key to the Renewable Grid," Oct. 2007. [Online]. Available: http://www.futurelab.net/blogs/marketing-strategy-innovation/2007/10/the_renewable_electron_economy_3.html

[3] G. Garavaglia. (Before 1834) Picture of A. Volta, the noted physicist and electrical researcher. [Online]. Available: http://en.wikipedia.org/wiki/File:Volta_A.jpg

[4] Unknown. (18-19th century) Portrait of Luigi Galvani (1737-1798), Italian physicists. [Online]. Available: http://en.wikipedia.org/wiki/File:Luigi_Galvani,_oil-painting.jpg

[5] K. Muta, M. Yamazaki, and J. Tokieda, "Development of New-Generation Hybrid System THS II - Drastic Improvement of Power Performance and Fuel Economy," *2004 SAE World Congress, SAE Paper 2004-01-0064*, 2004.

[6] US-DOE, "Average retail price of electricity to ultimate customers by end-use sector, by state," U.S. Energy Information Administration, Tech. Rep., 2010, http://www.eia.doe.gov/electricity/epm/table5_6_b.html.

[7] P. Ramadass, B. Haran, P. Gomadam, R. White, and B. Popov, "Development of first principles capacity fade model for Li-ion cells," *Journal of the Electrochemical Society*, vol. 151, no. 2, pp. 196 – 203, 2004.

[8] P. Flynn and et al., *Meeting the Energy Needs of Future Warriors*, Committee on Soldier Power/Energy Systems, Board on Army Science and Technology, National Research Council of the Nation Academies, Ed. The National Academies Press, 2004.

[9] A. Rousseau, J. Kwon, P. Sharer, and M. Duoba, "Integrating Data, Performing Quality Assurance, and Validating the Vehicle Model for the 2004 Prius Using PSAT," *SAE Papers 2006-01-0667*, 2006.

[10] J. C. Forman, S. J. Moura, J. L. Stein, and H. K. Fathy, "Parameter Identification of the Doyle-Fuller-Newman Model Based on Experimental Cycling of a Li-ion LiFePO4 Battery Using a Genetic Algorithm," *2011 American Control Conference*, 2011.

[11] D. Obey, "American Recovery and Reinvestment Act of 2009," Feb. 2009, Public Law No: 111-5. [Online]. Available: http://frwebgate.access.gpo.gov/cgi-bin/getdoc.cgi?dbname=111_cong_public_laws&docid=f:publ005.pdf

[12] L. Burns, J. McCormick, and C. Borroni-Bird, "Vehicle of change," *Scientific American*, vol. 287, no. 4, pp. 40–49, 2002.

[13] W. Kempton and J. Tomic, "Vehicle-to-grid power fundamentals: Calculating capacity and net revenue," *Journal of Power Sources*, vol. 144, no. 1, pp. 268–279, 2005.

[14] ——, "Vehicle-to-grid power implementation: From stabilizing the grid to supporting large-scale renewable energy," *Journal of Power Sources*, vol. 144, no. 1, pp. 280–294, 2005.

[15] B. K. Sovacool and R. F. Hirsh, "Beyond batteries: An examination of the benefits and barriers to plug-in hybrid electric vehicles (PHEVs) and a vehicle-to-grid (V2G) transition," *Energy Policy*, vol. 37, no. 3, pp. 1095–1103, 3 2009.

[16] J. Newman and K. Thomas-Alyea, *Electrochemical Systems*. John Wiley & Sons, Inc., 2004.

[17] D. Linden and T. B. Reddy, *Handbook of Batteries (3rd Edition)*. McGraw-Hill, 2002.

[18] R. Huggins, *Advanced batteries: materials science aspects*. Springer Verlag, 2008.

[19] T. Nagaura and K. Tozawa, "Lithium ion rechargeable battery," *Progress in Batteries and Solar Cells*, vol. 9, pp. 209–217, 1990.

[20] A. Padhi, K. Nanjundaswamy, and J. Goodenough, "Phospho-olivines as positive-electrode materials for rechargeable lithium batteries," *Journal of the Electrochemical Society*, vol. 144, no. 4, pp. 1188 – 1194, 1997.

[21] J. Tarascon, A. Gozdz, C. Schmutz, F. Shokoohi, and P. Warren, "Performance of bellcore's plastic rechargeable li-ion batteries," vol. 86-88, July 1996, pp. 49 – 54.

[22] J. Tarascon and M. Armand, "Issues and challenges facing rechargeable lithium batteries," *Nature*, vol. 414, no. 6861, pp. 359–367, 2001.

[23] M. Broussely, P. Biensan, and B. Simon, "Lithium insertion into host materials: the key to success for Li ion batteries," *Electrochimica Acta*, vol. 45, no. 1, pp. 3 – 22, 1999.

[24] M. Verbrugge and B. Koch, "Lithium intercalation of carbon-fiber microelectrodes," *Journal of the Electrochemical Society*, vol. 143, no. 1, pp. 24–31, Jan 1996.

[25] J. S. Gnanaraj, R. W. Thompson, J. F. DiCarlo, and K. M. Abraham, "The role of carbonate solvents on lithium intercalation into graphite," *Journal of the Electrochemical Society*, vol. 154, no. 3, pp. A185–A191, 2007.

[26] X. Zhang, A. M. Sastry, and W. Shyy, "Intercalation-induced stress and heat generation within single lithium-ion battery cathode particles," *Journal of the Electrochemical Society*, vol. 155, no. 7, pp. A542 – A552, 2008.

[27] A. Van Der Ven, K. Garikipati, S. Kim, and M. Wagemaker, "The role of coherency strains on phase stability in lixfepo 4: Needle crystallites minimize coherency strain and overpotential," *Journal of the Electrochemical Society*, vol. 156, no. 11, pp. A949 – A957, 2009.

[28] V. Ramadesigan, R. N. Methekar, F. Latinwo, R. D. Braatz, and V. R. Subramanian, "Optimal porosity distribution for minimized ohmic drop across a porous electrode," *Journal of the Electrochemical Society*, vol. 157, no. 12, pp. A1328 – A1334, 2010.

[29] D. Morgan, A. Van der Ven, and G. Ceder, "Li conductivity in LixMPO4 (M = Mn, Fe, Co, Ni) olivine materials," *Electrochemical and Solid State Letters*, vol. 7, no. 2, pp. A30–A32, 2004.

[30] D. Aurbach, "Review of selected electrode-solution interactions which determine the performance of Li and Li ion batteries," *J. of Power Sources*, vol. 89, no. 2, pp. 206 – 18, 2000.

[31] P. Arora, R. E. White, and M. Doyle, "Capacity fade mechanisms and side reactions in lithium-ion batteries," *Journal of the Electrochemical Society*, vol. 145, no. 10, pp. 3647 – 3667, 1998.

[32] L. Kanevskii and V. Dubasova, "Degradation of lithium-ion batteries and how to fight it: A review," *Russian Journal of Electrochemistry*, vol. 41, no. 1, pp. 3 – 19, 2005.

[33] M. Doyle, T. Fuller, and J. Newman, "Modeling of galvanostatic charge and discharge of the lithium/polymer/insertion cell," *Journal of the Electrochemical Society*, vol. 140, no. 6, pp. 1526 – 33, 1993.

[34] T. Fuller, M. Doyle, and J. Newman, "Simulation and optimization of the dual lithium ion insertion cell," *Journal of the Electrochemical Society*, vol. 141, no. 1, pp. 1 – 10, 1994.

[35] A. Sciarretta and L. Guzzella, "Control of hybrid electric vehicles," *IEEE Control Systems Magazine*, vol. 27, no. 2, pp. 60 – 70, 2007.

[36] C. Lin, H. Peng, J. Grizzle, and J. Kang, "Power management strategy for a parallel hybrid electric truck," *Control Systems Technology, IEEE Transactions on*, vol. 11, no. 6, pp. 839–849, 2004.

[37] C.-C. Lin, "Modeling and Control Strategy Development for Hybrid Vehicles," Ph.D. dissertation, University of Michigan, Ann Arbor, 2004.

[38] M. P. O'Keefe and T. Markel, "Dynamic Programming Applied to Investigate Energy Management Strategies for a Plug-In HEV," *22nd International Battery, Hybrid and Fuel Cell Electric Vehicle Symposium, (EVS-22)*, October 23, 2006 2006.

[39] Q. Gong, Y. Li, and Z.-R. Peng, "Trip-based optimal power management of plug-in hybrid electric vehicles," *IEEE Transactions on Vehicular Technology*, vol. 57, no. 6, pp. 3393–3401, 2008.

[40] L. Johannesson, M. Asbogard, and B. Egardt, "Assessing the potential of predictive control for hybrid vehicle powertrains using stochastic dynamic programming," *IEEE Transactions on Intelligent Transportation Systems*, vol. 8, no. 1, pp. 71 – 83, 2007.

[41] E. Tate, "Techniques for Hybrid Electric Vehicle Controller Synthesis," Ph.D. dissertation, Electrical Engineering: Systems, University of Michigan, Ann Arbor, 2007.

[42] S. J. Moura, H. K. Fathy, D. S. Callaway, and J. L. Stein, "A Stochastic Optimal Control Approach for Power Management in Plug-in Hybrid Electric Vehicles," *IEEE Transactions on Control Systems Technology*, no. pp, 2010.

[43] A. Vahidi, A. Stefanopoulou, and H. Peng, "Current management in a hybrid fuel cell power system: A model-predictive control approach," *IEEE Transactions on Control Systems Technology*, vol. 14, no. 6, pp. 1047–1057, 2006.

[44] G. Ripaccioli, D. Bernardini, S. Di Cairano, A. Bemporad, and I. Kolmanovsky, "A stochastic model predictive control approach for series hybrid electric vehicle power management," *2010 American Control Conference*, pp. 5844 – 9, 2010.

[45] C. Musardo, G. Rizzoni, Y. Guezennec, and B. Staccia, "A-ECMS: An adaptive algorithm for hybrid electric vehicle energy management," *European Journal of Control*, vol. 11, no. 4-5, pp. 509–524, 2005.

[46] P. Rodatz, G. Paganelli, A. Sciarretta, and L. Guzzella, "Optimal power management of an experimental fuel cell/supercapacitor-powered hybrid vehicle," *Control Engineering Practice*, vol. 13, no. 1, pp. 41–53, 2005.

[47] L. Serrao, S. Onori, and G. Rizzoni, "ECMS as a realization of Pontryagin's minimum principle for HEV control," in *2009 American Control Conference*, June 2009, pp. 3964 –3969.

[48] D. Opila, "Incorporating Drivability Metrics into Optimal Energy Management Strategies for Hybrid Vehicles," Ph.D. dissertation, Mechanical Engineering, University of Michigan, Ann Arbor, 2010.

[49] N. Kim, S. Cha, and H. Peng, "Optimal Control of Hybrid Electric Vehicles Based on Pontryagin's Minimum Principle," *IEEE Transactions on Control Systems Technology*, vol. PP, no. 99, pp. 1 –9, 2011.

[50] J. Liu and H. Peng, "Modeling and control of a power-split hybrid vehicle," *Control Systems Technology, IEEE Transactions on*, vol. 16, no. 6, pp. 1242–1251, 2008.

[51] D. Rotenberg, A. Vahidi, and I. Kolmanovsky, "Ultracapacitor assisted powertrains: modeling, control, sizing, and the impact on fuel economy," in *2008 American Control Conference (ACC '08)*, Dept. of Mech. Eng., Clemson Univ., Clemson, SC, USA.   Piscataway, NJ, USA: IEEE, 11-13 June 2008 2008, pp. 981–7.

[52] B. Wu, C. Lin, Z. Filipi, H. Peng, and D. Assanis, "Optimal power management for a hydraulic hybrid delivery truck," *Vehicle System Dynamics*, vol. 42, no. 1-2, pp. 23–40, July 2004.

[53] D. Kum, H. Peng, and N. Bucknor, "Modeling and control of hybrid electric vehicles for fuel and emission reduction," in *2008 ASME Dynamic Systems and Control Conference*, 2008, pp. 1247–1254.

[54] D. F. Opila, D. Aswani, R. McGee, J. A. Cook, and J. W. Grizzle, "Incorporating drivability metrics into optimal energy management strategies for hybrid vehicles," *47th IEEE Conference on Decision and Control*, pp. 4382–9, 2008.

[55] S. J. Moura, H. K. Fathy, D. S. Callaway, and J. L. Stein, "A stochastic optimal control approach for power management in plug-in hybrid electric vehicles," *ASME Dynamic Systems and Control Conference*, Oct. 2008.

[56] E. Gatzke, A. Stamps, C. Holland, and R. White, "Analysis of capacity fade in a lithium ion battery," *Journal of Power Sources*, vol. 150, pp. 229–39, 10/04 2005.

[57] M. Verbrugge and E. Tate, "Adaptive state of charge algorithm for nickel metal hydride batteries including hysteresis phenomena," *Journal of Power Sources*, vol. 126, no. 1-2, pp. 236–249, 2004.

[58] C. Gould, C. Bingham, D. Stone, and P. Bentley, "New battery model and state-of-health determination through subspace parameter estimation and state-observer techniques," *IEEE Transactions on Vehicular Technology*, vol. 58, no. 8, pp. 3905 – 3916, 2009.

[59] I.-S. Kim, "A technique for estimating the state of health of lithium batteries through a dual-sliding-mode observer," *IEEE Transactions on Power Electronics*, vol. 25, no. 4, pp. 1013 – 1022, 2010.

[60] D. V. Do, C. Forgez, K. El Kadri Benkara, and G. Friedrich, "Impedance observer for a li-ion battery using kalman filter," *IEEE Transactions on Vehicular Technology*, vol. 58, no. 8, pp. 3930 – 3937, 2009.

[61] G. L. Plett, "Extended Kalman filtering for battery management systems of LiPB-based HEV battery packs. Part 1. Background," *Journal of Power Sources*, vol. 134, no. 2, pp. 252–61, 08/12 2004.

[62] G. Plett, "Extended Kalman filtering for battery management systems of LiPB-based HEV battery packs. Part 2. Modeling and identification," *Journal of Power Sources*, vol. 134, no. 2, pp. 262 – 76, 2004.

[63] G. L. Plett, "Extended Kalman filtering for battery management systems of LiPB-based HEV battery packs. Part 3. State and parameter estimation," *Journal of Power Sources*, vol. 134, no. 2, pp. 277–92, 08/12 2004.

[64] J. Siegel, X. Lin, A. G. Stefanopoulou, and D. Gorsich, "Neutron Imaging of Lithium Concentration for Validation of Li-ion Battery State of Charge Estimation," *27th Army Science Conference*, 2010.

[65] K. Smith, C. Rahn, and C.-Y. Wang, "Model-based electrochemical estimation of lithium-ion batteries," *2008 IEEE International Conference on Control Applications (CCA) part of the IEEE Multi-Conference on Systems and Control*, pp. 714 – 19, 2008.

[66] D. Di Domenico, G. Fiengo, and A. Stefanopoulou, "Lithium-ion battery state of charge estimation with a kalman filter based on a electrochemical model," *2008 IEEE International Conference on Control Applications (CCA) part of the IEEE Multi-Conference on Systems and Control*, pp. 702 – 707, 2008.

[67] R. Klein, N. A. Chaturvedi, J. Christensen, J. Ahmed, R. Findeisen, and A. Kojic, "State estimation of a reduced electrochemical model of a lithium-ion battery," Baltimore, MD, USA, 2010, pp. 6618 – 6623.

[68] A. Schmidt, M. Bitzer, A. Imre, and L. Guzzella, "Model-based distinction and quantification of capacity loss and rate capability fade in li-ion batteries," *Journal of Power Sources*, vol. 195, no. 22, pp. 7634 – 8, 2010/11/15.

[69] B. Saha, K. Goebel, S. Poll, and J. Christophersen, "Prognostics methods for battery health monitoring using a bayesian framework," *Instrumentation and Measurement, IEEE Transactions on*, vol. 58, no. 2, pp. 291 –296, Feb 2009.

[70] B. Saha, K. Goebel, and J. Christophersen, "Comparison of prognostic algorithms for estimating remaining useful life of batteries," *Transactions of the Institute of Measurement and Control*, vol. 31, no. 3-4, pp. 293 – 308, 2009.

[71] M. Safari, M. Morcrette, A. Teyssot, and C. Delacourt, "Life-Prediction Methods for Lithium-Ion Batteries Derived from a Fatigue Approach," *Journal of The Electrochemical Society*, vol. 157, no. 6, pp. A713–A720, 2010.

[72] ——, "Life prediction methods for lithium-ion batteries derived from a fatigue approach," *Journal of The Electrochemical Society*, vol. 157, no. 7, pp. A892–A898, 2010.

[73] J. Liu, "Modeling, Configuration and Control Optimization of Power-Split Hybrid Vehicles," Ph.D. dissertation, University of Michigan, Ann Arbor, 2007.

[74] S. J. Moura, D. S. Callaway, H. K. Fathy, and J. L. Stein, "Impact of battery sizing on stochastic optimal power management in plug-in hybrid electric vehicles," Columbus, OH, United States, 2008, pp. 96 – 102.

[75] ——, "Tradeoffs between battery energy capacity and stochastic optimal power management in plug-in hybrid electric vehicles," *Journal of Power Sources*, vol. 195, no. 9, pp. 2979 – 2988, 2010.

[76] S. J. Moura, J. C. Forman, J. L. Stein, and H. K. Fathy, "Control of Film Growth in Lithium Ion Battery Packs via Switches," *2009 ASME Dynamic Systems and Control Conference*, 2009.

[77] S. Moura, J. Forman, S. Bashash, J. Stein, and H. Fathy, "Optimal Control of Film Growth in Lithium-Ion Battery Packs via Relay Switches," *Industrial Electronics, IEEE Transactions on*, vol. PP, no. 99, p. 1, 2010.

[78] S. J. Moura, J. L. Stein, and H. K. Fathy, "Battery Health-Conscious Power Management for Plug-in Hybrid Electric Vehicles via Stochastic Control," *2010 ASME Dynamic Systems and Control Conference*, 2010.

[79] K. Ariyur and M. Krstić, *Real-time optimization by extremum-seeking control.* Wiley-Interscience, 2003.

[80] Y. A. Chang and S. J. Moura, "Air Flow Control in Fuel Cell Systems: An Extremum Seeking Approach," *2009 American Control Conference*, 2009, St. Louis, MO, USA.

[81] S. Moura and Y. Chang, "Asymptotic Convergence through Lyapunov-based Switching in Extremum Seeking with Application to Photovoltaic Systems," in *American Control Conference (ACC), 2010*, July 2010, pp. 3542 –3548.

[82] S. Bashash, S. J. Moura, and H. K. Fathy, "Plug-in Hybrid Electric Vehicles Charge Pattern Optimization for Energy Cost and Battery Health," *submitted to Journal of Power Sources*, 2010.

[83] ——, "Battery Health-Conscious Plug-In Hybrid Electric Vehicle Grid Demand Prediction," *2010 ASME Dynamic Systems and Control Conference*, 2010.

[84] S. J. Moura and H. K. Fathy, "Optimal Boundary Control & Estimation of Diffusion-Reaction PDEs," *2011 American Control Conference*, 2011.

[85] S. J. Moura, J. B. Siegel, D. J. Siegel, H. K. Fathy, and A. G. Stefanopoulou, "Education on Vehicle Electrification: Battery Systems, Fuel Cells, and Hydrogen," in *2010 IEEE Vehicle Power and Propulsion Conference (VPPC)*, Sept. 2010, pp. 1–6.

[86] K. Mizushima, P. Jones, P. Wiseman, and J. Goodenough, "LixCoO2 (0¡ x¡-1): A new cathode material for batteries of high energy density," *Materials Research Bulletin*, vol. 15, no. 6, pp. 783–789, 1980.

[87] G. Girishkumar, B. McCloskey, A. Luntz, S. Swanson, and W. Wilcke, "Lithium-air battery: Promise and challenges," *Journal of Physical Chemistry Letters*, vol. 1, no. 14, pp. 2193 – 2203, 2010.

[88] R. Bhattacharyya, B. Key, H. Chen, A. Best, A. Hollenkamp, and C. Grey, "In situ NMR observation of the formation of metallic lithium microstructures in lithium batteries," *Nature Materials*, 2010.

[89] J. Zhou and P. Notten, "Studies on the degradation of li-ion batteries by the use of microreference electrodes," *Journal of Power Sources*, vol. 177, no. 2, pp. 553 – 560, 2008.

[90] H.-C. Wu, C.-Y. Su, D.-T. Shieh, M.-H. Yang, and N.-L. Wu, "Enhanced high-temperature cycle life of LiFePO4-based Li-ion batteries by vinylene carbonate as electrolyte additive," *Electrochemical and Solid-State Letters*, vol. 9, no. 12, pp. 537 – 541, 2006.

[91] K. Striebel, J. Shim, A. Sierra, H. Yang, X. Song, R. Kostecki, and K. McCarthy, "The development of low cost lifepo4-based high power lithium-ion batteries," *Journal of Power Sources*, vol. 146, no. 1-2, pp. 33 – 38, 2005.

[92] P. Liu, J. Wang, J. Hicks-Garner, E. Sherman, S. Soukiazian, M. Verbrugge, H. Tataria, J. Musser, and P. Finamore, "Aging Mechanisms of LiFePO4 Batteries Deduced by Electrochemical and Structural Analyses," *Journal of the Electrochemical Society*, vol. 157, no. 4, pp. A499–A507, 2010.

[93] M. Dubarry and B. Y. Liaw, "Identify capacity fading mechanism in a commercial LiFePO4 cell," *Journal of Power Sources*, vol. 194, no. 1, pp. 541 – 549, 2009.

[94] Y. Zhang, C.-Y. Wang, and X. Tang, "Cycling degradation of an automotive LiFePO4 lithium-ion battery," *Journal of Power Sources*, vol. 196, no. 3, pp. 1513 – 1520, 2011.

[95] K. Amine, J. Liu, and I. Belharouak, "High-temperature storage and cycling of C-LiFePO4/graphite Li-ion cells," *Electrochemistry Communications*, vol. 7, no. 7, pp. 669 – 673, 2005.

[96] H.-H. Chang, H.-C. Wu, and N.-L. Wu, "Enhanced high-temperature cycle performance of LiFePO4/carbon batteries by an ion-sieving metal coating on negative electrode," *Electrochemistry Communications*, vol. 10, no. 12, pp. 1823 – 1826, 2008.

[97] F. Huet, "A review of impedance measurements for determination of the state-of-charge or state-of-health of secondary batteries," *Journal of Power Sources*, vol. 70, no. 1, pp. 59 – 69, 1998.

[98] *High Power Lithium Ion ANR26650M1 Data Sheet*, A123 Systems, 2006.

[99] J. C. Forman, S. Bashash, J. L. Stein, and H. K. Fathy, "Reduction of an Electrochemistry-Based Li-Ion Battery Model via Quasi-Linearization and Pad[e-acute] Approximation," *Journal of The Electrochemical Society*, vol. 158, no. 2, pp. A93–A101, 2011.

[100] D. LeBlanc, J. Sayer, C. Winkler, R. Ervin, S. Bogard, J. Devonshire, M. Mefford, M. Hagan, Z. Bareket, R. Goodsell, *et al.*, "Road departure crash warning system field operational test: Methodology and results," *University of Michigan Transportation Research Institute, Tech. Rep. UMTRI-2006-9-1, June*, 2006.

[101] A. Baughman and M. Ferdowsi, "Battery charge equalization-state of the art and future trends," *SAE Transactions: Electronic and electrical systems, Paper No. 2005-01-3474*, 2005.

[102] W. Fang, O. J. Kwon, and C.-Y. Wang, "Electrochemical-thermal modeling of automotive li-ion batteries and experimental validation using a three-electrode cell," *International Journal of Energy Research*, vol. 34, no. 2, pp. 107 – 15, 2010.

[103] P. Nelson, D. Dees, K. Amine, and G. Henriksen, "Modeling thermal management of lithium-ion pngv batteries," *Journal of Power Sources*, vol. 110, no. 2, pp. 349 – 356, 2002.

[104] C. Forgez, D. Vinh Do, G. Friedrich, M. Morcrette, and C. Delacourt, "Thermal modeling of a cylindrical LiFePO4/graphite lithium-ion battery," *Journal of Power Sources*, vol. 195, no. 9, pp. 2961 – 2968, 2010.

[105] T. Yoshida, M. Takahashi, S. Morikawa, C. Ihara, H. Katsukawa, T. Shiratsuchi, and J. Yamaki, "Degradation mechanism and life prediction of lithium-ion batteries," *Journal of the Electrochemical Society*, vol. 153, no. 3, p. A576, 2006.

[106] M. Broussely, P. Biensan, F. Bonhomme, P. Blanchard, S. Herreyre, K. Nechev, and R. Staniewicz, "Main aging mechanisms in Li ion batteries," *Journal of Power Sources*, vol. 146, no. 1-2, pp. 90 – 96, 2005.

[107] J. Newman, *Electrochemical Systems*, 2nd ed.   Prentice Hall, 1991.

[108] S. B. Peterson, J. Apt, and J. Whitacre, "Lithium-ion battery cell degradation resulting from realistic vehicle and vehicle-to-grid utilization," *Journal of Power Sources*, vol. 195, no. 8, pp. 2385 – 2392, 2010.

[109] J. Wang, P. Liu, J. Hicks-Garner, E. Sherman, S. Soukiazian, M. Verbrugge, H. Tataria, J. Musser, and P. Finamore, "Cycle-life model for graphite-LiFePO4 cells," *Journal of Power Sources*, vol. 196, no. 8, pp. 3942 – 3948, 2011.

[110] T. Cover, J. Thomas, and J. Wiley, *Elements of information theory.*   Wiley Online Library, 1991, vol. 1.

[111] A. Baughman and M. Ferdowsi, "Double-tiered switched-capacitor battery charge equalization technique," *IEEE Trans. on Industrial Electronics*, vol. 55, no. 6, pp. 2277–85, 2008.

[112] J. W. Kimball, B. T. Kuhn, and P. T. Krein, "Increased performance of battery packs by active equalization," *2007 IEEE Vehicle Power and Propulsion Conference*, Sept. 9-12 2007 2007.

[113] P. Balakrishnan, R. Ramesh, and T. Prem Kumar, "Safety mechanisms in lithium-ion batteries," *Journal of Power Sources*, vol. 155, no. 2, pp. 401–414, 2006.

[114] G.-H. Kim, A. Pesaran, and R. Spotnitz, "A three-dimensional thermal abuse model for lithium-ion cells," *Journal of Power Sources*, vol. 170, no. 2, pp. 476 – 89, 2007.

[115] E. Denardo, *Dynamic Programming: Models and Applications*. Courier Dover Publications, 2003.

[116] A. English, "2012 Toyota Plug-in Prius Review," *Popular Mechanics*, 2009. [Online]. Available: http://www.popularmechanics.com/automotive/new_cars/ 4339705.html

[117] R. Johri and Z. Filipi, "Low-Cost Pathway to Ultra Efficient City Car: Series Hydraulic Hybrid System with Optimized Supervisory Control," *SAE International Journal of Engines*, vol. 2, no. 2, pp. 505–520, 2010.

[118] V. Larsson, L. Johannesson, and B. Egardt, "Impact of Trip Length Uncertainty on Optimal Discharging Strategies for PHEVs," in *Proceedings of the 6th IFAC Symposium Advances in Automotive Control*, 2010.

[119] T. W. Anderson and L. A. Goodman, "Statistical inference about markov chains," *Annals of Mathematical Statistics*, vol. 28, no. 1, pp. 89–110, 1957.

[120] P. Brockwell and R. Davis, *Time Series: Theory and Methods*. Springer, 1998.

[121] USDOT-FHWA, "National Household Travel Survey," U.S. Department of Transportation, Federal Highway Administration, Tech. Rep., 2009, http://nhts.ornl.gov/index.shtml.

[122] M. Amiri, M. Esfahanian, M. R. Hairi-Yazdi, and V. Esfahanian, "Minimization of power losses in hybrid electric vehicles in view of the prolonging of battery life," *Journal of Power Sources*, vol. 190, no. 2, pp. 372 – 379, 2009.

[123] N. Shidore, J. Kwon, and A. Vyas, "Trade-off between PHEV fuel efficiency and estimated battery cycle life with cost analysis," *5th IEEE Vehicle Power and Propulsion Conference*, pp. 669 – 677, 2009.

[124] Z. Amjadi and S. S. Williamson, "Power-electronics-based solutions for plug-in hybrid electric vehicle energy storage and management systems," *IEEE Transactions on Industrial Electronics*, vol. 57, no. 2, pp. 608 – 616, 2010.

[125] C. Mi, B. Li, D. Buck, and N. Ota, "Advanced electro-thermal modeling of lithium-ion battery system for hybrid electric vehicle applications," *2007 IEEE Vehicle Power and Propulsion Conference*, pp. 107 – 111, 2007.

[126] D. Bertsekas, *Dynamic Programming and Optimal Control, Vols I and II.* Athena Scientific, 2005.

[127] AAA, "Daily fuel gauge report," AAA, Tech. Rep., 2010, http://www.fuelgaugereport.com/.

[128] M. A. Wiering and E. D. De Jong, "Computing optimal stationary policies for multi-objective Markov decision processes," *Proceedings of the 2007 IEEE Symposium on Approximate Dynamic Programming and Reinforcement Learning, ADPRL 2007*, pp. 158 – 165, 2007.

[129] M. Puterman and M. Shin, "Modified policy iteration algorithms for discounted Markov decision problems," *Management Science*, vol. 24, no. 11, pp. 1127–1137, 1978.

[130] M. Puterman, *Markov decision processes: Discrete stochastic dynamic programming.* John Wiley & Sons, Inc. New York, NY, USA, 1994.

[131] P. Kumar and P. Varaiya, *Stochastic systems: estimation, identification and adaptive control.* Prentice-Hall, Inc. Upper Saddle River, NJ, USA, 1986.

[132] D. De Farias and B. Van Roy, "The linear programming approach to approximate dynamic programming," *Operations Research*, vol. 51, no. 6, pp. 850 – 865, 2003.

[133] R. Luus, "Optimal control by dynamic programming using systematic reduction in grid size," *International Journal of Control*, vol. 51, no. 5, pp. 995 – 1013, 1990.

[134] ——, "Application of dynamic programming to high-dimensional non-linear optimal control problems," *International Journal of Control*, vol. 52, no. 1, pp. 239 – 250, 1990.

[135] ——, *Iterative dynamic programming.* CRC Press, 2000.

[136] G. Seenumani, J. Sun, and H. Peng, "A numerically efficient iterative procedure for hybrid power system optimization using sensitivity functions," New York, NY, United states, 2007, pp. 4738 – 4743.

[137] D. Bertsekas and J. Tsitsiklis, *Neuro-Dynamic Programming.* Athena-Scientific, 1996.

[138] J. M. Lee, N. S. Kaisare, and J. H. Lee, "Choice of approximator and design of penalty function for an approximate dynamic programming based control approach," *Journal of Process Control*, vol. 16, no. 2, pp. 135 – 156, 2006.

[139] W. Powell, *Approximate Dynamic Programming: Solving the curses of dimensionality.* Wiley-Interscience, 2007.

[140] P. B. Sharer, A. Rousseau, S. Pagerit, and P. Nelson, "Midsize and SUV Vehicle Simulation Results for Plug-In HEV Component Requirements," *SAE Papers, 2007 SAE World Congress*, vol. 2007-01-0295, 2007.

[141] P. B. Sharer, A. Rousseau, D. Karbowski, and S. Pagerit, "Plug-in hybrid electric vehicle control strategy: Comparison between ev and charge-depleting options," *SAE Papers, 2008 SAE World Congress*, vol. 2008-01-0460, 2008.

[142] A. Rousseau, S. Pagerit, and D. Gao, "Plug-in Hybrid Electric Vehicle Control Strategy Parameter Optimization," Electric Vehicle Symposium-23, Tech. Rep., 2007.

[143] T. Markel and A. Simpson, "Energy storage systems considerations for grid-charged hybrid electric vehicles," in *Vehicle Power and Propulsion, 2005 IEEE Conference*, Sept 2005, p. 6 pp.

[144] O. Sundstrom, D. Ambuhl, and L. Guzzella, "On implementation of dynamic programming for optimal control problems with final state constraints," *Oil and Gas Science and Technology*, vol. 65, no. 1, pp. 91 – 102, 2010.

[145] P. Papalambros and D. Wilde, *Principles of optimal design: modeling and computation.* Cambridge Univ Press, 2000.

[146] D. Karthikeyan, G. Sikha, and R. White, "Thermodynamic model development for lithium intercalation electrodes," *Journal of Power Sources*, vol. 185, no. 2, pp. 1398 – 407, 2008.

[147] J. Chatzakis, K. Kalaitzakis, N. Voulgaris, and S. Manias, "Designing a new generalized battery management system," *IEEE Transactions on Industrial Electronics*, vol. 50, no. 5, pp. 990–999, Oct. 2003.

[148] Y.-S. Lee and M.-W. Cheng, "Intelligent control battery equalization for series connected lithium-ion battery strings," *IEEE Transactions on Industrial Electronics*, vol. 52, no. 5, pp. 1297–1307, Oct. 2005.

[149] N. A. Chaturvedi, R. Klein, J. Christensen, J. Ahmed, and A. Kojic, "Algorithms for advanced battery-management systems," *IEEE Control Systems Magazine*, vol. 30, no. 3, pp. 49 – 68, 2010.

[150] S. Bashash, S. J. Moura, J. C. Forman, and H. K. Fathy, "Plug-in Hybrid Electric Vehicle Charge Pattern Optimization for Energy Cost and Battery Longevity," *Journal of Power Sources*, vol. 196, no. 1, pp. 541–549, 2011.

[151] A. Bemporad, F. Borrelli, and M. Morari, "Model predictive control based on linear programming - the explicit solution," *IEEE Transactions on Automatic Control*, vol. 47, no. 12, pp. 1974 – 1985, 2002.

[152] Y. Zhang and C.-Y. Wang, "Cycle-life characterization of automotive lithium-ion batteries with linio[sub 2] cathode," *Journal of The Electrochemical Society*, vol. 156, no. 7, pp. A527–A535, 2009.

[153] W. B. Gu and C. Y. Wang, "Thermal-Electrochemical Modeling of Battery Systems," *Journal of The Electrochemical Society*, vol. 147, no. 8, pp. 2910–2922, 2000.

[154] W. Fang, O. J. Kwon, and C.-Y. Wang, "Electrochemicalthermal modeling of automotive li-ion batteries and experimental validation using a three-electrode cell," *International Journal of Energy Research*, vol. 34, no. 2, pp. 107–115, 2010.

[155] S. Golmon, K. Maute, and M. L. Dunn, "Numerical modeling of electrochemical-mechanical interactions in lithium polymer batteries," *Computers and Structures*, vol. 87, no. 23-24, pp. 1567 – 1579, 2009.

[156] B. Wilson and J. Stein, "An algorithm for obtaining proper models of distributed and discrete systems," *Transactions of the ASME. Journal of Dynamic Systems, Measurement and Control*, vol. 117, no. 4, pp. 534 – 40, 1995.

[157] S. Santhanagopalan and R. E. White, "Online estimation of the state of charge of a lithium ion cell," *Journal of Power Sources*, vol. 161, no. 2, pp. 1346 – 1355, 2006.

[158] V. R. Subramanian, V. Boovaragavan, V. Ramadesigan, and M. Arabandi, "Mathematical model reformulation for lithium-ion battery simulations: Galvanostatic boundary conditions," *Journal of The Electrochemical Society*, vol. 156, no. 4, pp. A260–A271, 2009.

[159] V. Ramadesigan, V. Boovaragavan, J. J. Carl Pirkle, and V. R. Subramanian, "Efficient reformulation of solid-phase diffusion in physics-based lithium-ion battery models," *Journal of The Electrochemical Society*, vol. 157, no. 7, pp. A854–A860, 2010.

[160] A. P. Schmidt, M. Bitzer, A. W. Imre, and L. Guzzella, "Experiment-driven electrochemical modeling and systematic parameterization for a lithium-ion battery cell," *Journal of Power Sources*, vol. 195, no. 15, pp. 5071 – 5080, 2010.

[161] L. Cai and R. E. White, "Reduction of model order based on proper orthogonal decomposition for lithium-ion battery simulations," *Journal of the Electrochemical Society*, vol. 156, no. 3, pp. A154 – A161, 2009.

[162] C. Speltino, D. Di Domenico, G. Fiengo, and A. Stefanopoulou, "Comparison of reduced order lithium-ion battery models for control applications," 2009, pp. 3276 – 81.

[163] D. Di Domenico, A. Stefanopoulou, and G. Fiengo, "Lithium-ion battery state of charge and critical surface charge estimation using an electrochemical model-based extended kalman filter," *Journal of Dynamic Systems, Measurement and Control, Transactions of the ASME*, vol. 132, no. 6, 2010.

[164] D. Li and Y. Haimes, "Multiobjective dynamic programming. the state of the art," *Control, theory and advanced technology*, vol. 5, no. 4, pp. 471 – 483, 1989.

[165] A. Shwartz, "Death and discounting," *IEEE Transactions on Automatic Control*, vol. 46, no. 4, pp. 644 – 7, 2001.

[166] M. Jacobson, N. Shimkin, and A. Shwartz, "Markov decision processes with slow scale periodic decisions," *Mathematics of Operations Research*, vol. 28, no. 4, pp. 777 – 800, 2003.

[167] H. Fathy, "Combined Plant and Control Optimization: Theory, Strategies, and Applications," Ph.D. dissertation, Mechanical Engineering, University of Michigan, Ann Arbor, 2003.

[168] P. Patil, Z. Filipi, and H. Fathy, "Computationally Efficient Combined Design and Control Optimization Using a Coupling Measure," *2010 IFAC Symposium on Mechatronic Systems*, 2010.

[169] M.-J. Kim and H. Peng, "Power management and design optimization of fuel cell/battery hybrid vehicles," *Journal of Power Sources*, vol. 165, no. 2, pp. 819 – 32, 2007.

[170] B. Conlon, P. Savagian, A. Holmes, and M. Harpster, "Output Split Electrically-Variable Transmission with Electric Propulsion Using One or Two Motors," *U.S. Patent 2009/0092171 A1*.

[171] B. Adornato, R. Patil, Z. Filipi, Z. Baraket, and T. Gordon, "Characterizing naturalistic driving patterns for plugin hybrid electric vehicle analysis," Dearborn, MI, United states, 2009, pp. 655 – 660.

[172] Z. Ma, D. Callaway, and I. Hiskens, "Decentralized charging control for large populations of plug-in electric vehicles: Application of the nash certainty equivalence principle," in *Control Applications (CCA), 2010 IEEE International Conference on*, 2010, pp. 191 –195.

[173] D. Callaway and I. Hiskens, "Achieving Controllability of Electric Loads," *Proceedings of the IEEE*, vol. 99, no. 1, pp. 184–199, 2011.

[174] J. Kassakian, M. Schlecht, and G. Verghese, *Principles of power electronics*, ser. Addison-Wesley series in electrical engineering.   Addison-Wesley, 1991.

[175] P. Krein, *Elements of Power Electronics*, ser. The Oxford series in electrical and computer engineering. Oxford University Press, 1998.

[176] M. Krstic and A. Smyshlyaev, "Adaptive control of PDEs," *Annual Reviews in Control*, vol. 32, no. 2, pp. 149–60, 12 2008.

[177] M. Krstic, *Boundary Control of PDEs: A Course on Backstepping Designs*. Philadelphia, PA: Society for Industrial and Applied Mathematics, 2008.

[178] H. Fathy, Z. Filipi, J. Hagena, and J. Stein, "Review of hardware-in-the-loop simulation and its prospects in the automotive area," vol. 6228, no. 1, 2006, pp. 1–20.

[179] B. Bloom and D. Krathwohl, "Taxonomy of educational objectives: The classification of educational goals. Handbook I: Cognitive domain," 1956.

[180] J. C. Forman, S. Bashash, J. L. Stein, and H. K. Fathy, "Reduction of an electrochemistry-based li-ion battery degradation model via constraint linearization and pade approximation," *Journal of the Electrochemical Society (Accepted)*, 2010.

[181] C. Speltino, D. Di Domenico, G. Fiengo, and A. G. Stefanopoulou, "Cell Equalization In Battery Stacks Through State Of Charge Estimation Polling," in *Proceedings of the 2010 American Control Conference*, 2010.

[182] J. A. Gubner, *Probability and random processes for electrical and computer engineers*. New York, NY: Cambridge University Press, 2006.